TURBULENT OCEAN-TO-ICE HEAT TRANSFER: LABORATORY AND NUMERICAL STUDIES

by

Eshwan Ramudu

A dissertation submitted to The Johns Hopkins University
in conformity with the requirements for the degree of
Doctor of Philosophy

Baltimore, Maryland
May, 2018

Abstract

This thesis explores turbulent ocean-to-ice heat transfer and consists of two main studies. The first is a laboratory experiment on the time evolution of an ice layer cooled from below and subjected to a turbulent shear flow of warm water from above. This experiment is motivated by observations of warm water intrusion into the ocean cavity under Antarctic ice shelves, accelerating the melting of their basal surfaces. Either partial transient melting or complete melting of the ice occurs in our experiments depending on the strength of the applied turbulent shear flow, which is represented in terms of its Reynolds number Re. The ice consequently reforms at a rate independent of Re. A one-dimensional model for the evolution of the ice thickness is derived from the experimental results. Applying our model to field measurements at a site under the Antarctic Pine Island Glacier ice shelf yields a predicted melt rate that exceeds present-day observations. Arctic sea ice is also rapidly declining. In the second study, we use large eddy simulation (LES) to investigate numerically the turbulent entrainment of heat from the mixed layer, a mechanism that is possibly partly responsible for the observed sea ice loss. We model the Arctic Ocean's Canada Basin, which features a perennial anomalously warm Pacific Summer Water (PSW) layer at the base of the mixed layer and a summertime Near-Surface Temperature Max-

imum (NSTM) within the mixed layer, trapping heat from solar radiation. The ice drift velocity and initial temperature profiles are varied in our simulations. The results show that the presence of the NSTM enhances heat entrainment from the mixed layer. Additionally there is no PSW heat entrained under the parameter space considered. We propose a scaling law for the ocean-to-ice heat flux, which depends on the initial NSTM temperature anomaly and the ice-drift velocity. In an extension of this LES study, we investigate, the effect of varying the ice basal surface roughness z_0 over three orders of magnitude, all other parameters being kept constant. As z_0 is increased, the heat flux to the ice basal surface increases to a peak value, then decreases.

Faculty Advisor and Primary Reader: Dr. Anand Gnanadesikan

Secondary Readers: Drs. Charles Meneveau and Peter Olson

Acknowledgments

I am grateful to my Ph.D. advisor, Dr. Anand Gnanadesikan, for his guidance and patience from beginning to end of my thesis work. I sincerely thank Drs. Peter Olson, Charles Meneveau, Renske Gelderloos, and Di Yang for their mentorship. I feel very fortunate to have had the chance to work with such an accomplished and dedicated group of scientists, and from them, I learned to become a better thinker.

I enjoyed the courses taught by Drs. Thomas Haine, Peter Olson, Anand Gnanadesikan, Darryn Waugh, Andrea Prosperetti, Charles Meneveau, Rajat Mittal, and Joseph Katz, and I thank them for their excellent teaching. I acknowledge the helpful and generous feedback from Dr. Haine over the course of my thesis work.

Special thanks to Ben Hirsh, without whose technical assistance the laboratory experiment I conducted would not have been possible. Thank you also to Rich Middlestat, Frank Cook, and Daren Ayres from the Whiting School of Engineering Machine Shop for building my laboratory apparatus.

To Flori Yellin, Tony Martinez, Xiang Yang, Jordan Thomas, and Carl Shapiro, thank you so much for your company and inspiration during my time at Johns Hopkins. To my friends outside Johns Hopkins, Alex Bick, Vij Dhayan,

Matthew Fierstein, and Jian Li, thank you too for your encouragement.

Many thanks to Sonali Abraham, Joel Bretheim, Courtney Engle, Alex Fuller, Ismail Hameduddin, Stephen Jeffress, Perry Johnson, Grace Kim, Sarita Koride, Maylis Landeau, Aleksi Nummelin, Marie-Aude Pradal, Jane Schwab, Elina Spyrou, Kial Stewart, and Hannah Susorney for meaningful discussions and friendship.

I am especially thankful to my family and my in-laws, the Pasrichas, for being ever supportive.

Finally thank you to my wonderful wife, Trisha, who has been beside me on this journey to pursue a Ph.D.

Funding for this work came from the National Science Foundation (grant EAR-110371, PI: Dr. Peter Olson) and from the National Oceanic and Atmospheric Administration (grant NA15OAR4310172, co-PIs: Drs. Anand Gnadesikan and Thomas Haine) and is gratefully acknowledged.

Contents

List of Tables

List of Figures

Chapter 1

Introduction

1.1 Motivation

Of the total amount of fresh water on Earth, more than 87% is in the form of ice and more than 90% of that ice exists in Antarctica (Jacobs *et al.*, 1992). Antarctica is covered by about 12 million km^2 of grounded ice and surrounded by about 1.5 million km^2 of ice shelves (Drewry *et al.*, 1982). If Antarctica loses all its ice, the global sea level could rise by 60–72 m (Drewry & Morris, 1992). The stability of Antarctica's land ice relies on ice shelves, which are floating extensions of the grounded ice sheets limiting ice discharge into the ocean.

Alarmingly, Antarctica's ice shelves are melting at an accelerating pace. Between 2003 and 2012, ice shelves lost roughly 310 km^3 of ice per year. In comparison, the volume loss between 1994 and 2003 was a negligible 25 km^3 per year approximately (Paolo *et al.*, 2015). The measured changes in Antarctic ice shelves are shown in figure 1. Ice shelves lose mass through iceberg calving, basal melting, topside sublimation, wind drift, and decreased glacier flux (Pritchard *et al.*, 2012; Rignot *et al.*, 2013). While iceberg calving has traditionally been considered the main form of mass loss, basal melting now accounts for roughly

the same amount of mass loss as calving for Antarctica as a whole (Depoorter *et al.*, 2013). This increase in basal melting is party due to an influx of relatively warm and salty Circumpolar Deep Water into the ocean cavity under ice shelves (Jacobs *et al.*, 2011), the CDW influx being itself caused by an increase in the westerly wind stress around the continental shelf (Steig *et al.*, 2012).

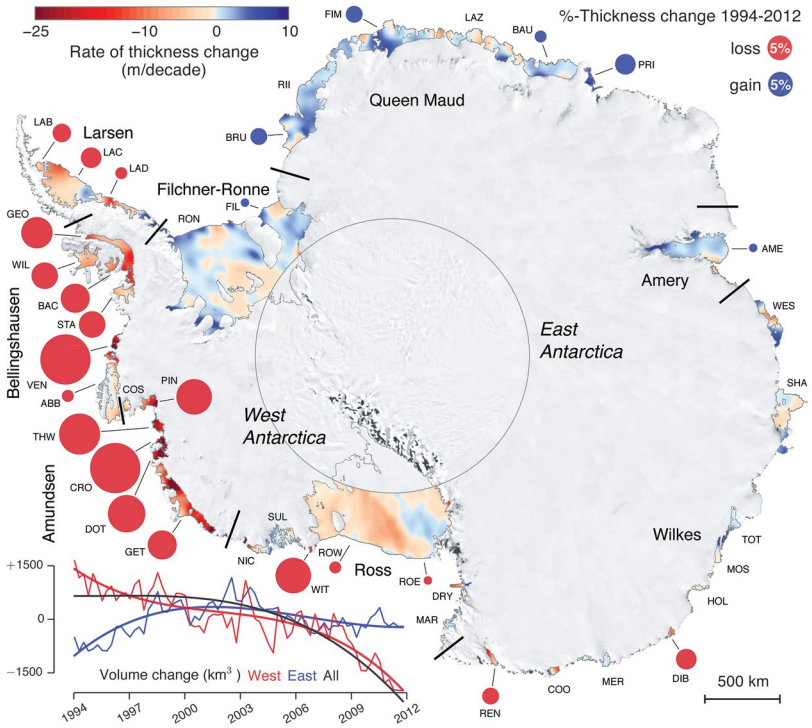

Figure 1.1: Rate of thickness change of Antarctic ice shelves from 1994 to 2012 estimated from measurements. (Bottom left) Average volume change over the same time period for western (red), eastern (blue), and all (black) ice shelves. (Reproduced from Paolo *et al.* (2015)).

Arctic sea ice is one of the most expansive geophysical features on Earth. Its extent varied from a minimum of about 7.5 million km^2 in late summer to a maximum of about 15.5 million km^2 in winter between 1979 and 2000 (Comiso, 2003). Arctic sea ice plays an integral role in governing Earth's climate. It is

responsible for the ice-albedo feedback mechanism in the Arctic, regulating the impact of solar radiation forcing on the atmosphere-ice-ocean system (Perovich *et al.*, 2007). It also insulates the Arctic lower atmosphere from ocean heat. Additionally, the formation of sea ice in the Arctic drives a local deep convection pattern which cools and ventilates deep and bottom waters part of the global thermohaline cirulation (Dieckmann & Hellmer, 2003).

The Arctic sea ice cover is rapidly shrinking. Between 1979 and 2006, sea ice extent in September has declined by a rate of about 9% per decade (Stroeve *et al.*, 2007). Figure 1.2 shows the comparison between Arctic sea extent on September 13, 2017 and the median 1981–2010 extent for that same day. Based on submarine observations and satellite measurements, the mean sea ice thickness is estimated to have have decreased from 1.62 m in the period 1993–1997 to 1.43 m in the period 2003-2007, representing a -12% change (Kwok & Rothrock, 2009). A number of climate models predict that the Arctic may have its first ice-free summer by 2050 (AMAP, 2012). Arctic ice loss will have important ramifications for the climate, ecological dynamics, and humans. The positive ice-albedo feedback mechanism will lead to the polar amplification of climate change (Holland & Bitz, 2003). The expansion open water areas in the Arctic will allow increased solar heat input into the ocean, which can contribute to further thinning of sea ice (Perovich *et al.*, 2007). Furthermore, in regions where sea ice has melted, positive temperature anomalies are present in the lower atmosphere locally due to turbulent heat fluxes from the ocean. These temperature anomalies are spread by atmospheric circulation and consequently affect neighboring regions (Serreze *et al.*, 2009, 2011). This process, in addition to other associated changes, can have complex remote effects (Vihma, 2014).

Francis *et al.* (2009) demonstrated that, in response to the loss of sea ice, the polar jet stream has weakened and Liu *et al.* (2012) indicated that the frequency of snow storms in the mid-latitudes is increasing. Yang & Christensen (2012) found, using CMIP5 models, that sea ice reduction will contribute to a warming trend in Europe in the period 2006-2100. Sea ice loss will also impact terrestrial vegetaion and Arctic faunal diversity, which consists of species such as polar bears, walruses, seals, caribous, and dolphins (Post *et al.*, 2013). In addition, the Arctic's 400,000 indigeneous people and coastal communities, including many in Alaska, may be forced to relocate (Bronen, 2013).

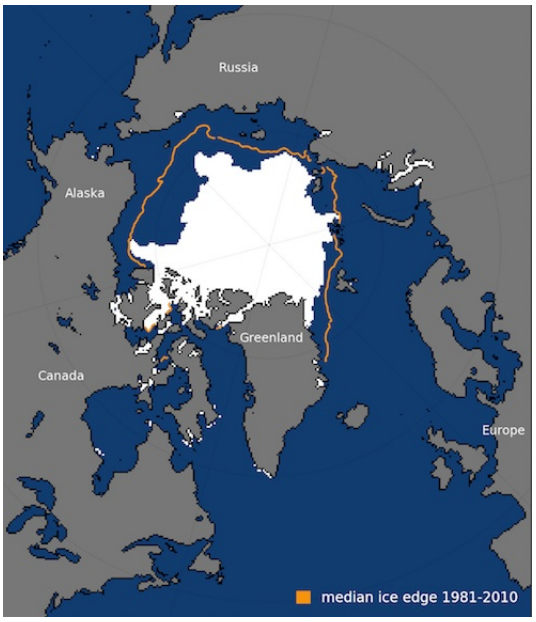

Figure 1.2: Arctic sea ice extent on September 13, 2017 (white area) compared with 1981-2010 average ice extent for that day (orange line). Credit: National Snow and Ice Data Center.

The observed retreat of Arctic sea ice is due to a combination of strong natural variability in the couple ice-ocean-atmosphere system and increasing radiative forcing caused by anthropogenic warming (Serreze *et al.*, 2007). Con-

cerning the mechanisms directly responsible for melting, Steele *et al.* (2010) showed that for the summers of 2002–2006 in the Pacific Sector of the Arctic, 31% of ice loss was due to top surface melting, forced by atmosphere-ice heat fluxes, 27% was due to bottom melting caused by solar radiative input into the ocean, and 42% was due to bottom melting caused by dynamical ocean processes such as advection and convective heat transfer. Zhang *et al.* (2013) reported that the Arctic sea ice extent record low reached in 2012 was driven by a strong increase in bottom melt during the passage of a cyclone. Turbulent heat fluxes from the ocean were the dominant process causing bottom melting.

The important contribution of turbulent ocean-to-ice heat transfer in the melting of the basal surface of Antarctic ice shelves and Arctic sea ice is the motivation for this thesis. Turbulent heat transfer in a fluid is the transfer of thermal energy by the turbulent motions, or eddies, in the fluid. In this work, I use two methods to study this subject in the context of ocean–ice interaction.

1.2 Methods

The first method is a laboratory experiment designed to investigate the melting of ice in response to heat transfer from a turbulent flow of warm water. The application of this experiment is the basal melting of Antarctic ice shelves by warm water flow along their basal surfaces. By being designed to have dynamic and thermodynamic similarity, scaled laboratory experiments contribute meaningfully to the understanding of processes in real-life geophysical systems. Laboratory experiments have been used extensively in the investigation of ice–ocean interaction (Huppert & Worster, 1985; Wettlaufer *et al.*, 1997; Neufeld &

Wettlaufer, 2008; Stern *et al.*, 2014; Kerr & McConnochie, 2015; McConnochie & Kerr, 2017). This study adds to this body of work by considering ice ablation due to heat transfer uniquely.

The second method is high-resolution numerical modeling using large eddy simulation (LES). Through this approach, turbulent heat transfer from the ocean mixed layer to sea ice in the Arctic is investigated. LES has been applied in numerous planetary boundary layer (PBL) studies involving buoyancy, rotation, rough surfaces, ocean waves, canopies, entrainment, radiation, and/or condensation (Moeng & Sullivan, 2015). Heat transfer in the PBL under sea ice is a unique problem because both temperature and salinity differences conspire to set the rate of heat transfer. LES is a useful tool for this investigation because it can resolve a significant fraction of the turbulent fluxes. Two previous studies (Skyllingstad & Denbo, 2001; Skyllingstad *et al.*, 2003) on ocean-to-ice turbulent exchanges have been based on LES. In this study, the Johns Hopkins University *LESGO* code is used. In order for the code to be tailored for its application, the scalar transport equation was added. Details of the numerical implementation of this equation are provided in §A.1. A brief description of the LES technique is given next (§1.3).

1.3 Large eddy simulation

Turbulent flows consist of motions that span a wide range of scales. The larger scales contain most of the energy while the smaller scales dissipate the energy. For high Reynolds number flows, resolving all the scales of motion in numerical simulations is prohibitively expensive with the computational power available

today. LES helps address this challenge. In LES, the large scales of the flow are explicitly resolved while the effect of the finer scales is modeled. Thus the computational cost of resolving the small scales is not incurred. (Pope, 2000)

The LES method is based on a spatial filtering operation,

$$\widetilde{f}(x_i) = \int_D f(x_i')G(x_i, x_i'; \Delta)\mathrm{d}x_i', \tag{1.1}$$

f representing the variable being filtered; $\widetilde{f}$, the filtered variable; i, an index that takes the values 1, 2, and 3 to denote the x, y, z directions respectively; D, the domain; G, the filter function; and Δ, the filter width. This operation separates the larger scales from the smaller scales. Applied to the velocity field u_i, filtering results in the decomposition of u_i into a filtered (resolved) part, $\widetilde{u}_i$, and a residual (sub-grid scale) part u_i'. The governing equations of motion for an incompressible fluid without the action of any body forces are

$$\frac{\partial u_i}{\partial x_i} = 0 \tag{1.2}$$

$$\frac{\partial u_i}{\partial t} + \frac{\partial}{\partial x_j}(u_i u_j) = -\frac{1}{\rho}\frac{\partial p}{\partial x_i} + \nu\frac{\partial^2 u_i}{\partial x_j \partial x_j}, \tag{1.3}$$

where p is the pressure, ρ is the density, and ν is the kinematic viscosity. For the spatially-filtered velocity, the governing equations become

$$\frac{\partial \widetilde{u}_i}{\partial x_i} = 0 \tag{1.4}$$

$$\frac{\partial \widetilde{u}_i}{\partial t} + \frac{\partial}{\partial x_j}(\widetilde{u}_i \widetilde{u}_j) = -\frac{1}{\rho}\frac{\partial \widetilde{p}}{x_i} + \nu\frac{\partial^2 \widetilde{u}_i}{\partial x_j \partial x_j} - \frac{\partial \tau_{ij}}{\partial x_j}. \tag{1.5}$$

$\tau_{ij} = \widetilde{u_i u_j} - \widetilde{u}_i \widetilde{u}_j$ is the residual (sub-grid scale) stress tensor. To close the above equations, a model for τ_{ij} is required. Since in LES, the dissipative small scales of motion are unresolved, the sub-grid scale (SGS) model needs to be formulated

so that it removes energy from the resolved scales. τ_{ij} is thus usually expressed in terms of the eddy viscosity ν_T,

$$\tau_{ij} - \frac{\delta_{ij}}{3} = -2\nu_T \widetilde{S}_{ij}, \tag{1.6}$$

with $\widetilde{S}_{ij}$ being the resolved strain-rate tensor (Piomelli, 1999). The Smagorinsky model,

$$\nu_T = C\Delta^2 |\widetilde{S}| \widetilde{S}_{ij} \tag{1.7}$$

where C is a coefficient, was proposed as an algebraic approach to representing ν_T (Smagorinsky, 1963; Lilly, 1967). Although simple and numerically robust, the use of a constant value for C has important limitations. The model is over-dissipative close to the wall or when the grid scale approaches the limits of the inertial range and is additionally unable to properly account for the effects of stratification, shear, and rotation. To eliminate the procedure of calibrating the coefficient C in the Smagorinsky model, Germano *et al.* (1991) introduced the dynamic model in which C is evaluated based on information from the resolved scales of the flow. The dynamic model has offered opportunities for further approaches giving greater accuracy. (Meneveau & Katz, 2000)

To illustrate the concept of LES, figure 1.3 shows a model energy spectrum of a turbulent flow. The cut-off filter operation causes eddies with wavenumber lower than the filter-width to be resolved. These resolved eddies are typically of the integral or inertial scales. Eddies with wavenumber higher than the filter width, whose scale is usually of the order of the Kolmogorov scale, are modeled. In figure 1.4, the result of using LES to represent a flow field can be compared against the direct numerical simulation (DNS) of the same flow field. It can be seen that the small scale features are absent in the LES solution (figure 1.4a).

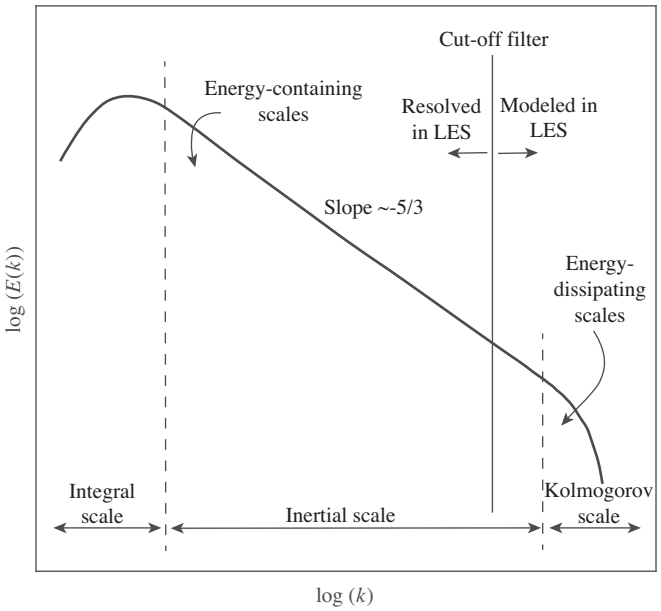

Figure 1.3: Model energy spectrum E in a turbulent flow plotted against wavenumber k

In this study, the scale-dependent Lagrangian dynamic SGS model is used for estimating the Smagorinsky coefficient C in modeling the eddy viscosity. An extension of the Germano *et al.* (1991) dynamic model, this approach involves the accumulation of averages in time by following fluid pathlines in the resolved velocity field. It yields a scale dependent coefficient C through an additional filtering operation. The mean dissipation properties from the use of this model are of high accuracy. Full details can be found in Bou-Zeid *et al.* (2005).

1.4 Thesis outline

Chapter 2 presents the laboratory experiment on the time evolution of an ice layer cooled from below and subjected to a turbulent shear flow of warm water

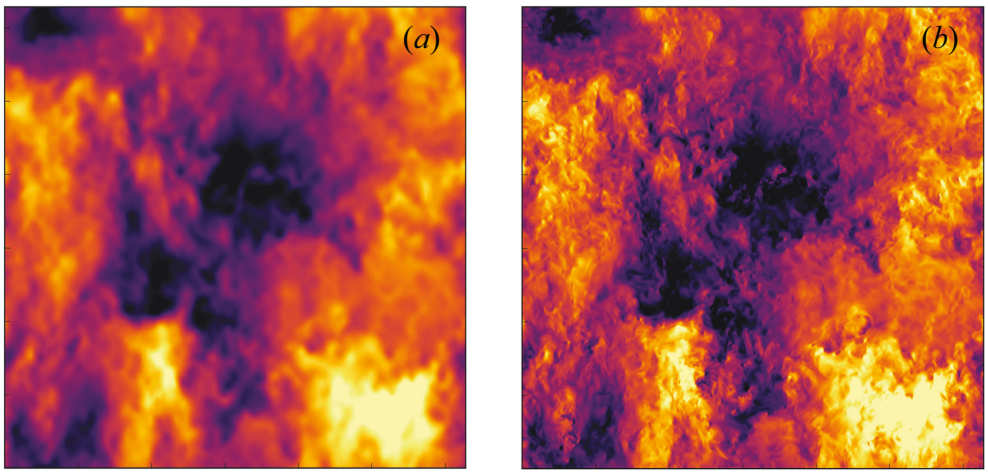

Figure 1.4: Instantaneous velocity field in homogeneous isotropic turbulence solved using (a) LES and (b) DNS (reproduced from Martínez Tossas (2017)).

from above. This study is motivated by observations of warm water intrusion into the ocean cavity under Antarctic ice shelves, accelerating the melting of their basal surfaces. The strength of the applied turbulent shear flow in the experiments is represented in terms of its Reynolds number Re, which is varied over the range $2.0 \times 10^3 \leq Re \leq 1.0 \times 10^4$. Depending on the water temperature, partial transient melting of the ice occurs at the lower end of this range of Re and complete transient melting of the ice occurs at the higher end. Following these episodes of transient melting, the ice reforms at a rate that is independent of Re. The experimental measurements of ice thickness and temperature are fitted to a one-dimensional model for the evolution of the ice thickness in which the turbulent heat transfer is parameterized in terms of the friction velocity of the shear flow. Applying the model to field measurements at a site under the Antarctic Pine Island Glacier ice shelf yields a predicted melt rate that exceeds present-day observations.

Chapter 3 presents the LES-based study on turbulent ocean-to-ice heat

transfer in the Arctic. The faster than projected retreat of Arctic sea ice suggests that free-running large-scale climate models may not be accurately representing some key processes. The small-scale turbulent entrainment of heat from the mixed layer could be one such process. To better understand this mechanism, we model the Arctic Ocean's Canada Basin, which is characterized by a perennial anomalously warm Pacific Summer Water (PSW) layer residing at the base of the mixed layer and a summertime Near-Surface Temperature Maximum (NSTM) within the mixed layer trapping heat from solar radiation. Using LES, we investigate heat entrainment for different ice drift velocities and different initial temperature profiles. The value of LES is that the resolved turbulent fluxes are greater than the sub-grid scale fluxes for most of our parameter space. The results show that the presence of the NSTM enhances heat entrainment from the mixed layer. Additionally there is no PSW heat entrained under the parameter space considered. We propose a scaling law for the ocean-to-ice heat flux which depends on the initial temperature anomaly in the NSTM layer and the ice-drift velocity. A case study of 'The Great Arctic Cyclone of 2012' gives a turbulent heat flux from the mixed layer that is approximately 70% of the total ocean-to-ice heat flux estimated from the PIOMAS model often used for short-term predictions. Present results highlight the need for large-scale climate models to account for the NSTM layer.

Chapter 4 is an extension of the LES study of Chapter 3. The effect of varying the basal surface roughness on the turbulent ocean-to-ice heat flux is investigated using the same LES set-up. A summary of the derivation of the heat transfer law used as a boundary condition to estimate the heat flux at the ice–ocean interface is first presented. The roughness length z_0 is varied

over three orders of magnitude (1.2×10^{-5} m $\leq z_0 \leq 1.2 \times 10^{-2}$ m). As z_0 increases, the turbulent heat flux to the basal surface peaks to a value that is roughly twice the heat flux at the lowest z_0, then decreases. This result suggests that there is an optimal roughness length that allows for a maximum melting rate. A physical interpretation of the heat flux–roughness behavior is that, while roughness causes additional fluctuations in the flow, which enhance heat transfer, it also decelerates the flow at the wall, which suppresses heat transfer. Common parameterizations for estimating the ocean-to-ice heat flux in climate models are reviewed. The treatment of surface roughness in these parameterizations is suggested as an important future research areas.

Finally, two studies based on the work presented in this thesis are proposed in chapter 5. The first is a laboratory experiment investigating ice ablation due to heat and salt exchange with a turbulent flow. The second is a LES-based study on heat entrainment from the ocean to sea ice in a marginal ice zone, in which the parameters varied include the size of the ice floes and the fraction of open-water areas.

Chapter 2

Turbulent heat exchange between water and ice at an evolving ice–water interface

The work presented in this chapter is reproduced from Ramudu *et al.* (2016).

2.1 Introduction

The exchange of heat and salt across the turbulent boundary layer at the ice-ocean interface governs the rate at which sea ice and ice shelves melt or grow in response to changes in ocean properties. Estimates of the heat exchange at such interfaces vary substantially across observational and modelling studies. In order to predict the evolution of sea ice and ice shelves more accurately, better constraints on their heat exchanges with the underlying ocean are needed.

Antarctica is surrounded by ice shelves, thick floating sheets of ice that extend from the grounding line onto the ocean surface. They play a critical role in the mass balance and dynamics of Antarctica's terrestrial ice by serving as a buttress at the coastline and limiting the rate of ice flow into the ocean (Hooke, 2005). Antarctic ice shelves are also important to the formation of Antarctic

Bottom Water, a mass of dense water that fills about one half of the deep ocean (Broecker *et al.*, 1998) and that plays an important role in the carbon cycle (Marinov *et al.*, 2008).

Recent studies show that warm and salty Circumpolar Deep Water around Antarctica is shoaling onto the continental shelf and intruding into the ocean cavities under ice shelves, causing increased melting of their basal surfaces (Jacobs *et al.*, 2011; Pritchard *et al.*, 2012; Schmidtko *et al.*, 2014). This process is depicted in figure 2.1. Increased basal melting can trigger the disintegration of ice shelves (Feldmann & Levermann, 2015) and hence accelerate Antarctic ice loss, which would contribute significantly to global sea level rise. The rough topography of the ocean floor under ice shelves may play a role in guiding the warm shoaling water inside the cavity (Brisbourne *et al.*, 2014). Basal melting results in a buoyant plume of meltwater that flows along the shelf base, generating turbulence, which in turn affects both the transfer of heat to the shelf and the entrainment of heat from the relatively warm far-field into the relatively cold boundary layer (Little *et al.*, 2008).

Previous studies of ice shelf–ocean interaction have been conducted mainly through numerical models. The heat transfer from the ocean mixed layer to the ice shelf base in these models is parameterized in terms of the temperature difference across, and the thermal exchange velocity γ_T through, the boundary layer. γ_T is defined as the ratio of the thermal diffusivity to the thickness of the boundary layer. In the earlier works of Hellmer & Olbers (1989) and Scheduikat & Olbers (1990), γ_T was taken to be a constant. Jenkins (1991) followed the theory of Kader & Yaglom (1972), assuming that the ice–water interface is hydraulically smooth, and expressed γ_T in terms of the friction velocity of the

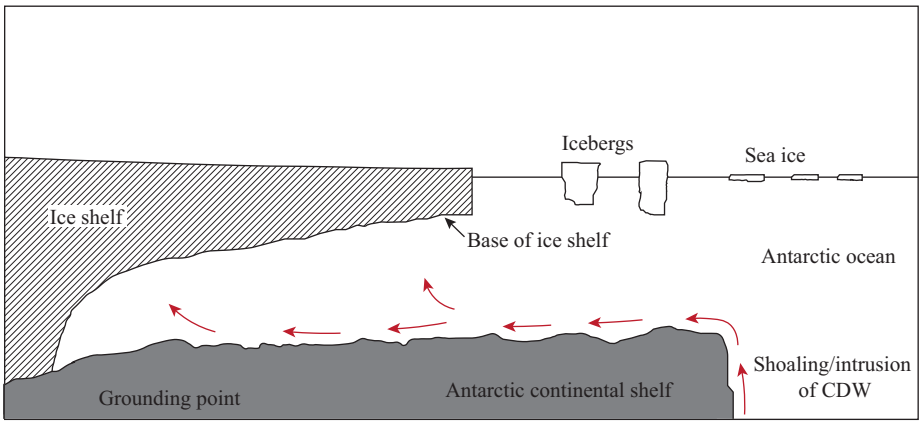

Figure 2.1: Warm Circumpolar Deep Water (CDW) rising into the ocean cavity under an Antarctic ice shelf.

turbulent boundary layer. This formulation was used in the studies by Holland & Feltham (2006) and Jenkins *et al.* (2010*b*). McPhee *et al.* (1987*a*) developed a parameterization for γ_T by using the formulation of Yaglom & Kader (1974) for the transfer of heat in a turbulent boundary layer near a rough wall and by additionally considering the effect of buoyancy and rotation on heat transfer. Holland & Jenkins (1999), Mueller *et al.* (2012), and Dansereau *et al.* (2014) adopted this parameterization in their studies. The formation of channels in the ice shelf base as a result of plumes flowing on the underside of the shelf has also been investigated numerically (Dallaston *et al.*, 2015).

There are numerous laboratory experiments on heat transfer at a phase change boundary between a solid and a liquid that are relevant to our study. Townsend (1964) investigated the evolution of the layer of free convection over an ice surface into a stable liquid layer above. The instability of an ice surface, and subsequent formation of a wavy interface, in the presence of a turbulent flow was explored by Gilpin *et al.* (1980). Significant work has been performed

on the study of the formation of a mushy layer and on compositional and thermal convection in the liquid during the solidification of a binary solution to explain brine rejection as sea ice forms (Huppert & Worster, 1985; Wettlaufer *et al.*, 1997). The effect of an external shear flow on a mushy layer has also been investigated (Neufeld & Wettlaufer, 2008). In the latter study, a laminar shear flow was applied to an NH_4Cl mushy layer from above and the primary focus was the stability of the mushy layer in response to the shear flow. Kerr & McConnochie (2015) developed a theoretical model for the dissolution of a vertical solid surface and tested their model with experimental measurements. These laboratory studies provide an explanation of the physical processes at an ice–water interface and are useful guides for investigating the effect of turbulent warm water at an ice-ocean interface. Also related to ice-shelf-ocean interaction is the set of experiments by Stern *et al.* (2014) on the effect of geometry on circulation inside the ice shelf cavity and at the ice shelf front. None of these studies, however, consider the effect of shear-driven turbulence on what is essentially a horizontal ice shelf–ocean interface.

In this paper, we describe an experimental study on the response of an ice–water interface to forced convection in the form of turbulent mixing in pure water over ice. The experiments are conducted in a cylindrical tank with a layer of ice growing on a basal cooling plate at the bottom, representing the base of an ice-shelf. The overlying water layer is covered at the top by a lid with a rough underside. This rough surface drives the motion in the water column and creates a well-mixed turbulent liquid layer when the lid is rotated. Turbulent mixing causes warm water to be transported from the far-field to the ice–water interface. Our laboratory set-up is an idealized, inverted model of the

ocean cavity under Antarctic ice shelves in which the circulation of relatively warm water is reaching the basal surface of these ice shelves, causing accelerated basal melting. The set-up is inverted because the boundary layer at the ice–water interface in the experiments is denser than the far-field whereas in the ocean, the boundary layer is relatively buoyant. There is no natural convection in our experiments and hence the boundary layer is stable in the absence of turbulent mixing.

An important difference between the laboratory set-up and the oceanographic case is the absence of salt in the experiments. The ice-ocean interface is at a temperature intermediate between the salinity-dependent freezing point of the ocean and the melting point of ice in fresh water (0 °C). The rate of phase change at the ice-ocean interface is governed by both the conservation of heat and the conservation of salt at the interface. When there is a large heat flux through the boundary layer to the ice–ocean interface, melting occurs. When the liquid far-field temperature is below the melting point of ice at the interface and the interface salinity is non-zero, conservation of salt at the interface causes ice to dissolve (Wells & Worster, 2011; Kerr & McConnochie, 2015). In this experimental study, we ignore the effect of salinity on the interface temperature, and we focus uniquely on the phase change due to heat transfer, melting.

We formulate a theoretical model for the evolution of the ice thickness in our experiments and compare our measurements with the prediction from our theoretical model in order to develop a parameterization for the turbulent heat transfer at the ice–water interface. The apparatus and procedure are described in §2.2. In §2.3, the governing equations in our theoretical model are outlined. The results from the set of experiments are shown in §2.4 and are compared to

Non-dimensional number	Definition	Experiment	Ice shelf cavity
Reynolds, Re	UD/ν	10^3 – 10^4	10^6
Friction Reynolds, Re_*	u_*D/ν	10^2 – 10^3	10^5
Rossby, Ro	$U/\Omega D$	0.7	1
Stefan, St	$c_s\Delta T_s/L$	0.2	0.2
Prandtl, Pr	ν/α_ℓ	13.6	13.8
Péclet, Pe	UD/α_ℓ	10^4 – 10^5	10^7
Volumetric heat capacity ratio, $\mathcal{C}$	$\rho_\ell c_\ell/\rho_s c_s$	2.2	2.2
Thermal diffusivity ratio, A	α_ℓ/α_s	0.12	0.12

Table 2.1: Dimensionless control parameters in the experiment and in an ice shelf cavity

the theoretical model in §2.5. In §2.6, we discuss the geophysical application of our results. Finally, we summarize our study in §2.7.

The dimensionless control parameters that are relevant to the study are the Reynolds number, friction Reynolds number, Rossby number, and Stefan number. The definition of these parameters and their estimated values in our experiments and in an ice shelf cavity are listed in table 2.1. In the definitions, the subscript s refers to the solid (ice) and the subscript ℓ refers to the liquid (water). D denotes the depth of the liquid layer; U, the characteristic velocity scale; u_*, the friction velocity; ν, the kinematic viscosity; Ω, the angular frequency of rotation; ρ, the density; c, the specific heat capacity; ΔT, the temperature difference; L, the specific latent heat; and α, the thermal diffusivity.

2.2 Experimental method

The experimental apparatus is shown in figure 2.2. It consists of a cylindrical tank of radius 17.5 cm with 1.5-cm-thick Perspex walls and a 5-cm-thick aluminum basal cooling plate. The tank is filled with pure water to a height of 10

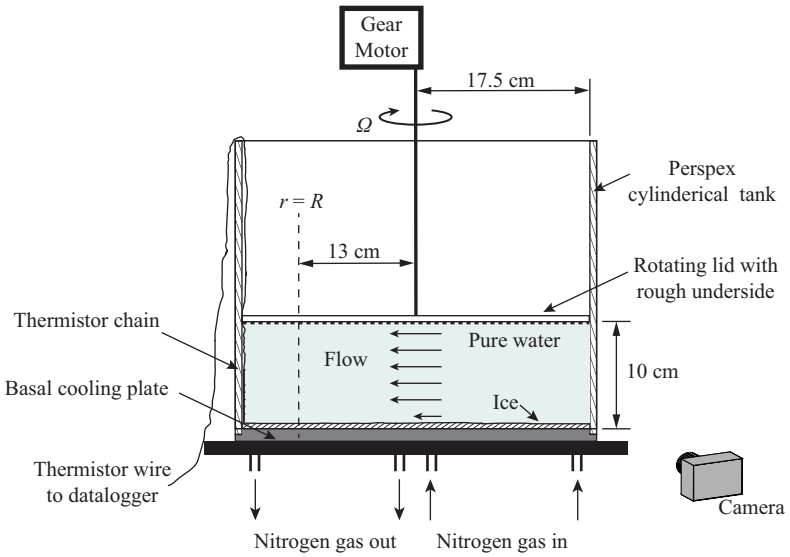

Figure 2.2: Schematic diagram of the apparatus

cm, and ice is grown by circulating cold nitrogen gas inside the basal cooling plate. The physical properties of liquid water and ice are listed in table 2.2. The interior of the plate consists of two sets of parallel spiral grooves, one set having an inlet at the center and an outlet near the rim and the other set having an inlet near the rim and an outlet at the center. This arrangement helps achieve a uniform heat flux through the plate and hence uniform ice growth on its surface. The nitrogen flow rate is held constant at 0.14 $m^3 min^{-1}$ within and across experiments. A perspex cover lid is positioned at the upper surface of the water layer, connected to a gear motor by means of a vertical metal rod. A plastic grid is attached to the underside of the cover lid, creating a rough surface for generating the turbulent shear flow. The grid consists of a lattice of squares, each square having sides of length 1.4 cm and projecting downward beneath the lid a distance of 0.9 cm. The rotation of the cover lid and plastic grid is controlled by the gear motor.

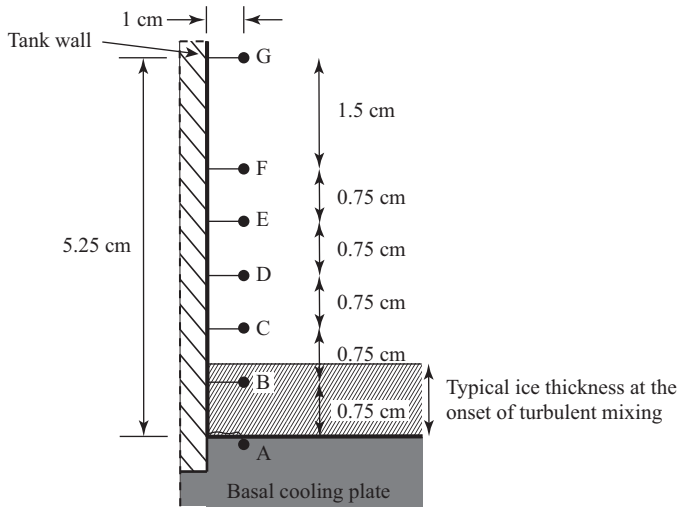

Figure 2.3: Arrangement of thermistors

To start each experiment, the water layer, initially at rest and at room temperature, is suddenly cooled from below by turning on the flow of nitrogen into the basal cooling plate. It typically takes about 30 minutes for ice to begin to nucleate on the basal plate. The ice is allowed to grow for another 30 minutes, reaching a nearly uniform thickness of 8–12 mm, depending on the initial temperature of the water. The motor is then turned on, rotating the lid and grid at a constant angular velocity, typically for about one hour. We experimented with lid angular velocities between 0.27 and 1.43 rads^{-1}, fast enough to generate a turbulent shear flow that extends to within approximately 1.5 cm of the bottom surface of the tank in each case.

Pictures of the ice are taken from the side of the tank at 1-minute intervals with a Nikon D800 camera. The ice thickness is subsequently measured from these pictures using GraphClick, a digitizer software. Seven thermistors are placed on a 5.25-cm-long vertical strip starting from the bottom of the tank to measure temperature at the locations shown in figure 2.3. The strip is placed

along the wall of the tank and the thermistors protrude 1 cm into the tank. The thermistors are connected to a datalogger. We focus on the ice thickness at a radial distance $R = 13$ cm from the tank center, that is, 4.5 cm from the outer wall. This location is a compromise between its proximity to the thermistor chain and its separation from the immediate effects of the outer wall.

Both the friction velocity and fluid velocity of the turbulent shear flow are measured over the entire range of lid angular velocities. The average shear stress, and hence friction velocity, is obtained by measuring the torque on the lid with a torque meter. The fluid velocity is obtained from planar PIV measurements. The water is seeded with nearly spherical glass beads of specific gravity 1.1 and average diameter 10 μm and illuminated with a pulsed Nd:YAG laser sheet. A vertical light sheet is set up along a chord at $r = R$ to measure the vertical profile of the azimuthal component of the velocity. To measure the radial component of the velocity, a horizontal light sheet is set up to illuminate a sector of the tank's circular cross-sectional area at different heights above the bottom plate. A high-speed CMOS camera synchronized with the pulsed laser taking double exposure images at a resolution of 2048×2048 pixels is oriented vertically above the tank and horizontally to the side of the tank, for imaging the radial flow and azimuthal flow, respectively. The open source software PIVlab (Thielicke & Stamhuis, 2014) is used to calculate PIV velocities from the exposures. For the determinations of the azimuthal velocity profiles, only a vertical strip at the center of the images taken from the side, in which the particles move in the plane of the light sheet, is used in the analysis.

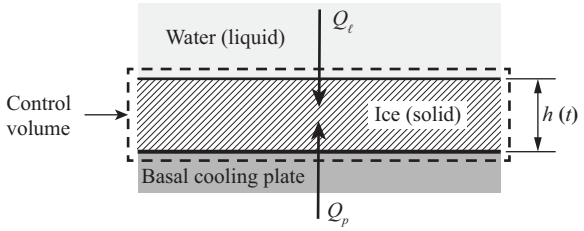

Figure 2.4: Control volume around ice

2.3 Ice energy balance

The energy (enthalpy) balance in a control volume enclosing the ice with thickness h at a time t shown in figure 2.4 yields the following relationship:

$$\frac{\mathrm{d}E}{\mathrm{d}t} = Q_p + Q_\ell, \tag{2.1}$$

where E is the energy (enthalpy) content of the ice, the subscript p refers to the plate, and Q is the heat entering the control volume from the region denoted by its subscript. Considering a one-dimensional energy balance, E and Q_p can be expressed as

$$E = \rho_s c_s \int_0^h \overline{T_s}\ \mathrm{d}z - \rho_s L h \tag{2.2}$$

and

$$Q_p = -\frac{k_s \Delta T_s}{h}. \tag{2.3}$$

In (2.2) and (2.3), k is thermal conductivity and T is temperature. $\Delta T_s = T_f - T_p$, where T_f is the freezing temperature of water (also the temperature of the ice–water interface). $\overline{T_s}$ is the average temperature of the ice. Assuming that the temperature varies linearly in the vertical direction through the ice, $\overline{T_s} = (T_f + T_p)/2$. Numerical values of the physical properties of water and ice are given in table 2.2. The first term on the right-hand side in (2.2) can be

Property	Units	Liquid water	Solid ice
Freezing temperature, T_f	K		273.15 [b]
Density, ρ	kg m^{-3}	999.8 [a]	916.7 [b]
Specific latent heat of fusion, L	J kg^{-1}		3.33×10^5 [b]
Isobaric specific heat capacity, c	J kg^{-1} K^{-1}	4.21×10^3 [a]	2.10×10^3 [b]
Thermal conductivity, k	W m^{-1} K^{-1}	0.556 [b]	2.16 [b]
Kinematic viscosity, μ	Pa s	1.79×10^{-3} [b]	
Thermal expansion coefficient, β	K^{-1}	6.77×10^{-5} [c]	160 [b]

Table 2.2: Physical properties of liquid water and ice at standard atmospheric pressure. ρ, L, c, k, μ, and β at 273.15 K. β for liquid water is linear and β for solid ice is volumetric. [a] From Wagner & Pruß (2002), [b] from Haynes (2015), and [c] from IOC *et al.* (2010).

rewritten as

$$\rho_s c_s \int_0^h \overline{T_s}\ \mathrm{d}z = \rho_s c_s h \left(\frac{\Delta T_s}{2} + T_p \right). \tag{2.4}$$

2.3.1 No turbulent mixing

When the ice is growing in quiescent water, heat is transferred by conduction. We ignore free convection in the liquid. In this case Q_ℓ is the sum of the conductive heat transfer through and the rate of change of enthalpy of the liquid, so that

$$Q_\ell = \frac{k_\ell \Delta T_\ell}{\delta} + \rho_s c_s T_f \frac{\mathrm{d}h}{\mathrm{d}t} \tag{2.5}$$

where the subscript ℓ refers to the liquid properties, δ is the thickness of the thermal boundary layer above the ice, and $\Delta T_\ell = T_\infty - T_f$, T_∞ being the temperature of the liquid far-field. Introducing

$$\delta = \frac{\alpha_\ell}{\mathrm{d}h/\mathrm{d}t} \tag{2.6}$$

from the heat balance in a control volume in the liquid region above the ice–water interface, with α_ℓ given by

$$\alpha_\ell = \frac{k_\ell}{\rho_\ell c_\ell}, \tag{2.7}$$

the conductive term in (2.5) can be rewritten as

$$\frac{k_\ell \Delta T_\ell}{\delta} = \rho_\ell c_\ell \Delta T_\ell \frac{\mathrm{d}h}{\mathrm{d}t}. \tag{2.8}$$

Substitution of (2.2), (2.3), (2.4), (2.5), and (2.8) into (2.1) gives, for the heat balance in the control volume,

$$\left(\rho_s L + \frac{\rho_s c_s \Delta T_s}{2} + \rho_\ell c_\ell \Delta T_\ell\right)\frac{\mathrm{d}h}{\mathrm{d}t} = \frac{k_s \Delta T_s}{h} + \frac{\rho_s c_s h}{2}\frac{\mathrm{d}}{\mathrm{d}t}(\Delta T_s), \tag{2.9}$$

which can be approximated, based on the largest terms, as

$$(\rho_s L + \rho_\ell c_\ell \Delta T_\ell)\frac{\mathrm{d}h}{\mathrm{d}t} \simeq \frac{k_s \Delta T_s}{h}. \tag{2.10}$$

This equation is non-dimensionalized by taking the length scale to be the depth D of the liquid, the temperature difference scale to be the temperature difference across the solid at the onset of turbulent mixing, and the time scale to be D^2/α_ℓ, which corresponds to the characteristic time for thermal diffusion over the distance D. This yields

$$\left[\frac{1}{St} + \mathcal{C}(\Delta T_\ell)^*\right]\frac{\mathrm{d}h^*}{\mathrm{d}t^*} = \frac{1}{A}\frac{(\Delta T_s)^*}{h^*}. \tag{2.11}$$

where variables with a superscript $*$ are in non-dimensional form. $\mathcal{C} = \rho_\ell c_\ell / \rho_s c_s$ is the ratio of the volumetric heat capacity of the liquid to that of the solid and $A = \alpha_\ell / \alpha_s$ is the ratio of the thermal diffusivity of the solid to that of the liquid. The typical values of $\mathcal{C}$ and A for the laboratory experiment and for the geophysical application are listed in table 2.1.

2.3.2 Turbulent mixing

For turbulent flow over a flat plate at constant temperature, Reynolds analogy relates the convective heat flux q_T to the properties of the momentum boundary layer. In Reynolds analogy, the heat flux and momentum flux at the plate in a turbulent boundary layer are considered equivalent since they are both influenced by the turbulent motion above the plate. The expression for q_T (see White, 1974, p. 564) is

$$q_T = \rho_\ell U_\infty c_\ell \Delta T_\ell C_h \tag{2.12}$$

where C_h is a heat-transfer coefficient (Stanton number) given empirically by

$$C_h = \frac{c_f/2}{1 + 12.8(Pr^{0.68} - 1)\sqrt{c_f/2}}, \tag{2.13}$$

U_∞ is the velocity of the liquid in the far-field, Pr is the Prandtl number, and c_f is the coefficient of friction defined as

$$c_f = 2\frac{u_*^2}{U_\infty^2} \tag{2.14}$$

where u_* is the friction velocity. We introduce the coefficient G in the expression for C_h to substitute for the constant term $12.8(Pr^{0.68} - 1)$. In the context of our experiment, this term is the term we are trying to constrain. For the turbulent mixing phase in our experiments, Q_ℓ is augmented by q_T, and hence the energy balance for the control volume becomes

$$(\rho_s L + \rho_\ell c_\ell \Delta T_\ell)\frac{\mathrm{d}h}{\mathrm{d}t} \simeq \frac{k_s \Delta T_s}{h} - \rho_\ell U_\infty c_\ell \Delta T_\ell C_h. \tag{2.15}$$

By using the same length, temperature difference, and time scales as in (2.11) and by additionally using U_∞ as the velocity scale, this expression is non-

dimensionalized to obtain

$$\left[\frac{1}{St} + \mathcal{C}(\Delta T_\ell)^*\right]\frac{\mathrm{d}h^*}{\mathrm{d}t^*} = \frac{1}{A}\frac{(\Delta T_s)^*}{h^*} - RePr\mathcal{C}(\Delta T_\ell)^* C_h, \tag{2.16}$$

where $RePr = Pe$. Table 2.1 lists typical values of Pe for the sub-ice shelf cavity and the laboratory set-up.

2.4 Experimental results

We conducted a set of eleven experiments at different angular velocities of rotation Ω of the lid. The value of Ω for each experiment is listed in table 2.3. Experiment 0 is a null experiment in which the lid was not rotated, and hence the water was not mixed by turbulence over the whole duration. The lid Re at a radius r, Re_r, in the tank is defined as

$$Re_r = \frac{(\Omega r)D}{\nu}. \tag{2.17}$$

When Ωr is taken as the velocity scale U, this definition of Re is the same as in table 2.1. The value of Re_r at $r = R$, which we denote by Re_R, for each experiment is given in table 2.3. We refer to the first portion of each experiment in which ice grows by conduction in still water as Phase 1 and the second portion of each experiment in which there is a turbulent shear flow and mixing as Phase 2.

We conducted a separate test to estimate the heat flux through the tank wall during Phase 2 of a typical experiment. A set of thermistors was placed on the external surface of the tank to measure its temperature, which was used to estimate the temperature difference across the tank wall. At the end of the turbulent mixing phase of the experiment, when the liquid inside the tank is

Experiment	Ω (rad/s)	Lid Re_R	Regime
0	0	0	
1	0.27	2.0×10^3	Attenuated growth
2	0.32	2.3×10^3	Partial Melting
3	0.45	3.3×10^3	Partial Melting
4	0.60	4.4×10^3	Partial Melting
5	0.71	5.2×10^3	Partial Melting
6	0.82	5.9×10^3	Complete Melting
7	0.98	7.1×10^3	Complete Melting
8	1.14	8.3×10^3	Complete Melting
9	1.31	9.5×10^3	Complete Melting
10	1.43	1.0×10^4	Complete Melting

Table 2.3: Angular frequency Ω of lid and lid Re_R in experiments

coldest, the heat flux through the tank wall is about 3% of the turbulent heat flux from the liquid to the ice-water interface in the interior of the tank.

2.4.1 Ice thickness

Measured ice thickness h_e versus time is shown in figures 2.5 and 2.6, from Experiments 1–10 and Experiment 0 respectively. In figure 2.5 the time $t = 0$ corresponds to the onset of the turbulent shear flow. In figure 2.6, the shaded region along the line plot has a total width of 0.5 mm and represents the error in the measurements. The error was estimated by taking the standard deviation of 10 repeated measurements of the ice thickness at $r = R$ during Phase 1 of a typical experiment. The ice thickness measurements in Experiment 0 and in Phase 1 of Experiments 1–10 are assigned the same error estimate.

The error in Phase 2 measured by the same method, using Phase 2 measurements from a typical experiment, is 0.9 mm. The error in ice thickness measurements in Phase 2 is larger than in Phase 1 because the ice–water inter-

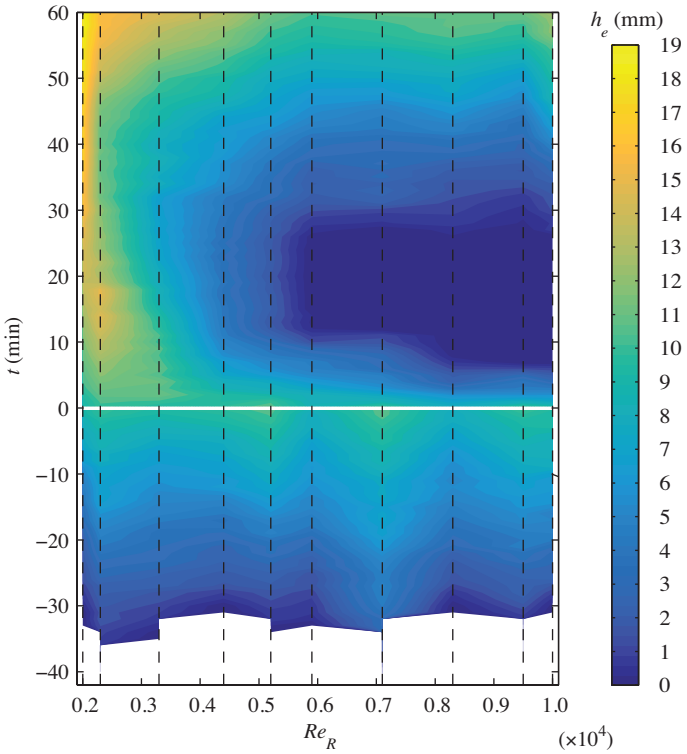

Figure 2.5: Ice thickness at $r = R$ over the course of Experiments 1-10. The vertical axis denotes the time relative to the onset of turbulent mixing in each experiment. The horizontal white line indicates the onset of mixing and dashed vertical black lines indicate the Re_R of each experiment. The contour plot has been constructed by linearly interpolating measurements from the 10 distinct experiments.

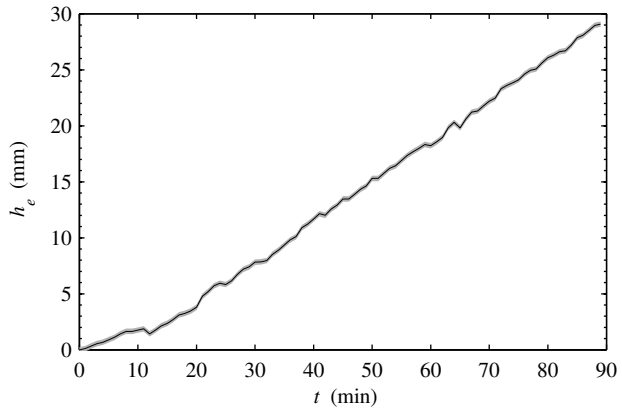

Figure 2.6: Ice growth in Experiment 0 (with no shear flow)

face becomes wavy when ice melts in the presence of the turbulent flow. The wavy pattern consists of spiral crests and troughs with wavelength 12–16 mm and amplitude 1–3 mm. It is difficult to visually identify the ice thickness along the diameter from the side-view pictures of the tank due to the waviness of the ice surface.

Ice grows at an almost constant rate when the water is undisturbed, as in Experiment 0 and in Phase 1 of Experiments 1–10. In Phase 2, mixing by the turbulent shear flow transports warm water from the far-field to the ice–water interface, which promotes heat transfer to the ice. The ice then responds in one of three ways, each of which we have observed as a transient at our measurement location $r = R$: (1) attenuated ice growth, (2) partial melting, and (3) complete melting. Attenuated growth refers to ice growing at a rate slower than during Phase 1. Partial melting refers to only a fraction of the ice thickness from Phase 1 changing phase into liquid, such that a residual thinner ice layer still remains in the tank. Complete melting refers to the whole ice layer from Phase 1 changing phase into liquid. Following this transient response, re-growth of ice

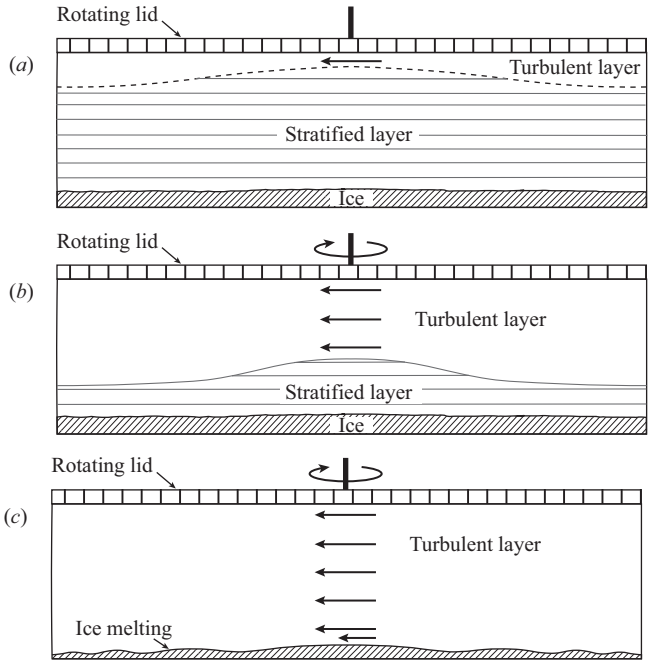

Figure 2.7: Changes in the liquid layer following the onset of turbulent mixing. At the lower end of experimental Re_R, the steps shown in this diagram occur over several minutes, whereas at the upper end of experimental Re_R, they occur in a few seconds. (a) A stratified layer initially separates the turbulent layer from the ice surface. The interface between the stratified layer and turbulent layer is dome-shaped. (b) The turbulent layer progresses downwards, eroding the stratified layer. (c) The turbulent layer has reached the ice–water interface and causes the ice to melt. The thickness of ice melted increases with radius. A spiral wavy profile develops on the ice surface during melting.

at the same rate as in Phase 1 is observed.

Figure 2.7 shows the sequence of structures that are observed in the ice–water system following the onset of turbulent mixing. A thermally stratified water layer initially separates the growing ice from the turbulent flow, as the turbulence develops beneath the rotating lid. The interface between the stratified layer and the turbulent flow is dome-shaped because the turbulent shear stress τ increases proportionally to r^2 and is therefore weaker near the center of

the tank. The dome-shaped interface was imaged in the experiments by inserting dye at the top of the water column into the turbulent layer and monitoring the evolution of the turbulent layer. In our lowest Re_R experiment, the stratified layer persists in the presence of the shear flow, thereby preventing turbulence from reaching the ice–water interface. Ice growth is attenuated in this case, but not stopped. At the other extreme, in our highest Re_R experiments, the turbulent mixing is strong enough to erode the stratified layer entirely almost immediately after the onset of the turbulent shear flow. When the turbulence comes in direct contact with the ice–water interface, it produces complete melting at high Re_R and partial melting at intermediate Re_R. In the partial melting cases, the thickness of ice melted increases with radial distance from the tank center. In table 2.3, the transient behavior the ice adopts at $r = R$ in response to turbulent mixing in Experiments 1–10 is given along with the corresponding Re_R.

The development of the spiral wavy pattern on the ice–water interface when ice melts in our experiments has been explained by Gilpin *et al.* (1980), as follows. Although the ice thickness is approximately uniform at the end of Phase 1, there are nevertheless small-amplitude deviations from uniform thickness due to random perturbations and minor design flaws in the cooling apparatus. Gilpin *et al.* (1980) found that such an interface will be unstable to growth in the presence of turbulence when the heat flux from the liquid to the solid is large, which is the case in our experiments during transient melting. The mechanism for the instability involves flow separation downstream of an irregularity in the ice, which causes the heat transfer at a crest to be smaller than the heat transfer at a valley. The amplitude of the irregularity thus grows, which further amplifies

the irregularity in the shear flow, producing a growing set of undulations on the ice–water interface as it melts. The wavelength of the undulations increases with u_*, which is proportional to r in our experiments. The dependence of the undulation wavelength on distance from the tank center gives rise to the spiral profile of the ice–water interface undulations that we observe.

2.4.2 Temperature

Thermistors A–G are used to measure the temperature at the heights indicated in figure 2.3. The resistance $\mathcal{R}$ of a thermistor is related to its temperature T according to the Steinhart-Hart equation,

$$\frac{1}{T} = a_1 + a_2 \ln \mathcal{R} + a_3 (\ln \mathcal{R})^3, \tag{2.18}$$

where a_1, a_2, and a_3 are the Steinhart-Hart coefficients and are unique to each thermistor. We obtained these coefficients by calibration prior to our series of experiments.

Temperature is recorded starting from the instant nitrogen starts to circulate inside the basal cooling plate. The evolution of temperature at the thermistor locations A–G in a typical experiment (in this case, Experiment 6) is shown in figure 2.8. Occasional outliers in the thermistor readings have been deleted and the data points have been replaced by interpolating neighboring values. These outliers are due to the thermistor connections occasionally freezing, causing sudden resistance increases which are seen as sudden temperature drops. Following the onset of turbulent mixing, there is an increase in temperature at A because warm water transported to the bottom of the tank causes melting of ice. At that time, thermistors B, C, D, E, F, and G record the same temperature, signaling

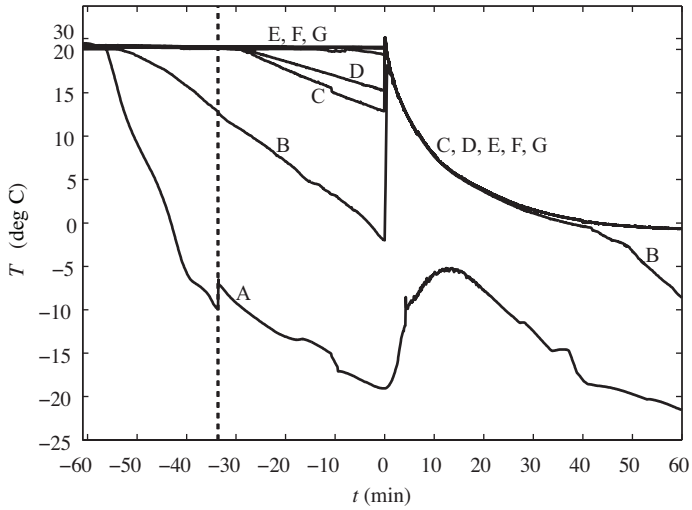

Figure 2.8: Temperature recorded by thermistors A, B, C, D, E, F, and G over the course of a typical experiment. The horizontal axis denotes time relative to the onset of turbulent mixing. The vertical dashed line indicates the time at which ice forms a thin layer on the bottom plate.

that mixing results in a homogeneous distribution of temperature in the turbulent shear flow. Note that after about 40 minutes of cooling, the temperature at B departs from the temperatures at C, D, E, F, and G as thermistor B is engulfed by the growing ice.

Vertical profiles of temperature in the same experiment at the indicated times during Phase 1 and Phase 2 are shown in figures 2.9(a) and 2.9(b) respectively. Because the ice–water interface is at $T_f = 0$ °C, the measured ice thickness at any time can be checked by interpolating T_f in the temperature time series recorded by thermistors A–G. The temperature within the ice can safely be assumed to increase linearly from the temperature of the plate to T_f, because heat transfer in the ice is by conduction and its growth rate is slow enough that the ice is in thermal equilibrium with its boundaries. The linear

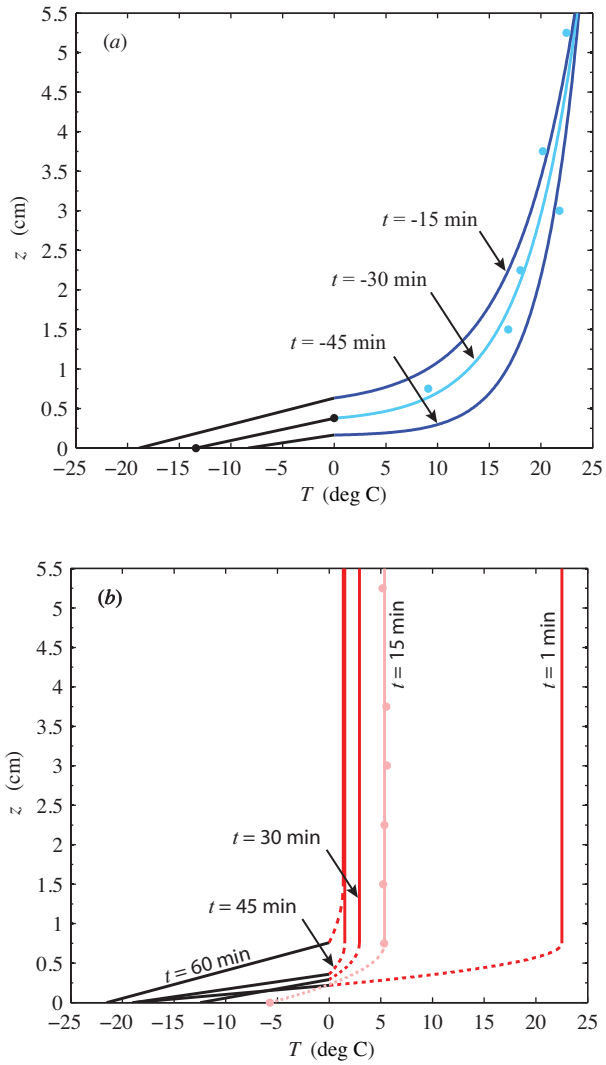

Figure 2.9: Vertical profiles of temperature at different times relative to the onset of turbulent mixing during (a) Phase 1 and (b) Phase 2 of a typical experiment. The temperature data points are shown for the $t = -30$ min profile in (a) and for the $t = 15$ min profile in (b). In (b), a dashed line is drawn between the location of the ice–water interface and the location of the first thermistor above the ice–water interface to indicate a possible temperature profile in that layer. (Colour online) Liquid temperature profiles in Phase 1 are in blue and liquid temperature profiles in Phase 2 are in red.

distributions of ice temperature are shown by the straight lines in the left half of figures 2.9(a) and 2.9(b). Temperature profiles above the ice–water interface in Phase 1 (figure 2.9a) are exponential fits to the temperature measurements. For clarity, the temperature data points corresponding to only one profile have been included in each figure. The fitted liquid layer temperature profiles in Phase 1 are characteristic of heat transfer in the liquid by conduction only.

We saw no evidence of natural convection in the liquid layer during Phase 1. For a liquid water layer over an ice–water interface at 0 °C, natural convection onsets at Rayleigh numbers above 1700, which has been confirmed experimentally by Boger & Westwater (1967). The Rayleigh number for this system can be expressed as

$$\text{Rayleigh} = \frac{d^3 \beta \rho_\ell^2 g c_\ell (\Delta T)}{\mu k_\ell} \tag{2.19}$$

where β is the thermal expansion coefficient of water, d is the convecting layer depth, and ΔT is the temperature difference across d. Boger & Westwater (1967) take d to be the thickness of the liquid layer between the ice–water interface and the height at which the water is at 4 °C, where it has maximum density. Interpolating the value of d from the temperature measurements in Phase 1 of our experiments and using values from table 2.2 for the physical properties of water, we found that the Rayleigh number in Phase 1 varies from 250 to about 850. It therefore remains below the critical Rayleigh number at which natural convection would occur.

As the liquid cools by conduction in Phase 1 of an experiment, the temperature T in its thermal boundary layer can be modelled according to the relation

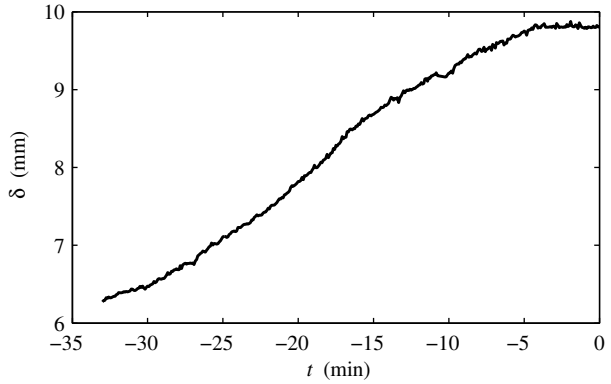

Figure 2.10: Boundary layer thickness δ calculated from exponential fit through non-dimensionalized vertical temperature time series

$$\frac{T - T_f}{T_\infty - T_f} = 1 - \mathrm{e}^{-(z-h_e)/\delta}, \ z \geq h_e. \tag{2.20}$$

The thickness δ of the thermal boundary layer can be obtained by taking the reciprocal of the fit coefficient of an exponential fit to this relationship. Figure 2.10 shows the evolution of δ calculated in this way in Phase 1 of the same experiment. The initial value of δ is non-zero because, prior to the formation of ice, a thermal boundary layer was already present in the liquid due to cooling from the bottom by the basal cooling plate. The thickness of the thermal boundary layer increases from its initial value as Phase 1 of the experiment proceeds. This indicates that, for a control volume in the liquid above the ice–water interface, the heat loss by conduction to the ice is larger than the enthalpy decrease of the control volume due to the movement of the ice–water interface into it. At the end of Phase 1, δ asymptotes to a uniform value. At this stage, the energy balance in the control volume above the ice–water interface is at steady-state, that is, conductive heat loss to the ice is balanced by enthalpy decrease due to the upward movement of the ice–water interface.

A simple one-dimensional model for the energy balance in the control volume gives $\delta = \alpha_\ell/(\mathrm{d}h_e/\mathrm{d}t)$. The predicted value of δ from this model for our case is 20 mm, which is about twice as large as the steady-state value of δ from figure 2.10. The rate of growth of ice, $\mathrm{d}h_e/\mathrm{d}t$, is very small in our experiment (about 5.5×10^{-3} mms^{-1}). There is very little liquid convective motion in the control volume above the ice–water interface in response to the very-slowly-moving interface, and hence, the thermal boundary layer is thinner than the theoretical prediction.

During Phase 2 of these experiments, all of the thermistors in the liquid typically record nearly the same temperature at a given time after the initial thermal stratification in the liquid has been destroyed by turbulent mixing. A vertical line through the mean of the temperatures measured by the thermistors in the liquid is drawn in figure 2.9(b) to represent a homogeneous vertical temperature profile in the liquid layer.

2.4.3 Velocity

Application of the heat balance shown in (2.15) to the control volume around the ice–water interface in figure 2.4 requires knowledge of the fluid velocity in the far-field. Since the temperature distribution in the liquid is nearly homogeneous when there is turbulent mixing, buoyancy forces in the liquid are weak during this phase of the experiments. The circulation in the far-field is thus due to the shear induced by the rotating lid only.

The velocity of the shear-driven turbulent flow above the flat bottom surface of the tank is measured for the purpose of relating the fluid velocity in the far-field to the lid velocity. We denote by $\overline{U_\theta}$ the mean of the azimuthal velocity

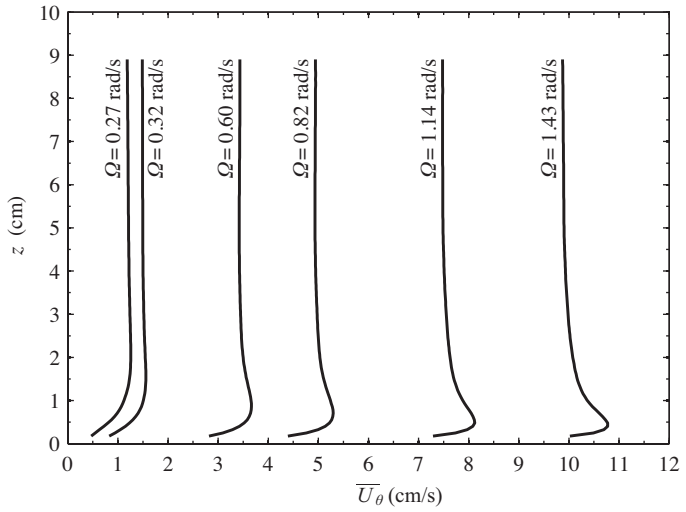

Figure 2.11: Mean azimuthal velocity in the fluid column at $r = R$ for different angular velocities of the lid

component and by $\overline{U_r}$ the mean of the radial velocity component of the flow. The vertical profiles of $\overline{U_\theta}$ corresponding to different lid angular velocities are shown in figure 2.11. They were obtained by horizontally averaging the horizontal component of the velocity vectors from PIV measurements in a vertical strip at $r = R$. Figure 2.12 shows $\overline{U_r}$ at different radial distances, including $r = R$, at a height of 0.5 cm and 7 cm above the basal cooling plate. The radial component of the velocity vectors from PIV measurements in a horizontal sector at these heights were averaged to obtain these profiles of $\overline{U_r}$.

The $\overline{U_\theta}$ plots show the presence of a thin boundary layer near the bottom plate. For higher angular frequencies of rotation Ω of the lid, $\overline{U_\theta}$ has a maximum within the boundary layer. We interprete this maximum to be due to the transfer of angular momentum from the flow near the wall along the bottom plate to the flow in the interior of the tank along the bottom plate. Above the boundary layer, there is a core region with uniform $\overline{U_\theta}$ that extends almost to

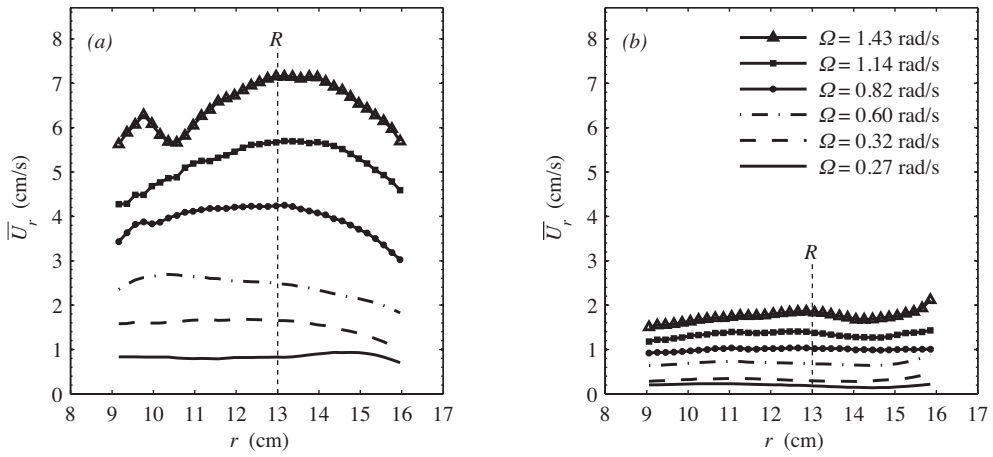

Figure 2.12: Mean radial velocity at heights of (a) 0.5 cm and (b) 7 cm above the bottom plate. Positive values correspond to inward direction. The vertical dashed line in (a) and (b) is at $r = R$ where the ice thickness measurements are taken.

the top of the fluid column. This uniform core can therefore be considered to be in solid body rotation. The velocity in the thin boundary layer near the rough underside surface of the lid has been omitted from the profile as it was difficult to obtain accurate measurements of velocity in that thin layer by PIV due to light reflections from the rough grid degrading the quality of the images. The far-field $\overline{U_\theta}$ is 34% of the lid velocity at the lowest lid Re and 53% of the lid velocity at the highest lid Re. $\overline{U_r}$ is 3-4 times larger inside the bottom boundary layer than in the interior of the fluid column. The turbulent flow between a rotating disk and a stationary disk has been studied experimentally by Itoh *et al.* (1992) and Cheah *et al.* (1994) and numerically using LES by Andersson & Lygren (2006). Itoh *et al.* (1992) also report the presence of an inner core in which $\overline{U_\theta}$ is homogeneous. Denoting $K = \frac{\overline{U_\theta}}{\Omega r}$, they found K in the range 31% to 42% for local Re ($= \Omega r^2/\nu$) from 1.6×10^5 to 8.8×10^5, which corresponds to 1.3×10^4

to 7.1×10^4 with the definition of Re in (2.17). $\overline{U_r}$ in their experiment was directed inwards in the boundary layer near the stationary plate and was zero in the inner core. In our experiments, the larger values of K at Re one order of magnitude smaller and the non-zero $\overline{U_r}$ in the inner core can be attributed to the roughness of the top boundary, which affects the circulation in the tank by causing enhanced mixing.

2.4.4 Friction Velocity

The heat balance in (2.15) also requires knowledge of the friction velocity u_* of the shear-driven flow. Here u_* is defined as

$$u_* = \sqrt{\frac{\tau(\Omega, r)}{\rho}} \tag{2.21}$$

where τ is the shear-stress on the lid, which is given by

$$\tau = C_D \rho_\ell \Omega^2 r^2 \tag{2.22}$$

with C_D being the drag coefficient associated with the lid. Taking $\mathrm{d}F$ to be the incremental change in force along an incremental change in radial distance $\mathrm{d}r$ from the center and Γ to be the torque on the lid, Γ and $\mathrm{d}F$ are related to C_D by

$$\mathrm{d}F = C_D \rho_\ell \Omega^2 r^2 (2\pi r \mathrm{d}r) \tag{2.23}$$

and

$$\Gamma = \int_0^R r \ \mathrm{d}F, \tag{2.24}$$

so that

$$\Gamma = \frac{2}{5} \pi C_D \rho_\ell \Omega^2 R^5. \tag{2.25}$$

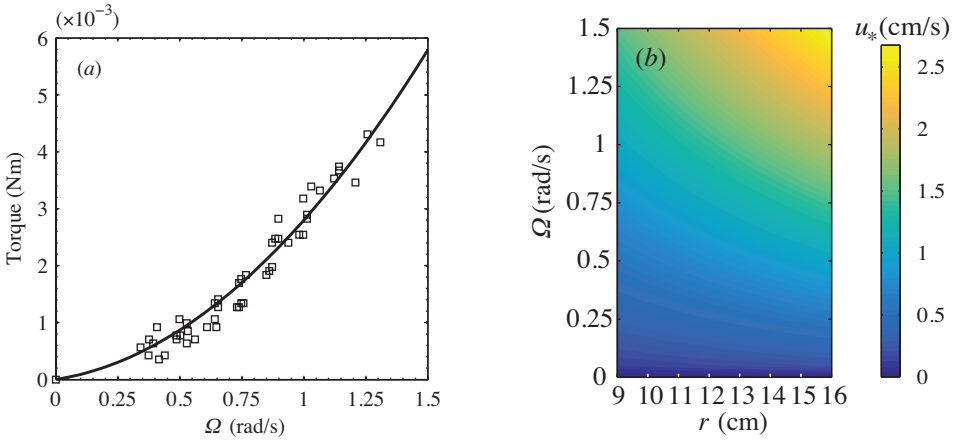

Figure 2.13: (a)Torque on the lid for a water depth of 10 cm: □, measurements; ——: line of best fit. (b) friction velocity u_* calculated from torque measurements.

Hence u_* can be determined from Γ according to the relation

$$u_* = \sqrt{\frac{5\Gamma}{2\pi\rho_\ell R^5}}r \tag{2.26}$$

The torque on the lid for different angular velocities of rotation is shown in figure 2.13(a). The line of best fit is a weighted-by-value two-parameter polynomial. The friction velocity derived from the torque measurements using (2.26) is shown in figure 2.13(b).

2.5 Model Comparison

2.5.1 Ice thickness

Our heat balance for the ice–water interface can be integrated in time to model the evolution of ice thickness in the experiments conducted with (2.10) used for Phase 1 and (2.15) used for Phase 2. In what follows, the modelled ice thickness is denoted by h_m. The values listed in table 2.2 for the properties of liquid water

and solid ice are used in the integration. ΔT_s and ΔT_ℓ in the heat balance are calculated in the following way:

$$\Delta T_s = \begin{cases} T_f - T_A, & \text{when ice is present,} \\ 0, & \text{when there is no ice,} \end{cases} \tag{2.27}$$

$$\Delta T_\ell = \begin{cases} T_G - T_f, & \text{when ice is present,} \\ T_G - T_A, & \text{when there is no ice.} \end{cases} \tag{2.28}$$

T_A refers to temperature measurements at thermistor A, which is located in a small hole in the basal cooling plate, and T_G refers to temperature measurements at thermistor G, which is located 5.25 cm above the basal cooling plate. The fluid velocity in the far-field, U_∞, is determined using the measurements of $\overline{U_\theta}$ and $\overline{U_r}$ interpolated at the angular velocity of the lid at a height $z = 7$ cm:

$$U_\infty = \sqrt{\overline{U_\theta(z)}^2 + \overline{U_r(z)}^2}, \ z = 7 \text{ cm}. \tag{2.29}$$

The friction velocity u_*, which is used in calculating the coefficient of friction c_f defined in (2.14), is determined from the calibration shown in figure 2.13(b). The equations are integrated by a second-order Runge-Kutta method, with the initial condition for h_m being zero. Because the temperature measurements were taken at intervals of 5 s, the time-step for integration is also 5 s.

In Phase 2, the heat flux q_T from the turbulent flow at the ice–water interface depends on the coefficient G. For the Pr of water at 0 °C, which is listed in table 2.1, G becomes 62.7. We denote this value by G_0. The expression for G is an empirical expression derived for a turbulent boundary layer in air over a perfectly flat plate (White, 1974). Using a range of values of G, including G_0, we evaluate h_m during Phase 2 of Experiments 2–10. We also calculate the root

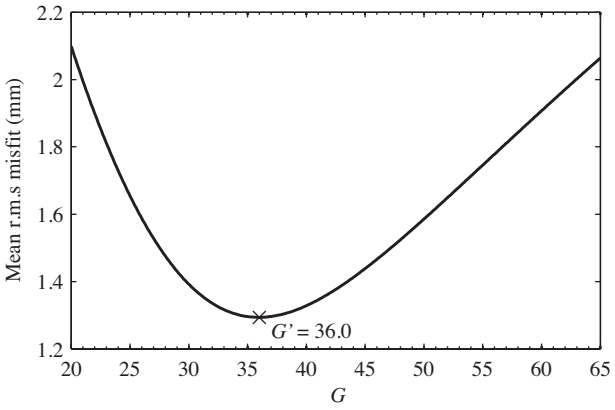

Figure 2.14: Misfit to (2.15) versus G

mean square (r.m.s) difference Δh_{RMS} between h_e and h_m at the corresponding times. The omission of Experiment 1 from this comparison will be explained when interpreting figure 2.15(d). The mean of Δh_{RMS} for the range of values of G considered is plotted in figure 2.14. Its minimum occurs when $G = 36.0$. The heat flux from the turbulent layer at the ice–water interface is therefore more closely approximated using this value of G, which will be denoted by G'. The fact that G' is smaller than G_0 indicates that heat transfer from a turbulent flow at an ice–water interface is more efficient than at a flat plate. This enhanced heat transfer can be attributed to the ice surface not being uniformly smooth, especially during melting when it develops a wavy profile, since a rough surface has a greater surface area than a flat surface and hence allows for greater heat transfer. With the new value G', the heat transfer coefficient C_h from the turbulent flow at the ice–water interface given in (2.12) is related to (u_*/U_∞) by the power law $C_h = 0.028(u_*/U_\infty)^{1.09}$.

G' is substituted in (2.15) to calculate h_m for Phase 2 of Experiments 1–10. Figure 2.15 shows the comparison between h_e and h_m in Experiments 8, 5, 3,

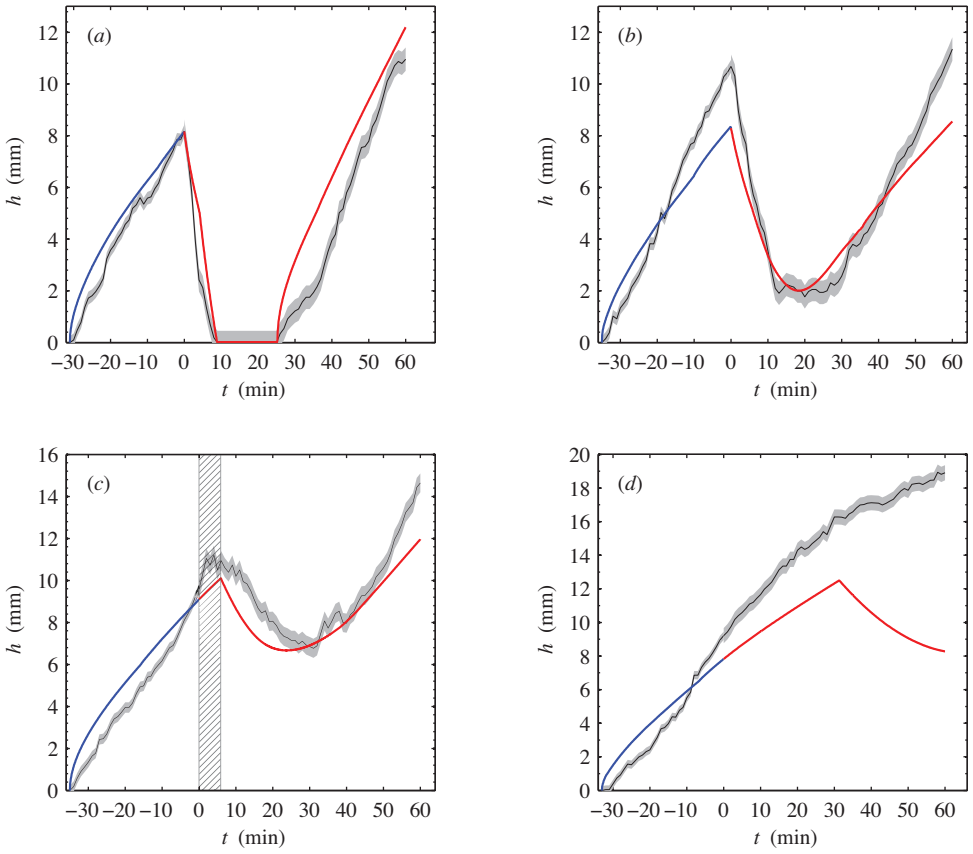

Figure 2.15: Comparison of h_e (thinner solid line with shaded error region) with h_m (thicker solid line) from (a) Experiment 8, (b) Experiment 5, (c) Experiment 3, and (d) Experiment 1. For $t < 0$, the error in h_e is 0.5 mm and for $t > 0$, it is 0.9 mm. The hatched region in (c) is discussed in the text. (Colour online) For the h_m plots, the blue portion corresponds to ice thickness evolution in Phase 1 while the red portion corresponds ice thickness evolution in Phase 2.

and 1. There is good agreement between h_e and h_m in Experiments 8, 5, and 3 but not in Phase 2 of Experiment 1. After the onset of turbulent mixing in Experiment 1, a stratified layer remained between the turbulent layer and the ice–water interface up to $t = 33$ min. This was evidenced by the behavior of dye inserted into the turbulent layer, which showed that a clear, stratified layer over the ice–water interface prevented the dyed turbulent layer from reaching the ice surface. Accordingly, the ice growth in that time interval is modelled using (2.10). For this case, the measured rate of ice growth is larger than predicted, a difference which occurs because the stratified layer over the ice–water interface inhibits heat transfer from the liquid far-field. Ice grows below the turbulent layer from $t = 0$ to $t = 33$ min, at which time it reaches the turbulence. For $t > 33$ min, h_m is modelled using (2.15). The model predicts melting whereas the experimental measurements indicate attenuated growth. The disagreement between h_e and h_m in Experiment 1 reveals a limitation of our model. At the lower end of the range of Re_R we investigate, the applied shear stress from the lid is low, and consequently the turbulence is too weak to erode the stratified layer quickly. Our model, however, assumes that the stratified layer gets eroded quickly at low values of Re_R.

A stratified layer is present in Experiments 2–4 for a short time interval following the onset of turbulent mixing. Although the theoretical model given by (2.10) is incomplete for this configuration, we use it to approximate h_m until the time when the turbulent layer comes into contact with the ice. h_m is consistently lower than h_e in that time interval, as shown in the hatched region of figure 2.15(c) for Experiment 3. In the determination of G' previously discussed, h_e and h_m from time intervals when a stratified layer was present

were not used.

The contour plot of h_m calculated using the theoretical model with G' for Experiments 2–10 is shown in figure 2.16. Experiment 1 is omitted because it is a case for which our model is not valid. The region corresponding to Experiment 1 in figure 2.16 is hatched. The absolute difference between h_e from figure 2.5 and h_m at corresponding times is shown in figure 2.17. The absolute difference is generally close to the error margin of 0.5 mm for Phase 1 and 0.9 mm for Phase 2, which indicates good agreement between the model and the experiment. The hatched area in figure 2.17 corresponds to Experiment 1 and time intervals when a stratified layer was present during Phase 2 of the experiments. The absolute difference between h_e and h_m in these intervals during Phase 2 was omitted from the contour plot because the model assumes that the stratified layer is eroded more rapidly and hence deviates from the experimental measurements.

We did not observe evidence of the radial component of the flow near the bottom of the tank during turbulent mixing affecting the evolution of ice in our set of experiments. The radial component of the flow is stronger at higher Re_R. In all experiments in which there is transient melting, the rate at which the ice melts always increases with distance from the center of the tank. During the subsequent re-freezing, the rate of ice growth is always uniform at all radial distances. These observations suggest that the far-field flow has a stronger influence on the evolution of ice than the radial flow near the bottom of the tank.

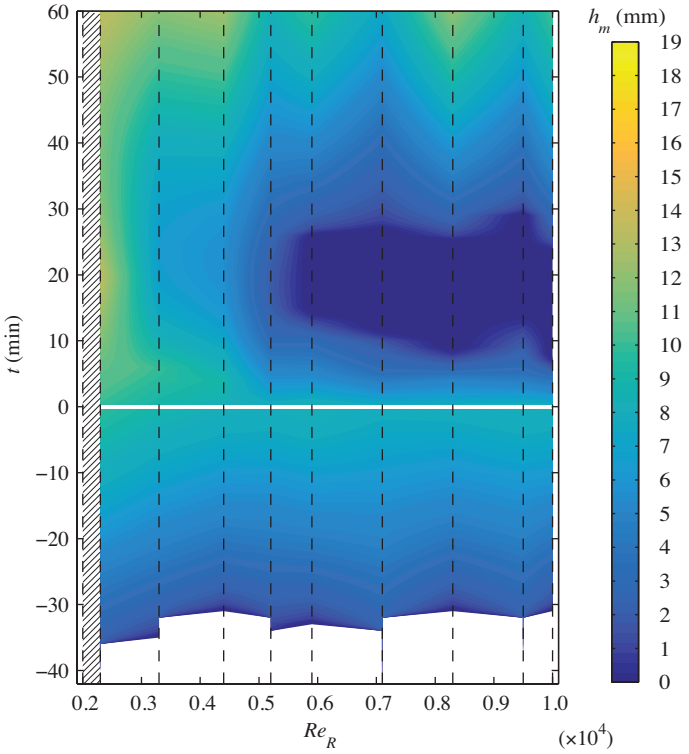

Figure 2.16: Contour plot of h_m for Re_R corresponding to Experiments 2–10. The white line represents the onset of turbulent mixing, the dashed vertical black lines indicate the Re_R of the experiments, and the contour plot is filled by linearly interpolating modelled ice thickness values at the distinct Re_R of the experiments.

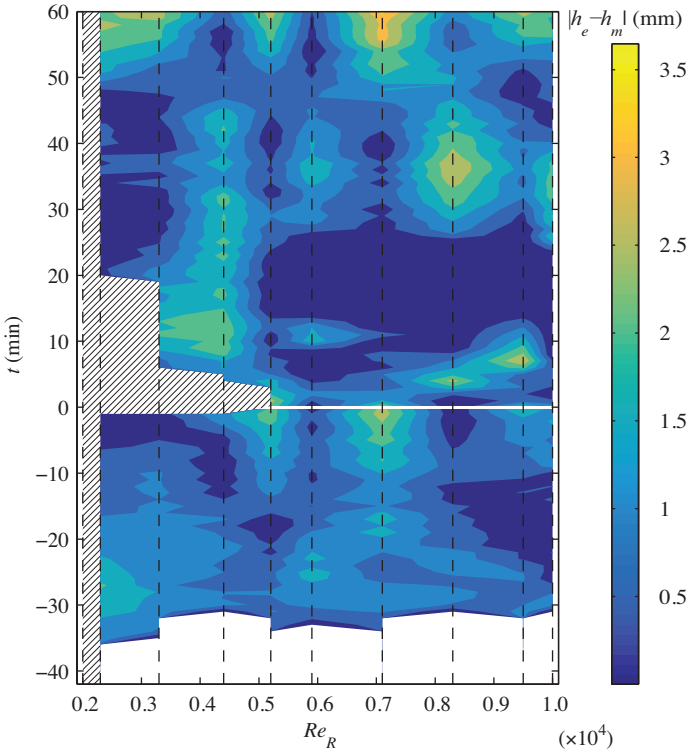

Figure 2.17: Contour plot of absolute difference between h_e and h_m for Experiments 2–10. The distinct Re_R of the experiments are marked by the dashed vertical black lines. Data corresponding to the Re_R of the experiments is linearly interpolated to make the contour plot.

2.6 Discussion

2.6.1 Application to observations under Pine Island Glacier Ice Shelf

Pine Island Glacier Ice Shelf is a 40-km-long, 20-km-wide ice shelf in the Amundsen Sea off West Antarctica. An investigation involving the deployment of autonomous underwater vehicles in its underlying ocean cavity showed that the basal surface of the ice shelf is experiencing rapid melting, probably due to shoaling Circumpolar Deep Water and intrusion of warmer water under the ice (Jenkins *et al.*, 2010*a*).

Stanton *et al.* (2013) reported in-situ measurements of the basal melt rate and ocean boundary layer properties from a site in the center of Pine Island Glacier Ice Shelf where a hole was drilled vertically from the surface to access the water underneath. We use the measurements, which are listed in table 2.4, to test our heat transfer model from (2.15) with $G = G'$. The boundary layer depth and density at the site were obtained from CTD profiling. The departure from freezing, mean current velocity, mean friction velocity, and local melting rate were measured using a flux package installed at an initial distance of 2.3 m below the ice shelf base. The range of values listed for the departure from freezing and mean current velocity are for a 35-day period. The mean friction velocity was constant in that period. The local melt rate is from a fit through measurements from days 5-35 and is equivalent to 14 m per year. We substitute h, u_*, and the medians of the range of values of ρ_ℓ, ΔT_ℓ, and U_∞ from table 2.4, ρ_s, k_s, and L from table 2.2, a typical value of $c_\ell = 4.00 \times 10^3$ Jkg^{-1}K^{-1} for sea water, and a typical value of $\Delta T_s = 19$ K (Tyler *et al.*, 2013) for an Antarctic

Property	In (2.15)	Units	Value
Ice shelf thickness	h	m	460
Boundary layer density	ρ_ℓ	kgm^{-3}	27.22 - 27.42
Departure from freezing	ΔT_ℓ	K	1.35 - 1.42
Mean current velocity	U_∞	ms^{-1}	0.11 - 0.15
Mean friction velocity	u_*	ms^{-1}	0.0086
Local melting rate	$-\mathrm{d}h/\mathrm{d}t$	m per day	0.039

Table 2.4: Measurements of the ocean boundary layer properties from Stanton *et al.* (2013)

ice shelf in (2.15). This yields a predicted melt rate $-\mathrm{d}h/\mathrm{d}t$ of 98 m per year.

The fact that our model over-predicts the observed melt rate can be partly explained by the observed ΔT_ℓ being across a thick stable stratified boundary layer. Our model is not valid for the interaction of a stable stratified layer with an ice-water interface. Eddy diffusivity in a stratified turbulent flow is lower than in an unstratified turbulent flow (Galperin *et al.*, 2007), which can account partly for the discrepancy between the observed and modelled melt rates. Our predicted value of the melt rate at the measurement site is an upper limit and corresponds to the case where a well-mixed turbulent warm water flow comes in direct contact with the ice-water interface.

In this application, phase change due to heat transfer through the boundary layer only is considered. The transfer of salt through the boundary layer is ignored. A mean vertical salt flux of 2.8×10^{-6} psu ms^{-1} was also measured at the observation site by Stanton *et al.* (2013). Both the conservation of heat and the conservation of salt at the interface control the rate of phase change. Whether heat transfer or salt transfer is the more dominant effect in causing the phase change at this site remains an open question. A complete analysis

should consider both effects, and include data from different levels within the boundary layer.

2.6.2 Comparison of γ_T from our model with other expressions for γ_T

The parameterization of the thermal exchange velocity across the boundary layer in our model is

$$\gamma_T = U_\infty C_h = U_\infty \left(\frac{c_f/2}{1 + G'\sqrt{c_f/2}} \right). \tag{2.30}$$

This parameterization is compared against two formulations used in the literature. Jenkins (1991) expressed γ_T as

$$\gamma_T = \frac{C_d^{1/2} U_\infty}{2.12 \ln(C_d^{1/2} Re) + 12.5 Pr^{2/3} - 8.68} \tag{2.31}$$

where C_d is a dimensionless drag coefficient given by

$$C_d = \frac{u_*^2}{U_\infty^2}. \tag{2.32}$$

The expressions (2.30) and (2.31) for γ_T are essentially equivalent, being related by the Prandtl-Nikuradse skin friction law (Kader & Yaglom, 1972). A constant Stanton number C_h is used by Jenkins (2011) for heat transfer through the boundary layer. This is converted to the thermal exchange velocity γ_T using $\gamma_T = U_\infty C_h$. The values of γ_T calculated from (2.30), (2.31), and the constant Stanton number of Jenkins (2011) for the range of friction velocities covered by Experiment 2-10 are compared in figure 2.18. For the configuration where a warm turbulent layer is in direct contact with an ice surface, our experimentally-constrained model estimates that the thermal exchange velocity is larger than conventional models assume.

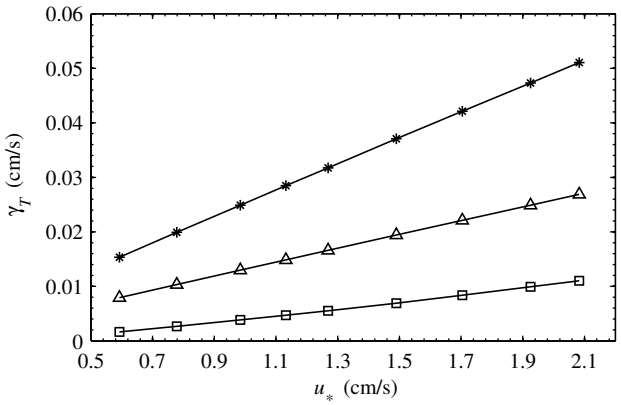

Figure 2.18: Thermal exchange velocity γ_T corresponding to the u_* from our experiments: $*$ from (2.30), $\triangle$ from (2.31) and $\square$ from Jenkins (2011).

2.7 Summary

We have conducted experiments on the melting of ice in a turbulent shear flow that transports warm water to the ice–water interface. A modified heat transfer law, originally derived for turbulent flow over a flat plate and which depends on the friction velocity of the flow, allows us to model the evolution of the ice thickness correctly. Our experiments have dynamic similarity with the geophysical system of the ocean cavity beneath an ice shelf through the Rossby number and thermodynamic similarity through the Stefan number. Although our experiments do not include the effect of salinity, they reveal the mechanisms through which warm water transport to an ice shelf's basal surface accelerates basal melting. Through this study, we propose an experimentally-constrained expression for the thermal exchange velocity γ_T in ice-ocean interaction.

We thank Yuanchao Li and Huang Chen for help in conducting the PIV measurements. We also thank Xiang I. A. Yang for helpful discussion. The

experiments were financially supported by NSF grant EAR-110371.

Chapter 3

Large eddy simulation of heat entrainment under Arctic sea ice

The work presented in this chapter is reproduced from Ramudu *et al.* (2018).

3.1 Introduction

The Arctic sea ice cover has been decreasing over the past few decades (Johannessen *et al.*, 1999; Kwok & Rothrock, 2009; Meier, 2017). This trend can severely affect Earth's climate by causing the Arctic region to continue warming through the positive ice-albedo feedback mechanism as well as by influencing weather and circulation patterns in the mid-latitudes. It can also significantly impact animals, plants, and human activity in and near the Arctic (Notz & Stroeve, 2016). The decline in Arctic sea ice is occurring faster than predicted by global climate models (Stroeve *et al.*, 2007; Kirchmeier-Young *et al.*, 2017), which leads to questions about whether these models are missing some key mechanisms responsible for the melting of sea ice. One such mechanism could be the supply of heat by entrainment from the upper ocean to the ice–ocean interface. In this study, we explore heat entrainment under drifting sea ice during

the summertime in order to better understand this process and its contribution to Arctic sea ice melt.

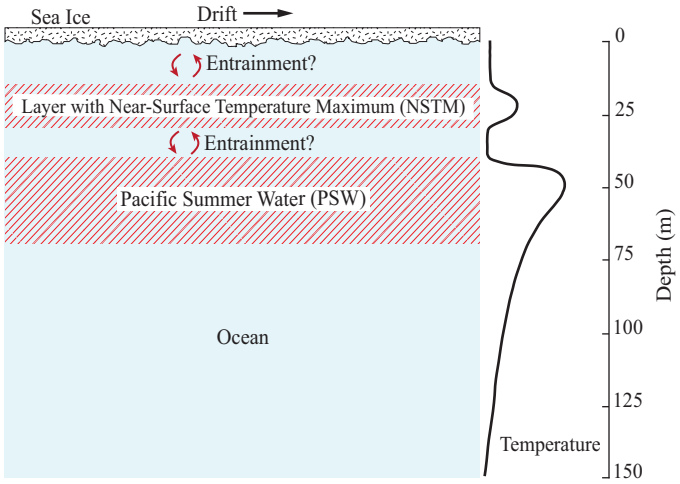

Figure 3.1: Schematic of the typical vertical structure and temperature profile in the Canada Basin in the Arctic Ocean

We focus our study on the Canada Basin in the Arctic Ocean, located roughly between latitudes 72° N and 84° N and longitudes 157° W and 128° W. Among the six regions of the Arctic, the Canada Basin experienced the second largest sea ice thickness decrease rate between 2002 and 2007 (Kwok & Rothrock, 2009). The structure of the upper water column in the Canada Basin is illustrated in figure 3.1. We define the ocean mixed layer as being the layer at the top bounded by a strong density gradient (and hence by a strong salinity gradient, since in the Arctic density is primarily influenced by salinity) below. The mixed layer may be thought of as a layer which experiences mixing at some point during the year, thus being distinguished from a mixing layer which is a layer whose depth corresponds to the depth of active mixing at any

one time. The Canada Basin consists of a shallow mixed layer about 40 m deep. (Toole *et al.*, 2010). Warm water of Pacific origin circulates at the base of the mixed layer (Coachman & Barnes, 1961; Steele *et al.*, 2004) and the heat content of this so-called Pacific Summer Water has been increasing over the years (Woodgate *et al.*, 2006; Timmermans *et al.*, 2014). The mixed layer and PSW layer are separated by a pycnocline that is strongly salinity-stratified (Toole *et al.*, 2010). Within the mixed layer, a Near-Surface Temperature Maximum layer (NSTM) often forms during the summer as a result of solar radiation penetrating through open water areas and getting stored near the surface (McPhee *et al.*, 1998). Given the trend of decreasing sea ice and earlier melt dates in the summer, it is likely that the NSTM will become warmer in time (Jackson *et al.*, 2010).

Several studies have investigated the influences of the heat-containing PSW and NSTM layers on sea ice. Shimada *et al.* (2006) noted that the spatial distribution of the decrease of sea ice concentration corresponds to the spatial distribution of PSW and that the sharper decline in sea ice concentration in the late 1990s coincided with the warming trend of the PSW. Woodgate *et al.* (2010) suggested that the heat flux carried by the flow of PSW into the Arctic initiates the seasonal melting and the formation of open water areas in the sea ice cover. Using observations taken underneath a drifting ice floe in the Beaufort Gyre from the Surface Heat Budget of the Arctic Ocean (SHEBA) project, Shaw *et al.* (2009) estimated the upward heat flux across the pynocline to be 0.1–1.5 W m^{-2} and the ice-ocean heat flux to be about 16.3 W m^{-2} during the summer warming season. Their concurrent numerical modeling indicated a very small heat entrained from the pycnocline, which showed that the heat

for sea ice melting primarily came from solar radiation stored within the mixed layer. On the basis of observations in the Canada Basin in the time period 2004–2009 and of simulation results using a one-dimensional mixed layer, Toole *et al.* (2010) argued that the pycnocline is so stable due to its stratification that PSW heat remains confined underneath the mixed layer. Steele *et al.* (2010) analyzed the summertime heat budget of the surface layer (0–60 m) of the Canada Basin with the Pan-Arctic Ice-Ocean Modeling and Assimilation System (PIOMAS) and found that heat flux from the atmosphere accounts for 77–83% of the warming of the upper ocean while the heat flux from the PSW layer is relatively very small. None of the modeling studies among these prior studies, however, resolved the turbulence explicitly.

In this study, we use large eddy simulation (LES) to investigate the turbulent transport of heat from the PSW and NSTM layers to the basal surface of sea ice as it drifts over the surface of the ocean. Unlike climate models which rely entirely on parameterizations of turbulent diffusion, LES is able to explicitly resolve turbulent fluxes down to the grid scale, with only the subgrid scale (SGS) component requiring parameterization. Considering that the contribution of turbulent heat entrainment to bottom melting of sea ice is currently a key question in Arctic oceanography, we choose to use LES to help improve our understanding of this physical process as LES can capture the details of the turbulent heat fluxes. In turn, this can provide useful insights for developing more accurate parameterizations for climate models. Our LES model is based on a high-fidelity spectral approach on horizontal planes and utilizes a scale-dependent Lagrangian SGS model that dynamically calculates the model coefficients for SGS quantities without *ad hoc* tuning. We remark

that Skyllingstad & Denbo (2001) also used LES, coupled with an ice model, to investigate the ice-ocean boundary layer. While their work focused on the case of wintertime freezing, ours applies to summertime melting. Additionally, we do not couple our LES model with an ice model for reasons explained in §3.2. We do, however, include the impact of sea ice melt on temperature and salinity via the surface boundary conditions.

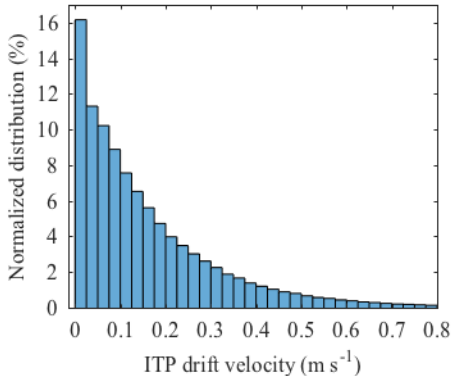

Figure 3.2: Histogram of ice drift velocities of ITPs deployed in the Canada Basin since 2005 (records used are from ITP 1, 2, 3, 4, 5, 6, 8, 11, 13, 18, 21, 23, 32, 33, 34, 41, 42, 43, 52, 55, 69, 77, 78, 79, 80, 82, 84, 85, 86, 87)

Our study isolates the effect of the shear stress-induced turbulence under moving sea ice on heat entrainment from the mixed layer. It can thus show what fraction of observed sea ice melt is due to heat contained in the ocean. To ensure a realistic range of ice drift velocities, we calculated the observed range from the recorded hourly locations of Ice-Tethered Profilers (ITPs) (Toole *et al.*, 2010; Krishfield *et al.*, 2008) deployed in the Canada Basin since 2005 (figure 3.2). Based on these observations, the velocities considered in this study are 0.03–0.30 m s^{-1}.

This paper is organized as follows. Section 3.2 describes in detail the ap-

proach and the set-up of the numerical model. In §3.3, results from simulations investigating the interaction of moving sea ice with the warm PSW and NSTM layers are presented. A case study of the effect of an intense 2012 Arctic cyclone on heat entrainment from the ocean with the LES model is conducted in §3.4. Finally, the results are summarized in §3.5.

3.2 Numerical model

3.2.1 Governing equations

The LES model solves the three-dimensional equations governing the flow under an ice-ocean interface:

$$\frac{\partial \widetilde{u}_i}{\partial t} + \widetilde{u}_j \frac{\partial \widetilde{u}_i}{\partial \widetilde{x}_j} = -\frac{\partial \widetilde{p}}{\partial x_i} + \epsilon_{ij3} f \widetilde{u}_j - \delta_{i3} g \left(1 - \frac{\widetilde{\rho}(\widetilde{\theta}, \widetilde{S})}{\rho_0}\right) - \frac{\partial \tau_{ij}}{\partial x_j} \tag{3.1}$$

$$\frac{\partial \widetilde{u}_i}{\partial x_i} = 0 \tag{3.2}$$

$$\frac{\partial \widetilde{\theta}}{\partial t} + \widetilde{u}_i \frac{\partial \widetilde{\theta}}{\partial x_i} = -\frac{\partial q_{T,i}}{\partial x_i} \tag{3.3}$$

$$\frac{\partial \widetilde{S}}{\partial t} + \widetilde{u}_i \frac{\partial \widetilde{S}}{\partial x_i} = -\frac{\partial q_{S,i}}{\partial x_i}. \tag{3.4}$$

Equation (3.1) is the momentum equation in which the Boussinesq approximation is made, (3.2) is the continuity equation, and (3.3) and (3.4) are the advection-diffusion equations for the scalars potential temperature θ and absolute salinity S respectively. In these equations, the tilde, $\widetilde{(..)}$, refers to a variable filtered on the LES grid and i and j are indices which can take the values 1, 2, and 3 to denote the directions x, y, and z respectively. u_i is the velocity, and u_1 and u_2 will be denoted by u and v respectively; t is time; p is the kinematic pressure; f is the Coriolis parameter; g is the acceleration due to gravity; ρ is the potential density; ρ_0 is a reference density; $\tau_{ij} = \widetilde{u_i u_j} - \widetilde{u}_i \widetilde{u}_j$ is the SGS

stress tensor; $q_{T,i} = \widetilde{u_i\theta} - \widetilde{u}_i\widetilde{\theta}$ is the SGS heat flux; and $q_{S,i} = \widetilde{u_i S} - \widetilde{u}_i\widetilde{S}$ is the SGS salt flux. Equations (3.1)–(3.4) form a coupled system. We use the non-linear equation of state for seawater (TEOS-10) to obtain the potential density $\widetilde{\rho}$ based on the potential temperature $\widetilde{\theta}$ and absolute salinity $\widetilde{S}$ (IOC *et al.*, 2010). Since the Reynolds number of the flow is very high, the effects of molecular viscosity and molecular thermal and salt diffusion are negligible and thus not included in the model. The values and units of all the constants used are listed in table 3.1. The equations are discretized on a Cartesian grid to solve for the velocity components and the evolution of the potential temperature and absolute salinity fields. The dimensions of the domain are $L_x = L_y = 300$ m and $L_z = 150$ m and the corresponding numbers of computational grid points are $N_x = N_y = 128$ and $N_z = 257$. The grid sizes $\Delta_x = L_x/N_x$, $\Delta_y = L_y/N_y$, and $\Delta_z = L_z/(N_z - 1)$ are uniform in each direction.

3.2.2 Numerical implementation

The LES model is based on the work of Albertson & Parlange (1999). It has since been tested and used extensively with application to the atmospheric boundary layer (Porté-Agel, 2004; Kumar *et al.*, 2006; Calaf *et al.*, 2011) and the ocean surface layer (Yang *et al.*, 2014, 2015). In the model, the horizontal components of velocity, the pressure, and the scalar quantities are stored at the cell center. The vertical velocity is stored on a grid staggered in the vertical direction by $\Delta z/2$. Derivatives on the horizontal plane are computed using spectral methods while derivatives on the vertical plane are approximated using second-order finite difference. In the momentum equation, the non-linear term is computed in rotational form to help ensure the conservation of mass and

Table 3.1: Constants used in model

Property	Symbol	Units	Value
Specific heat capacity of ice	c_{ice}	J kg^{-1} K^{-1}	2.10×10^3 [b]
Specific heat capacity of seawater	c_ℓ	J kg^{-1} K^{-1}	4.02×10^3 [a]
Coriolis parameter	f	s^{-1}	1.45×10^{-4}
Acceleration due to gravity	g	m s^{-2}	9.81
Molecular salt diffusivity of seawater	k_S	m^2 s^{-1}	9.0×10^{-10} [b]
Molecular thermal diffusivity of seawater	k_T	m^2 s^{-1}	1.38×10^{-7} [a]
Latent heat of fusion of seawater	L	J kg^{-1}	$L_f(1 - 0.03S_{\text{ice}})$ [d]
Latent heat of fusion of fresh water	L_f	J kg^{-1}	3.35×10^5 [b]
Constant relating freezing temperature to ocean salinity	m	$^{\circ}$C psu^{-1}	0.054 [f]
Typical salinity of sea ice	S_{ice}	g kg^{-1}	3 [c]
Basal roughness length at ITP 77 on 14 June 2014	z_0	m	1.2×10^{-5} [e]
Thermal expansion coefficient of seawater	α	$^{\circ}$C^{-1}	2×10^{-4}
von Karman constant	κ		0.4
Kinematic viscosity of seawater	ν	m^2 s^{-1}	1.84×10^{-6} [a]
Reference density of seawater	ρ_0	kg m^{-3}	1024 [a]
Reference density of sea ice	ρ_{ice}	kg m^{-3}	917 [b]

[a] Sharqawy *et al.* (2010). [b] Kantha & Clayson (2000). [c] IOC *et al.* (2010). [d] McPhee (2008). [e] Cole *et al.* (2017). [f] UNESCO (1981).

kinetic energy (Orszag & Pao, 1975). The momentum equation is solved by the projection method. In this procedure, an intermediate velocity field is first obtained by integrating the momentum equation to an intermediate time step without the pressure gradient term. A Poisson equation for the pressure is then solved using the pipelined Thomas algorithm (Povitsky & Morris, 2000). Finally, the intermediate velocity field is integrated to the new time step with a pressure correction to obtain the new velocity field. Time integration in

the momentum equation and scalar transport equations is performed using the second-order Adams-Bashforth method. In order to avoid aliasing errors, the non-linear terms are de-aliased using the 3/2 rule (Canuto *et al.*, 1988). The model is parallelized using Message Passing Interface (MPI).

3.2.3 SGS model

The expression for the (deviatoric part of the) SGS stress tensor in (3.1) is based on the Smagorinsky model (Smagorinsky, 1963):

$$\tau_{ij} = -2\nu_t \widetilde{\mathcal{S}}_{ij}. \tag{3.5}$$

$\mathcal{S}$ is the strain-rate tensor and ν_t is the eddy viscosity, which is itself given by $\nu_t = (C_s\Delta)^2|\widetilde{\mathcal{S}}|$, where C_s is the Smagorinsky coefficient and $\Delta = (\Delta_x\Delta_y\Delta_z)^{1/3}$ is the cut-off filter size in the LES. C_s is evaluated using the scale-dependent Lagrangian dynamic model of Bou-Zeid *et al.* (2005). Through the use of Lagrangian averaging over fluid pathlines, this method is able to capture the statistically significant spatial and temporal variation in C_s and remain stable at the same time (Meneveau *et al.*, 1996). By being scale-dependent, it is well-suited for LES of inhomogeneous high Reynolds number boundary layer flows where scale-dependence of C_s is expected (Bou-Zeid *et al.*, 2005), as is the case in this study. Furthermore, in this model, C_s is determined directly using resolved quantities, so that there is no need for empirical inputs or *a priori* tuning. The SGS heat flux $q_{T,i}$ and SGS salt flux $q_{S,i}$ are modeled as

$$q_{T,i} = -K_T \frac{\partial \widetilde{\theta}}{\partial x_i} \text{ and} \tag{3.6}$$

$$q_{S,i} = -K_S \frac{\partial \widetilde{S}}{\partial x_i}, \tag{3.7}$$

where K_T is the SGS thermal eddy diffusivity and K_S is the SGS salt eddy diffusivity. They are evaluated as $K_T = \nu_t/\mathrm{Pr}_{\mathrm{SGS}}$ and $K_S = \nu_t/\mathrm{Sc}_{\mathrm{SGS}}$, where $\mathrm{Pr}_{\mathrm{SGS}} = 0.4$ is the turbulent SGS Prandtl number (Antonopoulos-Domis, 1981; Mason, 1989; Yang *et al.*, 2015) and $\mathrm{Sc}_{\mathrm{SGS}} = 0.6$ is the turbulent SGS Schmidt number (Skyllingstad *et al.*, 1999).

3.2.4 Boundary conditions

At the basal ice surface (ice–ocean interface), where $z = 0$, the ocean water moves at a prescribed velocity U_b, the effect of a virtual ice cover over the whole domain drifting at a constant velocity in the x-direction. Hence, U_b is also referred to as the ice velocity. We ignore the vertical motion of the basal ice surface due to melting as well as convergent or divergent ice motions in our simulations. Based on the Monin-Obukhov similarity law, the resulting shear stress τ_{i3} $(i = 1, 2)$ at the top is expressed as

$$\tau_{i3} = -u_*^2 \left[\frac{\widehat{\widetilde{u}}_{r,i}(z_1)}{\sqrt{\widehat{\widetilde{u}}_{r,1}^2(z_1) + \widehat{\widetilde{u}}_{r,2}^2(z_1)}} \right], \tag{3.8}$$

where

$$\widehat{\widetilde{u}}_{r,i}(z_1) = \begin{cases} \widehat{\widetilde{u}}_i(z_1) - U_b, \ i = 1 \\ \widehat{\widetilde{u}}_i(z_1), \ i = 2 \end{cases} \tag{3.9}$$

and u_* is the friction velocity given by

$$u_* = \frac{\sqrt{\widehat{\widetilde{u}}_{r,1}^2(z_1) + \widehat{\widetilde{u}}_{r,2}^2(z_1)}}{(1/\kappa)\ln(z_1/z_0)}. \tag{3.10}$$

$\kappa = 0.4$ is the von Karman constant, $z_1 = \Delta z/2$ is the vertical distance of the first computational grid point, and z_0 is the roughness length of the basal ice surface. The hat, $\widehat{(..)}$, denotes test-filtering of the variables at a scale 2Δ,

which is done to reduce small-scale fluctuations between the local points at which the Monin-Obukhov similarity law is applied such that the large-scale fluctuations have greater influence on the solution (Bou-Zeid *et al.*, 2005). The boundary conditions in the horizontal directions are periodic. At the bottom of the domain, a stress-free condition is imposed. To prevent reflection of gravity waves from the bottom, vertical velocities are damped using a sponge layer (Nieuwstadt *et al.*, 1993).

The boundary conditions for temperature and salinity at the top are derived by considering the heat and salt balances at the virtual ice–ocean interface, following the procedure of Skyllingstad & Denbo (2001). Denoting $q_{T,3}$ and $q_{S,3}$ at $z = 0$ by q_{T*} and q_{S*},

$$\rho_{\text{ice}} L W_b = \rho_0 c_\ell q_{T*} - \rho_{\text{ice}} c_{\text{ice}} q_{\text{ice}} \tag{3.11}$$

$$(S_b - S_{\text{ice}}) W_b = q_{S*}. \tag{3.12}$$

L is the latent heat of fusion sea ice; W_b, the vertical velocity of the ice–ocean interface; c_ℓ, the specific heat capacity of seawater; c_{ice}, the specific heat capacity of sea ice; q_{ice}, the heat flux through the ice; S_b, the salinity of the ocean at the ice–ocean interface; and S_{ice}, the salinity in the interior of sea ice. When ice is melting in the summer, which is the case we consider in this study, $q_{\text{ice}} \ll q_{T*}$ (Shaw *et al.*, 2009), so the second term on the right-hand side of (3.11) can be neglected. The fluxes q_{T*} and q_{S*} are formulated using Monin-Obukhov similarity theory as

$$q_{T*} = \frac{1}{\Phi_T} [\widehat{\widetilde{\theta}}(z_1) - \theta_b] u_* \tag{3.13}$$

$$q_{S*} = \frac{1}{\Phi_T} [\widehat{\widetilde{S}}(z_1) - S_b] u_*, \tag{3.14}$$

where θ_b is the freezing temperature at the ice–ocean interface. We adopt the expressions of McPhee *et al.* (1987*a*) and Skyllingstad & Denbo (2001) for Φ_T and Φ_S in (3.13) and (3.14), respectively:

$$\Phi_T = \frac{1}{\kappa}\ln\left(\frac{z_1}{z_0}\right) + 1.57\left(\frac{u_* z_0}{\nu}\right)^{1/2}\left(\frac{\nu}{k_T}\right)^{2/3} \tag{3.15}$$

$$\Phi_S = \frac{1}{\kappa}\ln\left(\frac{z_1}{z_0}\right) + 1.57\left(\frac{u_* z_0}{\nu}\right)^{1/2}\left(\frac{\nu}{k_S}\right)^{2/3}. \tag{3.16}$$

In the above expressions, ν is the molecular viscosity, k_T is the molecular thermal diffusivity, and k_S is the molecular salt diffusivity of sea water. θ_b and S_b are unknown quantities in (3.13) and (3.14) respectively. The use of $\theta_b = -mS_b$, where $m = 0.054$ °C psu^{-1} (UNESCO, 1981), in (3.13) and the substitution of the resulting expression as well as of (3.14) in (3.11) and (3.12) yield a quadratic equation for S_b:

$$mS_b^2 + \left[\widehat{\widetilde{\theta}}(z_1) - mS_{\text{ice}} + \frac{\Phi_T L}{\Phi_S}\right]S_b - \left[\widehat{\widetilde{\theta}}(z_1)S_{\text{ice}} + \frac{\Phi_T L}{\Phi_S}\widehat{\widetilde{S}}(z_1)\right] = 0. \tag{3.17}$$

This equation is solved for S_b using known quantities pertaining to the flow and the ice. The fluxes q_{T*} and q_{S*} can subsequently be evaluated, with the following steps leading to q_{S*}:

$$W_b = \frac{u_*[\widehat{\widetilde{S}}(z_1) - S_b]}{\Phi_S(S_b - S_{\text{ice}})} \tag{3.18}$$

$$q_{S*} = -W_b[S_{\text{ice}} - \widehat{\widetilde{S}}(z_1)]. \tag{3.19}$$

In all our simulations, $W_b \ll u_*$, which justifies the omission of the vertical motion of the top boundary over the time duration considered in this study, allowing us to simplify the approach by not coupling the LES model with a model for ice evolution. The boundary conditions for the scalars at the bottom

of the domain are small outward temperature and salinity gradients of magnitude similar to the respective gradients inside the domain adjacent to the bottom boundary.

3.2.5 Initial conditions

To set up the initial velocity, we consider a simple model of the oceanic boundary layer near the surface in which the momentum balance is between the Coriolis force and eddy-viscosity forces:

$$-fv = \nu_t \frac{\partial^2 u}{\partial z^2} \tag{3.20}$$

$$fu = \nu_t \frac{\partial^2 v}{\partial z^2}, \tag{3.21}$$

with $u = U_b$ and $v = 0$ at $z = 0$ and $u,\ v \to 0$ as $z \to -\infty$. The solution is

$$u = U_b \exp(z/\delta) \cos(z/\delta) \tag{3.22}$$

$$v = U_b \exp(z/\delta) \sin(z/\delta), \tag{3.23}$$

where $\delta = \sqrt{2\nu_t/f}$. We assume a constant value $\nu_t = 1.0 \times 10^{-3}$ m^2 s^{-1} and initialize our simulations with mean velocity profiles according to (3.22) and (3.23). A small amount of noise is also added. We use vertical profiles of temperature and salinity measured by an ITP in the ocean under sea ice in the Canada Basin for our initial temperature and salinity conditions. The in-situ temperature and practical salinity from the ITP record are converted to potential temperature θ and absolute salinity S respectively using TEOS-10.

3.3 Results

For each initial vertical temperature profile, we perform 10 different LES experiments with ice-drift velocities U_b = 0.03, 0.06, 0.09, 0.12, 0.15, 0.18, 0.21, 0.24, 0.27, and 0.30 m s^{-1}. All the statistics presented in this section are time-averaged between 12 and 14 eddy turnover times, where an eddy turnover time is the ratio of the mixed layer depth z_m to the friction velocity u_*. The domain-averaged kinetic energy (not shown) in all simulations is very close to steady during that interval, with rms fluctuations in a typical simulation approximately 3% of the mean, indicating that quasi-equilibrium has been reached. For the lowest to the largest ice-drift velocity, the twelfth–fourteenth eddy turnover time averaging window corresponds, in physical time, to 129–151, 66–77, 46–53, 35–41, 27–32, 24–27, 21–25, 18–21, 16–18, and 14–17 h. All quantities shown in vertical profiles are horizontally-averaged. Time averaging is denoted by an overbar, $(\bar{..})$, and horizontal averaging is denoted by angle brackets, $(\langle..\rangle)$.

3.3.1 PSW only vs. PSW+NSTM

We investigate heat transfer from the ocean to the basal surface of drifting sea ice for two initial temperature profiles θ_0 in the Canada Basin. They are shown as the black lines in figures 3.3(a) and 3.3(b). The first profile (figure 3.3a) will be referred to as 'PSW only' and is representative of the early summer, having a uniform mixed layer temperature and a temperature peak corresponding to PSW just at the base of the mixed layer. The second profile (figure 3.3b) will be referred to as 'PSW+NSTM' and is typical of the late summer, featuring an NSTM within the mixed layer in addition to the PSW temperature peak just

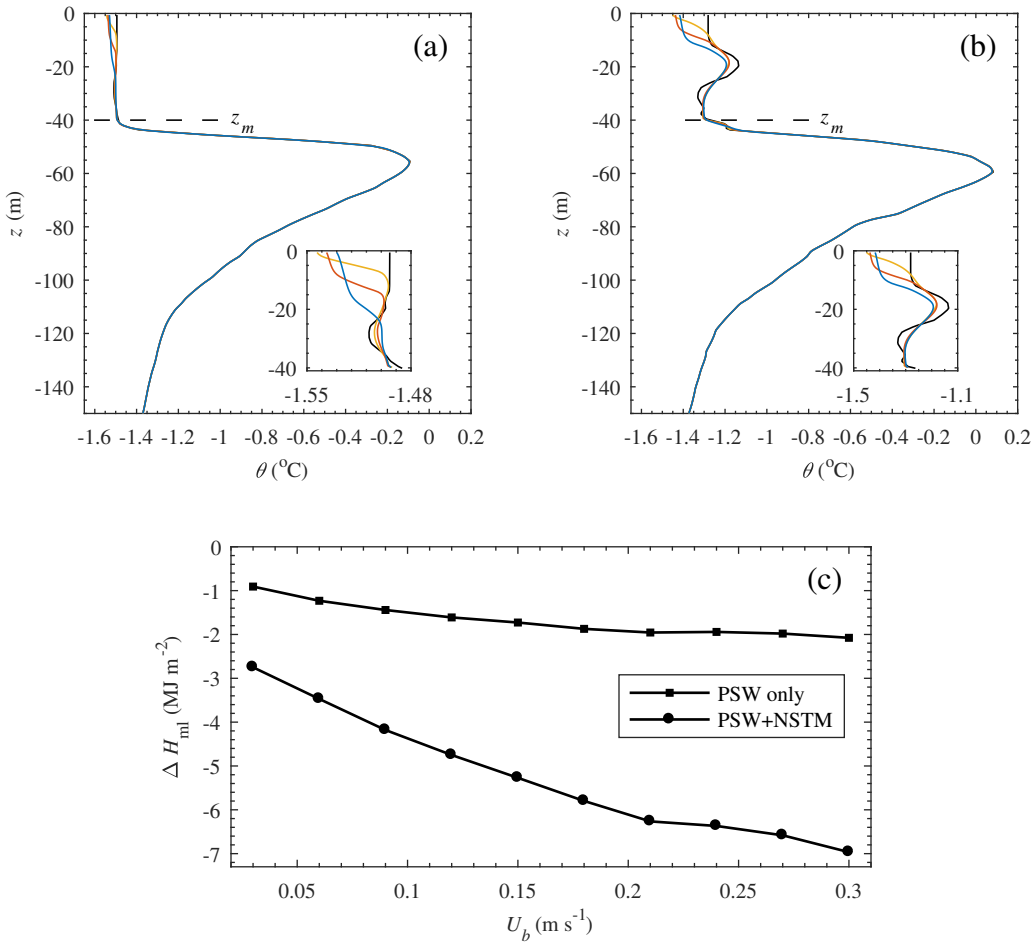

Figure 3.3: Initial temperature θ_0 (solid black line) and final temperature $\langle\overline{\theta}\rangle$ profiles from simulations with $U_b = 0.03$ m s^{-1} (yellow line), 0.15 m s^{-1} (red line), and 0.30 m s^{-1} (blue line) for (a) 'PSW only' case and (b) 'PSW+NSTM' case. The mixed layer depth z_m is indicated by a horizontal dashed line. (c) Change in heat content $\Delta H_{\rm ml}$ of the mixed layer for all U_b.

below the mixed layer. The two profiles were both collected by ITP 77. The 'PSW only' one is from 14 June 2014 at the location 143.0° W and 73.6° N while the 'PSW+NSTM' one is from 14 July 2014 at the location 150.5° W and 74.3° N. The corresponding vertical salinity profiles S_0 are shown in Supporting Information. The initial freezing temperature $\theta_b = -mS_b$ at the basal surface is -1.55 °C in the 'PSW only' case and -1.48 °C in the 'PSW+NSTM' case. The roughness length z_0 (table 3.1) is based on field measurements at the site of ITP 77 on June 14, 2014 (Cole *et al.*, 2017). While z_0 changes when ice melts (Ramudu *et al.*, 2016), the effect of its variation is beyond the scope of this study. The ITP measurements start about 8–12 m underneath the basal ice surface. We extrapolate the temperature and salinity measurement at the first recorded depth level to the basal ice surface in our initial profiles. In both configurations, the mixed layer depth z_m is about 40 m.

In addition to the initial temperature profiles, we present the final temperature profiles $\langle\overline{\theta}\rangle$ from the simulations with the slowest-moving ice ($U_b = 0.03$ m s^{-1}), ice moving at an intermediate velocity ($U_b = 0.15$ m s^{-1}), and the fastest-moving ice ($U_b = 0.30$ m s^{-1}) in figures 3.3(a) and 3.3(b). A thermal boundary layer exists at the ice–ocean interface because the temperature at the interface is at the freezing point θ_b and hence different from the temperature in the mixed layer. The thickness of the thermal boundary layer increases and the temperature difference across it decreases with increasing U_b due to the strength of the shear-driven mixing, which tends to homogenize the layer. These trends are more obvious in figure 3.3(a). In the 'PSW+NSTM' case (figure 3.3b), turbulence from the action of the drifting basal ice surface is responsible for the erosion of the NSTM layer. Heat from the NSTM layer is entrained upwards

and is also mixed downwards, causing the temperature of the water immediately below the NSTM to increase. There is no temperature change in the PSW layer in our experiments.

We calculate the change in heat content of the mixed layer ΔH_{ml} in our simulations according to

$$\Delta H_{\mathrm{ml}} = \int_{z_m}^{0} \rho c_p [\langle \overline{\theta} \rangle (z) - \theta_0(z)] \mathrm{d}z. \tag{3.24}$$

The variation of ΔH_{ml} with U_b is shown in figure 3.3*c*. In the 'PSW+NSTM' case, the mixed layer initially contains more heat than in the 'PSW only' case both because it features an NSTM and because it is at a higher temperature. Over the course of the same integration period, the 'PSW+NSTM' case thus loses more heat than the 'PSW only' case at all U_b due to enhanced turbulent entrainment.

Figure 3.4(*a*) shows the velocity components $\langle \overline{u} \rangle$ and $\langle \overline{v} \rangle$ from our simulations for both the 'PSW only' and 'PSW+NSTM' cases for $U_b = 0.15$ m s^{-1}, an intermediate value in the range of ice-drift velocities we consider. The velocity profiles in the mixed layer represent an Ekman spiral. Cole *et al.* (2014) also reported Ekman veering under sea ice drifting under the action of the wind using ocean velocity observations from the Canada Basin. In the 'PSW only' case, the velocity maxima are located at a greater depth than in the 'PSW+NSTM' case. This occurs because the mixed layer is characterized by a small salt stratification below about 15 m in the presence of the NSTM (see appendix A.4). This salt stratification tends to keep the mixed layer stable, opposing the destabilizing effect of the surface shear stress and thus limiting the depth at which the velocity peaks in the 'PSW+NSTM' case.

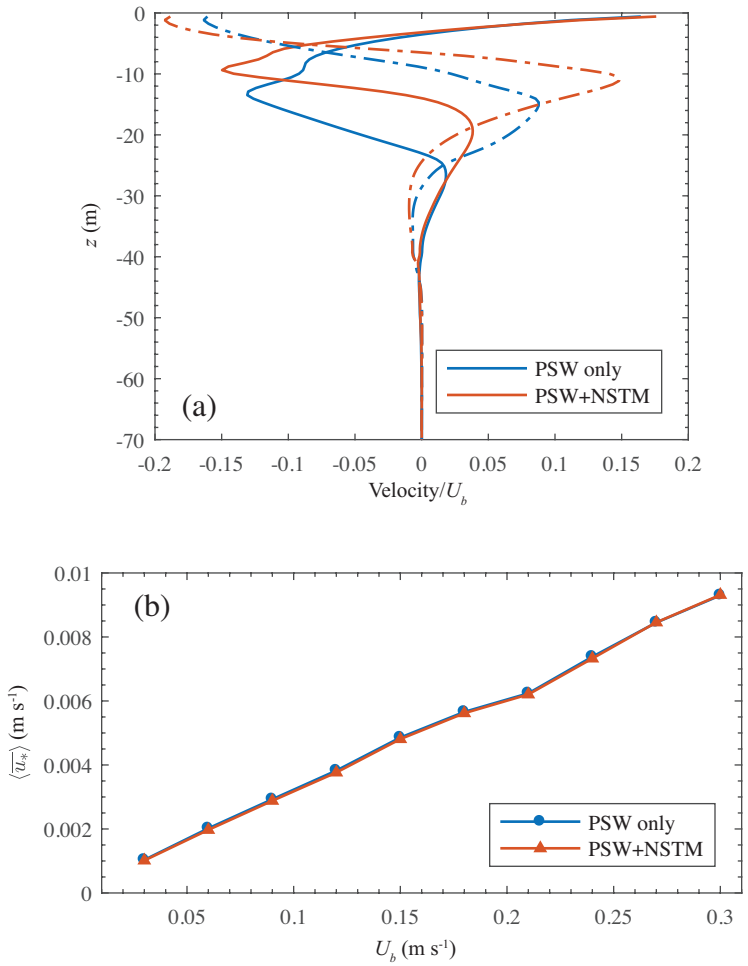

Figure 3.4: (a) Normalized horizontal velocity components $\langle \overline{u} \rangle$ (solid line) and $\langle \overline{v} \rangle$ (dash-dot line) from the simulation with $U_b = 0.15$ m s^{-1}. The points $\langle \overline{u} \rangle / U_b = 1$ and $\langle \overline{v} \rangle / U_b = 0$ at $z = 0$ are omitted. (b) Friction velocity $\langle \overline{u_*} \rangle$ for all U_b.

The friction velocity $\langle\overline{u_*}\rangle$ in all the simulations for both 'PSW only' and 'PSW+NSTM', presented in figure 3.4(b), increases almost linearly with U_b. It is also independent of the vertical temperature or salinity structure in the mixed layer.

We also investigate the spatial fluctuations u' and θ' within the top 40 m for the 'PSW+NSTM' case with $U_b = 0.15$ m s^{-1}. u' and θ' are defined as $u' = \overline{u} - \langle\overline{u}\rangle$ and $\theta' = \overline{\theta} - \langle\overline{\theta}\rangle$. The three-dimensional contour plots of figures 3.5(a) and 3.5(b) indicate that the turbulent field at the surface consists of streaks deflected to the right of the ice drift velocity U_b. The horizontal cross-sections at a depth $z = -4.1$ m are shown in figures 3.5(c) and 3.5(d) and the horizontal cross-sections at a depth $z = -35.2$ m (near the base of the mixed layer) are shown in figures 3.5(e) and 3.5(f). It can be seen that the length scale characterizing the turbulence is smaller at the surface than at the base of the mixed layer. At the surface, the turbulence is caused by the applied shear stress while at the base of the mixed layer, it is caused by internal waves. These two physical processes impose different length scales on the turbulence field. The ability of LES to resolve these different features and length scales makes it a valuable tool to use for this study. There are no major differences in the turbulent length scales between the 'PSW+NSTM' case and 'PSW only' case.

Figures 3.6(a) and 3.6(b) present the resolved heat flux $\rho_0 c_\ell \langle\overline{w'\theta'}\rangle$ (in W m^{-2}) and SGS heat flux $\rho_0 c_\ell \langle\overline{K_T \partial\theta/\partial z}\rangle$ (in W m^{-2}) for the 'PSW only' and 'PSW+NSTM' cases, respectively, for $U_b = 0.03$, 0.15, and 0.30 m s^{-1}. $\overline{w'\theta'}$ is defined as $\overline{w'\theta'} = \overline{w\theta} - \overline{w}\,\overline{\theta}$ and positive values indicate warm water moving upward. These two figures show that at higher ice-drift velocities, the SGS component is smaller than the resolved component, indicating that the LES

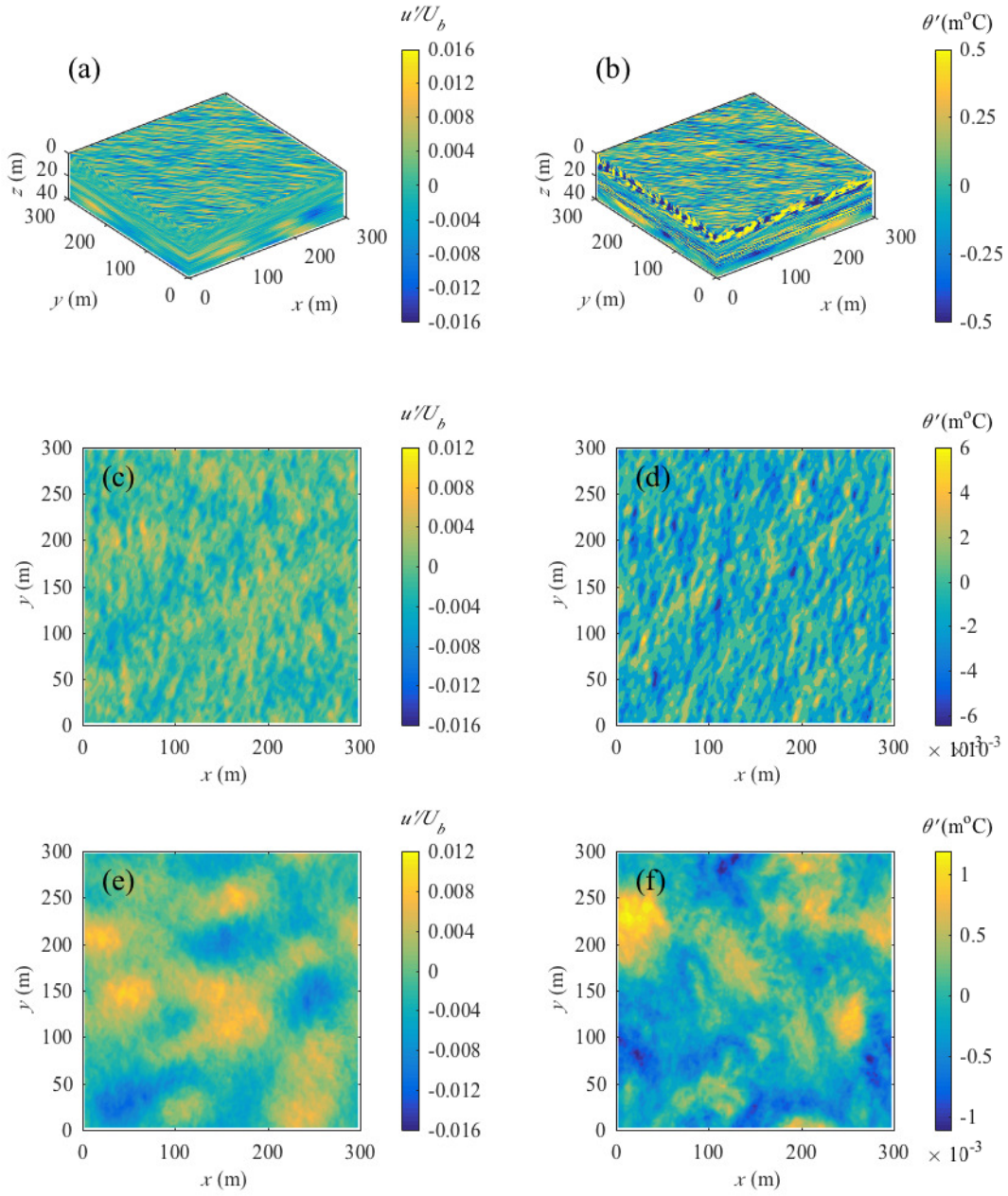

Figure 3.5: Three-dimensional contour plots of (a) u'/U_b and (b) θ'. Horizontal cross-sections at $z = -4.1$ m of (c) u'/U_b and (d) θ'. Horizontal cross-sections at $z = -35.2$ m of (e) u'/U_b and (f) θ'.

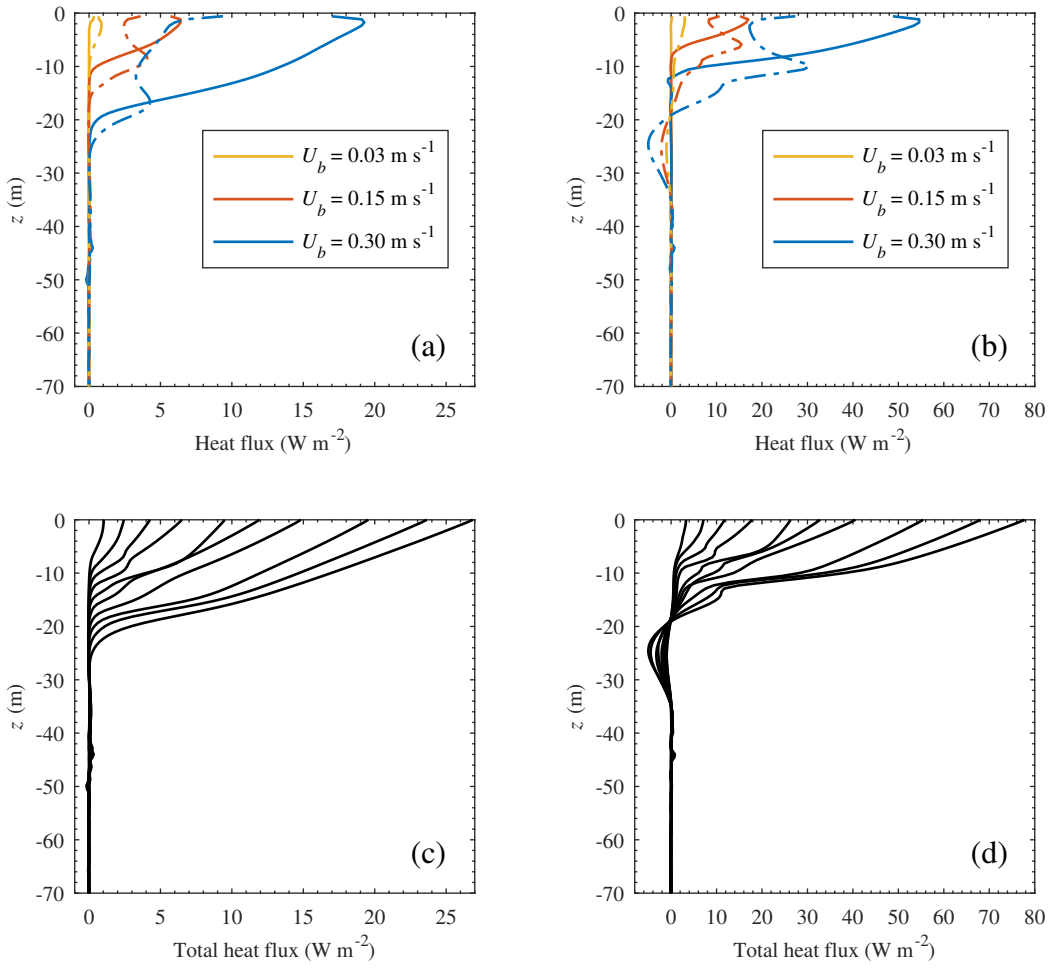

Figure 3.6: Resolved heat flux $\rho_0 c_\ell \langle \overline{w'\theta'} \rangle$ (solid lines) and SGS heat flux $\rho_0 c_\ell \langle \overline{K_T \partial\theta/\partial z} \rangle$ (dash-dotted lines) for the (a) 'PSW only' case and (b) 'PSW+NSTM' case. Total vertical heat flux (resolved+SGS) for the (c) 'PSW only' case and (d) 'PSW+NSTM' case. In (c) and (d), the profiles from left to right correspond to U_b increasing monotonically from 0.03 m s^{-1} to 0.30 m s^{-1}.

can resolve a large fraction of the turbulence. At the lowest U_b, although the shear stress at the surface is small, there is still turbulent convective motion near the ice–ocean interface due to buoyancy differences. This motion is captured by the SGS model to give non-zero eddy thermal diffusivities, which consequently leads to non-zero SGS vertical heat fluxes near the surface. The total vertical heat flux (resolved+SGS) for all U_b is plotted in figures 3.6(c) and 3.6(d) for 'PSW only' and 'PSW+NSTM' respectively. No heat is entrained from the PSW layer even at the largest U_b, so that the temperature of the PSW layer stays unchanged. The output from our simulations therefore support the result of Toole *et al.* (2010), who did not explicitly resolve the turbulent heat flux, that the heat trapped in the PSW layer is shielded from the basal ice surface by the strong salinity stratification at the base of the mixed layer. Heat is entrained only from within the mixed layer as a result of the shear stress-induced turbulence by drifting sea ice. The heat flux $Q_{T*} = \rho_0 c_\ell q_{T*}$ at the basal ice surface increases monotonically with U_b and the presence of the NSTM amplifies the heat entrained to the basal ice surface roughly by a factor of 3. In the 'PSW+NSTM' case, we also note the negative (downward) heat flux at the bottom end of the NSTM layer due to the turbulence mixing heat from the NSTM layer downwards.

The basal ice roughness length $z_0 = 1.2 \times 10^{-5}$ m chosen in this study is on the lower end of the the range of roughness lengths typically observed in the Arctic (Cole *et al.*, 2017). Additional simulations of the 'PSW+NSTM' case (not shown) were run with larger values of z_0 at a fixed $U_b = 0.15$ m s^{-1} for a sensitivity study of how the basal surface heat flux Q_{T*} changes with roughness z_0. It was found that when z_0 increases by 2 orders of magnitude, Q_{T*} increases

by a factor of 2 approximately. Still no heat was entrained from the PSW layer at the largest z_0 considered. Details of this study will be reported in future work.

Gallaher *et al.* (2016) reported measurements of the friction velocity u_* and vertical heat flux collected by the Naval Postgraduate School Autonomous Ocean Flux Buoy (AOFB) 33 (www.oc.nps.edu/∼stanton/fluxbuoy), deployed on the same ice floe as ITP 77. AOFB 33 samples at a depth of 4.5 m or initially 2 m below the basal ice surface. Although the set-up of our LES experiments is idealized, the outputs of friction velocity and total heat flux generally fall within the range of field measurements. The turbulent heat flux is observed to become larger when the NSTM starts developing in the mixed layer, consistent with the results of our simulations.

3.3.2 Modified NSTM

The magnitude of the temperature anomaly of the NSTM that develops within the mixed layer in the Canada Basin is variable. The NSTM evolves over time since it is a seasonal feature and also changes spatially since it depends on incoming solar radiation and the distribution of open water areas. Observations between 2002 and 2007 show that the NSTM is warmest south of 75° N and near the coast but that north of 75° N, the temperature peak of the NSTM has been steadily increasing (Jackson *et al.*, 2010). Some vertical temperature profiles collected by ITPs recently show that the temperature peak corresponding to the NSTM can be as large as the temperature peak corresponding to the PSW layer itself. Gallaher *et al.* (2016) observed that turbulent heat fluxes often exceeded 100 W m^{-2} when the ocean mixed layer heat content, and hence the

size of the NSTM, is large, contributing to well above-average basal ice melt rates. Given the impact of the NSTM on sea ice melt rates, it is important to understand the relationship between the heat content of the NSTM and turbulent heat delivery to the basal surface of sea ice.

To study this relationship, we repeat the LES experiments of §3.3.1 for five new cases, each with a different initial NSTM size (figure 3.7a). The new initial temperature profiles are obtained by artificially modifying the temperature in the NSTM layer, which occupies the depths 11–26 m, in the 'PSW+NSTM' case from §3.3.1. The original 'PSW+NSTM' profile is referred to as 'NSTM 1'. The temperature at all other depths outside the original NSTM layer is unmodified. In 'NSTM 6', the maximum temperature of the NSTM is equal in magnitude to the PSW maximum temperature. The initial heat content of the NSTM layer increases linearly from 'NSTM 1' through 'NSTM 6'.

Simulation results for the heat flux Q_{T*} at the basal ice surface are plotted in figure 3.7(b) for 'NSTM 1' through 'NSTM 6'. For comparison, Q_{T*} for the 'PSW only' case of §3.3.1 is also included. Q_{T*} increases monotonically in magnitude with U_b and the size of the NSTM. We can define a scaling law relating Q_{T*} to U_b and $\Delta\theta$, $\Delta\theta$ being the difference between the initial mean temperature of the mixed layer ($0 \leq z \leq z_m$) and the initial in-situ freezing temperature $\theta_b = -mS_b$ at the surface. The effect of changing the roughness length z_0 is not included in this scaling law. Figure 3.8(a) shows the fit of the dimensionless groups $a(c_\ell \Delta\theta / U_b^2)^{b_1} (U_b/(z_m f))^{b_2}$ to $Q_{T*}/\rho_0 c_\ell U_b \Delta\theta$, where a, b_1, and b_2 are fit coefficients evaluated to be $a = 1.47$, $b_1 = -0.62$, and $b_2 = -0.74$.

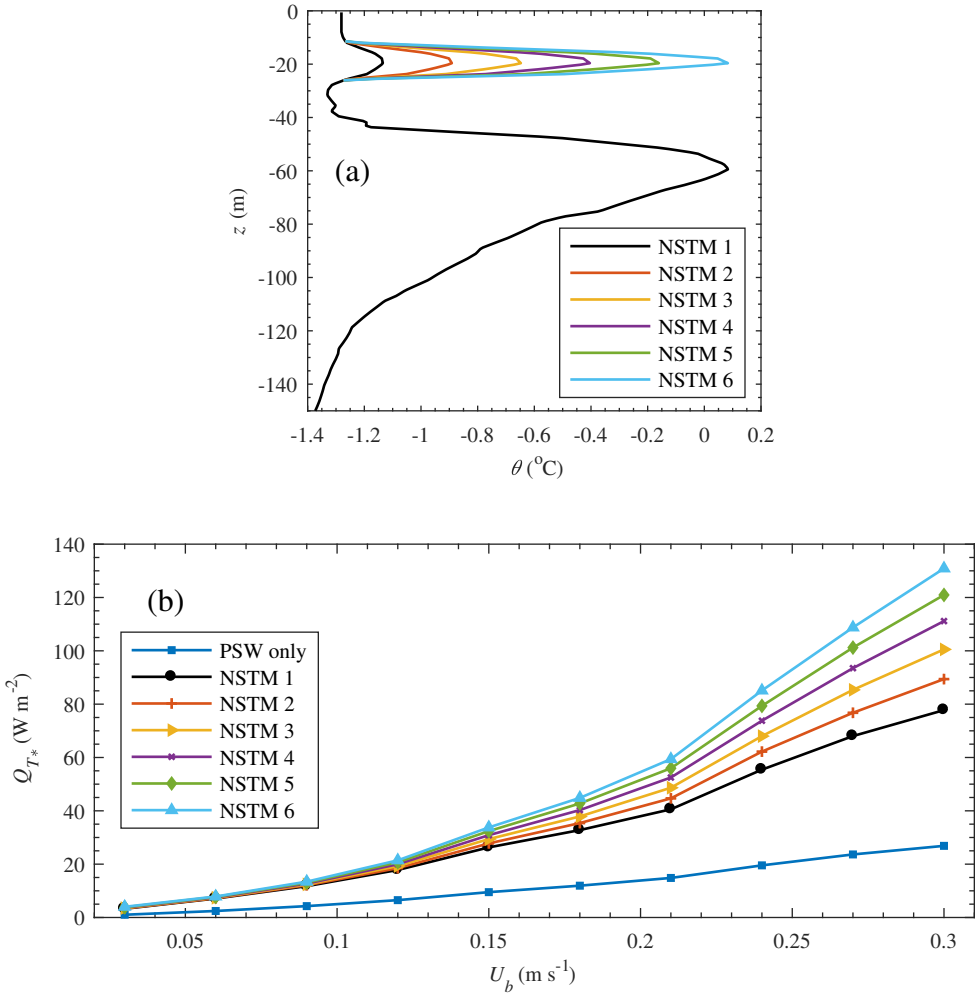

Figure 3.7: (a) Initial temperature profiles for cases 'NSTM 1' through 'NSTM 6'. (b) Basal surface heat flux Q_{T*} for 'NSTM 1' through 'NSTM 6' and all U_b.

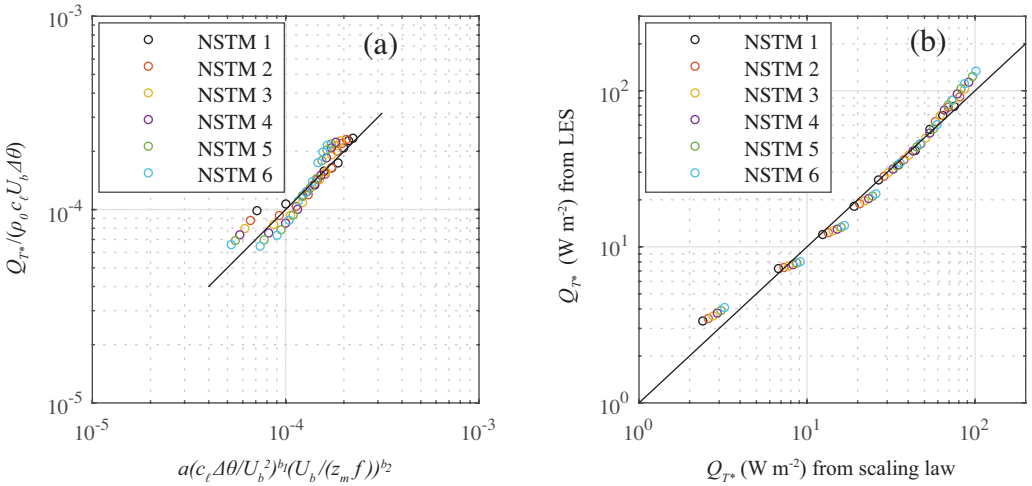

Figure 3.8: (a) Fit of $a(c_\ell \Delta\theta/U_b^2)^{b_1}(U_b/(z_m f))^{b_2}$ to $Q_{T*}/\rho_0 c_\ell U_b \Delta\theta$. (b) Comparison of Q_{T*} from LES with Q_{T*} from (3.25).

We thus propose for Q_{T*} the scaling law

$$Q_{T*} = 1.47 \left(\frac{c_\ell \Delta\theta}{U_b^2}\right)^{-0.62} \left(\frac{U_b}{z_m f}\right)^{-0.74} \rho_0 c_\ell U_b \Delta\theta. \tag{3.25}$$

Q_{T*} varies with $U_b^{1.50}$ and $\Delta\theta^{0.38}$. The dependence on $\Delta\theta$ is sub-linear because melting is a negative feedback process: melting results in the development of stratification at the ice–ocean interface, which suppresses heat delivery to the basal ice surface and hence further melting. The comparison between Q_{T*} from (3.25) and from the LES experiments is presented in a log–log plot in figure 3.8(b), with a black 1:1 line included. While there is good agreement between the two sets of Q_{T*}, the slight departures from the 1:1 line especially at the low and high ends of the range possibly indicate that different physical scales should be used for the scaling law for different ranges of Q_T*.

The 'PSW only' and 'NSTM 1' through 'NSTM 6' profiles are comparable to vertical temperature profiles commonly observed across the Canada Basin.

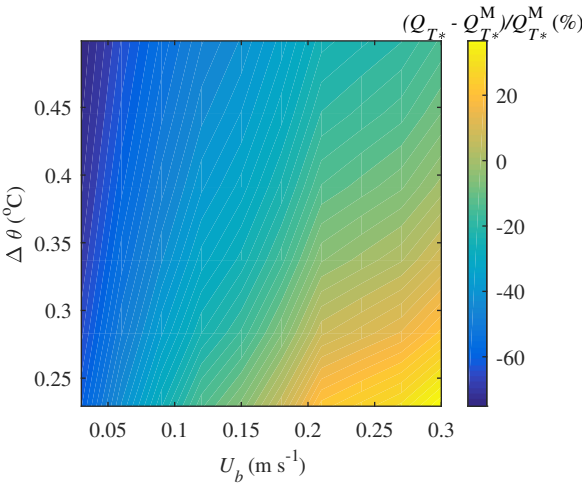

Figure 3.9: Percentage difference between Q_{T*} from (3.28) and Q^{M}_{T*} from (3.26) for $\Delta\theta$ from 'NSTM 1 through NSTM 6' and u_* corresponding to all U_b

There may be differences between actual observations and the profiles considered in our experiments in terms of the depth of the NSTM, depth of the PSW, and stratification strength. Nevertheless, the scaling law in (3.25) can be used to obtain an inexpensive estimate of the heat flux to the basal ice surface due to turbulent entrainment from the mixed layer and its subsequent contribution to basal melting in models of sea ice evolution in the Arctic.

McPhee *et al.* (1999) proposed a simpler expression for the heat flux at the basal ice surface and we will refer to the heat flux from this expression as Q^{M}_{T*}:

$$Q^{\mathrm{M}}_{T*} = c_H \rho_0 c_\ell u_* \Delta\theta. \tag{3.26}$$

$c_H = 0.006$ is a heat transfer coefficient. Our parameterization (3.25) can be rewritten as

$$Q_{T*} = \left(1.47\ c_\ell^{-0.62} z_m^{0.74} f^{0.74}\right) \rho_0 c_\ell U_b^{1.50} \Delta\theta^{0.38} \tag{3.27}$$

and the results shown in figure 3.4(b) suggest the relationship $u_* \approx 0.032\ U_b$ in

our simulations. Substituting this into (3.27) and further simplifying yields

$$Q_{T*} = C\rho_0 c_\ell u_*^{1.50} \Delta\theta^{0.38}, \tag{3.28}$$

with $C = 0.033\ \mathrm{m}^{-0.50}\mathrm{s}^{0.50}\mathrm{K}^{-0.62}$. Figure 3.9 shows the percentage difference between Q_{T*} from (3.28) and Q_{T*}^{M} from (3.26) for $\Delta\theta$ from the profiles 'NSTM 1' through 'NSTM 6' and for u_* corresponding to all U_b. The basal heat fluxes from the two expressions are of the same order. We attribute the differences between them to (3.28) having a super-linear dependence on u_* and sub-linear dependence on $\Delta\theta$.

3.4 Case study: turbulent heat entrainment during 'The Great Arctic Cyclone of 2012'

A large cyclone, commonly referred to as 'The Great Arctic Cyclone of 2012', passed over the Arctic in early August 2012. It lasted almost 13 days and its pressure minimum was the lowest recorded for August cyclones since 1979. Arctic sea ice extent was going to reach a record low after summer 2012, but the passage of the cyclone caused that record low to be reached a few weeks earlier than predicted (Simmonds & Rudeva, 2012).

Zhang *et al.* (2013) used the Pan-arctic Ice-Ocean Modeling and Assimilation System (PIOMAS) to model the effect of the cyclone on the sea ice pack. The cyclone moved over the ice-covered areas of the Pacific sector (ICAPS) of the Arctic on 6–8 August. The ICAPS is defined to be between 90° E and 90° W in the Arctic and covers an area of 3.87×10^6 km^2 based on satellite observations. The rate of sea ice melt in the ICAPS increased to 0.17×10^3 km^3 day^{-1} during the three-day period of 6–8 August from 0.08×10^3 km^3 day^{-1} during the three-

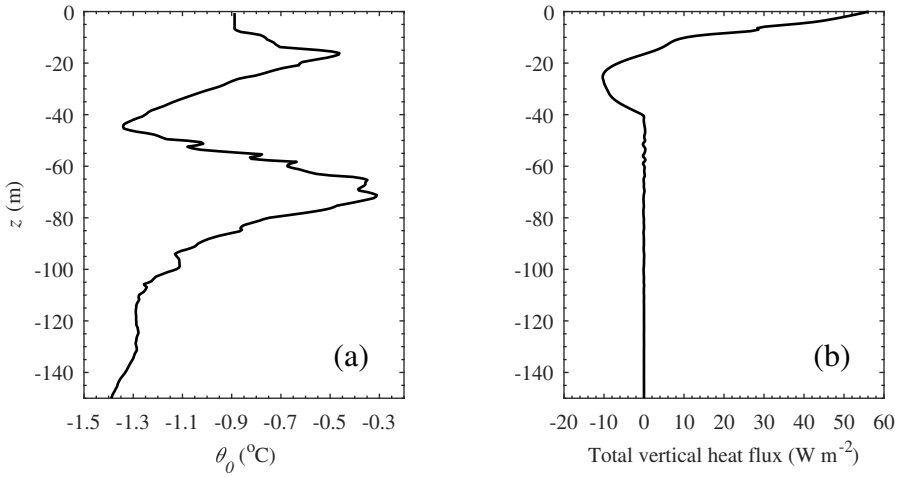

Figure 3.10: (a) Initial temperature profile from ITP 41 on 3 August 2012. (b) Total heat flux from LES.

day period of 2–4 August just before the arrival of the cyclone. Melting at the bottom by ocean dynamic heat transport was the main mechanism contributing to the increase in total melt rate, accounting for 0.10×10^3 km^3 day^{-1} during the cyclone as opposed to only 0.02×10^3 km^3 day^{-1} before. Bottom melt increased because the cyclone caused enhanced heat entrainment from the NSTM. Using (3.11) with the second term on the right neglected, we estimate the average basal ice surface heat flux over the ICAPS responsible for the 0.10×10^3 km^3 day^{-1} of cyclone-associated bottom melting to be 83 W m^{-2}.

A case study of 'The Great Arctic Cyclone of 2012' is conducted using LES. The physical domain size is the same as in previous experiments and all the constants used are the same as in table 3.1. U_b is taken to be 0.18 m s^{-1}, equivalent to the average ice drift speed during the cyclone simulated by Zhang *et al.* (2013). The initial temperature profile, shown in figure 3.10(a), and initial salinity profile, shown in appendix A.4, are from ITP 41 collected on 3 August

2012 at longitude 137.8° W and latitude 74.5° N. The surface heat flux Q_{T*} output by the simulation is 57 W m^{-2} (figure 3.10b). Using a mixed layer depth of 45 m, the scaling law from (3.25) yields $Q_T* = 62$ W m^{-2}. This indicates that the upward heat flux entrained from the heat stored in the ocean by the shear-induced turbulence alone was responsible for roughly 70% of the total ocean-to-ice heat flux during this event.

3.5 Summary

The Arctic Ocean has been losing sea ice due to increased melting since the 1980s, and this decline in sea ice has been particularly pronounced in the Canada Basin. Warm PSW sits at the base of the mixed layer in the Canada Basin and during the summer, the NSTM develops near the surface, storing solar radiation as heat within the mixed layer. It is thought that the presence of the PSW and NSTM water masses has contributed to the observed accelerated melting of sea ice, but the interaction of these two anomalously warm layers with the basal surface of sea ice is not fully known. In order to understand this process better, we use an LES model to study heat transport in a rectangular domain occupying the upper 150 m of the ocean as ice drifts over the surface. LES enables us to resolve the turbulent entrainment of heat not captured explicitly by climate models.

A comparison between the case where the upper ocean features a PSW layer only and the case where it features both the PSW and NSTM layers revealed that in the presence of the NSTM, the heat flux to the basal ice surface is about 3 times larger. Our modeled heat flux near the surface agrees generally well

with field observations. There is almost no heat entrained from the PSW layer over the range of ice-drift velocities considered. This leads to the conclusion that the stratification barrier at the base of the mixed layer is too strong to allow heat from the PSW layer to escape upwards. Since the NSTM itself varies spatially and temporally in the Arctic, we additionally study cases with NSTM sizes larger than in the original case. A scaling law for the basal heat flux is proposed based on the ice-drift velocity and the difference between the initial mean temperature of the mixed layer and the initial freezing temperature at the surface.

Using our LES model, a case study of the effect of 'The Great Arctic Cyclone of 2012' yields a basal surface heat flux of 57 W m^{-2} during the passage of the cyclone. This is compared with the 83 W m^{-2} that we estimated from the PIOMAS-based study of Zhang *et al.* (2013) was responsible for the enhanced bottom melting during the cyclone. The results from our idealized LES set-up indicates that a significant fraction ($\sim$70%) of the total basal heat flux that caused bottom melting was purely due to the action of the drifting ice entraining heat upwards from the mixed layer. In order to simulate this effect, large-scale climate models must be able to account for the NSTM layer. This may require a careful treatment of the optics of the NSTM layer (Kim *et al.*, 2016) in addition to entrainment of heat to the surface. Given the coarse resolution (order of $\sim$10 m vertically) of many climate models, it is far from clear that these processes are currently accurately resolved.

It is thus important to investigate how results from the LES model used in this study compare against results from ocean general circulation models using different mixed layer parameterizations. Furthermore, while almost no heat

entrainment from the PSW was found, the PSW still represents a significant reservoir of heat sitting dangerously close to sea ice in the Arctic. Would a less strongly-stratified pycnocline allow heat entrainment from the PSW more easily? Given the increased melting of sea ice, leads are becoming prominent in the ice cover especially in the summer. What is the impact of leads on ocean-to-ice heat transfer? These questions will be addressed in further research.

The Ice-Tethered Profiler data were collected and made available by the Ice-Tethered Profiler Program (Toole *et al.*, 2010; Krishfield *et al.*, 2008) based at the Woods Hole Oceanographic Institution (http://www.whoi.edu/itp). We thank Thomas Haine and Xiang I. A. Yang for helpful discussion. ER, RG, and AG are financially supported by NOAA grant NA15OAR4310172. DY acknowledges support from his start-up fund at the University of Houston and CM is partially supported by NSF. Supplementary Data is being provided on the Harvard Dataverse repository (Ramudu *et al.*, 2017) to enable the figures to be reproduced and the full data set is available by contacting the corresponding author at gnanades@jhu.edu.

Chapter 4

An optimal roughness length for melting?

4.1 Introduction

The rate of melting of sea ice depends on several factors, including ice velocity, ocean velocity, ocean temperature and stratification, and ice basal surface roughness. The underside of sea ice consists of cracks, blisters, bulges, and pressure ridges (Wadhams, 1988; Wadhams *et al.*, 2006), and thus has a variable topography. Ice basal surface roughness increases from deformation during convergent ice motion or break-up by waves and decreases during refreezing (Martin *et al.*, 2016). It is important to understand the role of surface roughness in the ocean–ice heat transfer process in order to predict the future evolution of sea ice more accurately.

Several studies have investigated turbulent heat transfer across rough surfaces. In Rayleigh-Benard convection, large thermal plumes have been found to be emitted from the gaps between roughness elements, enhancing heat transfer (e.g. Shen *et al.*, 1996). While this is the general view on the effect of surface roughness, Shishkina & Wagner (2011) demonstrated that when the roughness

elements are close to each other, the fluid stagnates, which suppresses heat transfer. In turbulent boundary layer flows over rough walls, increased sweep and ejection events have likewise been observed to contribute to more efficient heat transfer (Shafi *et al.*, 1997). However, similar to Shishkina & Wagner (2011), Hosni *et al.* (1991) noted that below a certain roughness spacing, roughness actually causes a reduction in heat transfer. In the context of ice melting, Gilpin *et al.* (1980) showed experimentally that the development of ripples on an ice surface in turbulent flow leads to an increased heat transfer rate to, and hence an increased melting rate of, the ice surface.

In this chapter, we investigate the effect of varying the surface roughness of sea ice on the ocean–ice turbulent heat flux using large eddy simulation (LES). This study is essentially an extension of the work of Ramudu *et al.* (2018). Surface roughness is usually expressed in terms of a roughness length, z_0. Based on measurements of shear stress, the roughness length under Arctic pack ice was estimated to be 1.0×10^{-3} to 4.7×10^{-2} m (Shaw *et al.*, 2008). Cole *et al.* (2017) estimated the roughness length at the site of an ice-tethered profiler (ITP 77) to vary between 3×10^{-6} to 1×10^{-2} m over the course of April–October 2014. Ramudu *et al.* (2018) used a fixed $z_0 = 1.2 \times 10^{-5}$ m in their analysis, a value at the lower end of the range of typical field values. In this LES investigation, the roughness length z_0 will be varied over two orders of magnitude. z_0 enters as an input variable in the parameterization for the heat flux to the ice–ocean interface in the model we use.

This chapter is organized as follows. In 4.2, we review and summarize the derivation of the heat flux parameterization which we implemented in our LES model. The results from our simulations are presented in 4.3. Finally, we

interpret and discuss our findings in 4.4 and point out important areas for future work.

4.2 Review of the derivation of the expression for q_{T*}

The expression used in chapter 3 for the turbulent heat flux q_T* from the ocean to the ice basal surface is

$$q_{T*} = \frac{1}{\Phi_T}[\theta(z_1) - \theta_b]u_*. \tag{4.1}$$

The symbol θ denotes the water temperature; z, the depth of the first grid point below the ice basal surface which is at $z = 0$; θ_b, the freezing temperature at the ice basal surface; u_*, the friction velocity; and Φ_T, the non-dimensional temperature change between the ice–ocean interface and a depth z.

$$\Phi_T = \Phi_T^{\text{turb}} + \Phi_T^{\text{visc}} \tag{4.2}$$

with Φ_T^{turb} being the temperature change within the logarithmic layer and Φ_T^{visc} being the temperature change within the viscous sublayer near the boundary. We express Φ_T^{turb} as

$$\Phi_T^{\text{turb}} = \frac{1}{\kappa}\log\left(\frac{z}{z_0}\right), \tag{4.3}$$

where $\kappa = 0.4$ is the von Karman constant and z_0 is the roughness length. For Φ_T^{visc}, we use the expression proposed by McPhee *et al.* (1987*a*),

$$\Phi_T^{\text{visc}} = 1.57\left(\frac{u_* z_0}{\nu}\right)^{0.5}\left(\frac{\nu}{k_T}\right)^{0.67}, \tag{4.4}$$

where ν is the molecular viscosity and k_T is the molecular thermal diffusivity. We explore how (4.4) was derived.

McPhee *et al.* (1987*a*) started with a control volume at the ice–ocean interface and made the assumptions that the control volume is at steady state, horizontally homogeneous, and only has negligible conductive and radiative heat transfer through the ice. The heat balance in the control volume is then

$$q_{T*} = W_b L = -K_T \frac{\partial \theta}{\partial z}. \tag{4.5}$$

W_b is the vertical velocity of the ice–ocean interface; L, the latent heat of fusion of sea ice; and K_T, the thermal eddy diffusivity of seawater. Non-dimensionalizing (4.5) and integrating from the ice–ocean interface ($z = z_b$) to a depth z yields

$$\frac{\theta(z) - \theta_b}{W_b L / u_*} = \Phi_T = \int_z^{z_b} \frac{u_*}{K_T} \, \mathrm{d}z'. \tag{4.6}$$

Four models for Φ_T were considered: the first by Josberger (1983) and Ikeda (1986), the second by Mellor *et al.* (1986), the third by Owen & Thomson (1963), and the fourth by Yaglom & Kader (1974). Based on comparisons between observations of ice melt rate and theoretical predictions, the model of Yaglom & Kader (1974), with small modifications, was chosen to ultimately arrive at the expression for Φ_T^{visc} shown in (4.4).

The Yaglom & Kader (1974) model for Φ_T is

$$\Phi_T = \frac{Pr_t}{\kappa} \log\left(\frac{z}{z_0}\right) + \left(\frac{u_* h}{\nu}\right)^{1/2} \left\{ b_1' \left(\frac{\nu}{k_T}\right)^{2/3} - b_2' \right\} + C, \tag{4.7}$$

where Pr_t is the turbulent Prandtl number, h is the size of the average roughness element (wall protrusions), and b_1', b_2', and C are constants. This equation, which was developed originally for turbulent parallel flow along a rough wall, is obtained through the following steps. First, the wall is assumed to have a constant temperature θ_b different from the temperature $\theta(z)$ of the fluid. The

temperature near the wall, above the wall protrusions, can be represented by a general temperature law of the wall,

$$\theta_b - \theta(z) = \theta_* \Phi_T(z_+, Pr, h_+, \sigma_1, \sigma_2, ...). \tag{4.8}$$

In the above expression, θ_* is the friction temperature given by $\theta_* = q_{T*}/(c_\ell \rho_0 u_*)$, where ρ_0 is the reference density and c_ℓ is the specific heat capacity of the fluid. In addition, $z_+ = zu_*/\nu$, $h_+ = hu_*/\nu$, and σ_1 and σ_2 are dimensionless parameters representing the shapes and distribution of the roughness elements. If the Reynolds number and Péclet number of the flow are high enough, the temperature profile will be similar to the turbulent velocity profile near the wall and thus Φ_T will be logarithmic:

$$\Phi_T(z_+, Pr, h_+, \sigma_1, \sigma_2, ...) = \alpha \log z_+ + \beta(Pr, h_+, \sigma_1, \sigma_2). \tag{4.9}$$

α is a numerical coefficient which does not depend on the properties of the wall. Measurements from experiments of turbulent wall flows suggest $\alpha \approx 2.12$. β is a numerical coefficient whose value depends on the roughness of the wall. The mean velocity profile in a turbulent flow along a dynamically rough wall is itself represented by

$$U(z) = u_* \left(\frac{1}{\kappa} \log z_+ + B \right), \tag{4.10}$$

where

$$B = -\frac{1}{\kappa} \log h_+ + B'(\sigma_1, \sigma_2, ...). \tag{4.11}$$

B' is a constant that depends on the shape of the roughness elements. While the velocity profile is not affected by the molecular velocity, the profile of temperature $\theta(z)$ must depend on the molecular thermal diffusivity k_T (or on Pr) since the transfer of heat form the wall to the fluid occurs by molecular diffusion.

Focusing only on cases with $Pr \gtrsim 1$, Yaglom & Kader (1974) proceed by considering the thickness of the viscous sublayer δ_ν near the wall. Since the Reynolds number $Re_{\delta_\nu} = \delta_\nu U(\delta_\nu)/\nu \sim 1$,

$$\delta_\nu \sim \left(\frac{\nu h}{u_*}\right)^{1/2} = h/h_+^{1/2}. \tag{4.12}$$

Within this viscous sublayer, molecular viscosity is the dominant effect in the transfer of momentum.

Concerning the eddy viscosity ν_t and the eddy thermal diffusivity K_T, these decrease as a function of z^3 as $z \to 0$. The following forms for ν_t and K_T are assumed

$$\nu_t = a_M \nu z_+^3 \tag{4.13}$$

$$K_T = a_H \nu z_+^3, \tag{4.14}$$

with a_M and a_H being numerical coefficients. Along a completely rough wall, the turbulent exchange in the spaces between the protrusions would be weaker than the turbulent exchange at the same height along a smooth wall. Thus both a_M and a_H should vary inversely with h_+. Further, ν_t and K_T should be proportional to each other since they represent turbulent exchanges in the same turbulent flow. By taking ν_t and K_T to be of order ν at $z = \delta_\nu$ and by substituting (4.12) in (4.13) and (4.14), the relations

$$a_M \sim h_+^{-3/2} \tag{4.15}$$

$$a_H \sim h_+^{-3/2} \tag{4.16}$$

are obtained. Substituting (4.16) into (4.14) yields

$$K_T = a'_H \nu h_+^{-3/2} z_+^3 \tag{4.17}$$

where a'_H is independent of h_+.

For flows with $Pr \gg 1$, there exists a thin sublayer of thickness δ_m within the viscous sublayer δ_ν in which molecular diffusivity plays a dominant role in heat transfer. Since $K_T = k_T$ at $z = \delta_M$, (4.17) gives

$$a'_H \nu h_+^{-3/2} \left(\frac{\delta_m u_*}{\nu} \right)^3 = k_T, \tag{4.18}$$

which then leads to

$$\delta_m \sim \left(\frac{h}{h_+^{-1/2}} \right) Pr^{-1/3}. \tag{4.19}$$

Eddy diffusivity plays the dominant role in heat transfer at $\delta_m < z < \delta_\nu$. These assumptions about the viscous sublayer lead to the following relationships:

$$-k_T \frac{\mathrm{d}\theta}{\mathrm{d}z} = \frac{q_{T*}}{c_\ell \rho_0}, \ 0 < z < \delta_m \tag{4.20}$$

$$-K_T \frac{\mathrm{d}\theta}{\mathrm{d}z} = \frac{q_{T*}}{c_\ell \rho_0}, \ \delta_m < z < \delta_\nu. \tag{4.21}$$

The above expressions give

$$\theta_b - \theta(\delta_\nu) = \frac{\theta_* h_+^{1/2}}{b'_1 Pr^{2/3} - b'_2}, \tag{4.22}$$

b'_1 and b'_2 being numerical coefficients.

Above the viscous sublayer ($z > \delta_\nu$), the dimensionless temperature $\theta_+(z) = [\theta_b - \theta(z)]/\theta_*$ varies differently from the dimensionless velocity $U_+(y) = U(y)/u_*$ by the factor $\alpha\kappa$. This, along with (4.22), lead to the expression for the term β in (4.9)

$$\beta = h_+^{1/2}(b'_1 Pr^{2/3} - b'_2) - \alpha(\log h_+) + C, \tag{4.23}$$

with C being a numerical coefficient not too different from B' in (4.11).

To estimate the values of the coefficients b'_1, b'_2, and C, Yaglom & Kader (1974) used data from the experiments of Chamberlain (1968). These experiments consisted of measurements of the velocity profile and the concentration

of either the radioactive vapor of ThB or of water vapor in wind tunnels with rough surfaces. With satisfactory accuracy, the values $b_1' = 0.55$, $b_2' = 0.11$, and $C \approx 9.5$ were obtained. The use of these constants in (4.23) and the consequent substitution of (4.23) in (4.9) leads to the full expression for the Yaglom & Kader (1974) model for Φ_T shown in (4.7).

McPhee *et al.* (1987*a*) used (4.7) in a model to theoretically estimate the melt rate at a site during the MIZEX experiment, obtaining predicted values which were lower than observed values. This prompted two adjustments to (4.7). First, since seawater has a large $Pr = 13.8$, the constants b_2' and C are negligible relative to other terms in the expression and can thus be ignored. Second, in order to match the predicted melt rate with the observed melt rate, the coefficient b_1' is changed to 1.57. With these modifications, the expression for Φ_T in (4.7) becomes

$$\Phi_T = \frac{Pr_t}{\kappa} \log\left(\frac{z}{z_0}\right) + 1.57\left(\frac{u_* h}{\nu}\right)^{1/2}\left(\frac{\nu}{k_T}\right)^{2/3}. \tag{4.24}$$

We used the second term on the right of (4.24), which represents the non-dimensional change in temperature across the viscous sublayer, for the expression for Φ_T^{visc} in our model.

4.3 LES results

We investigate the effect of changing the roughness length z_0 on the ocean-to-ice heat flux q_{T*} using LES. The set-up of the LES model is the same as in §3.2 of this thesis. The initial temperature profile from the "PSW+NSTM" case shown in figure 3.3(b) (and corresponding initial salinity profile from figure A.2(b)) are used and an intermediate ice-drift velocity $U_b = 0.15$ m s^{-1} is specified.

Ten simulations are run with roughness lengths $z_0 = 1.2 \times 10^{-3}$, 2.4×10^{-3}, 3.6×10^{-3}, 4.8×10^{-3}, 6.0×10^{-3}, 7.2×10^{-3}, 8.4×10^{-3}, 9.6×10^{-3}, 1.08×10^{-2}, and 1.2×10^{-2} m. For each run, averages are calculated between the 12th and 14th eddy turnover times, when the simulation has reached quasi-equilibrium.

Figure 4.1(a) shows the values of $Q_{T*} = \rho_o c_\ell q_{T*}$, with $\rho_0 = 1024$ kg m^{-3} and $c_\ell = 4.02 \times 10^3$ J kg^{-1} K^{-1}, for varying z_0 from the LES experiments. The Q_{T*} value from the "PSW+NSTM" simulation in §3.3.1 where $z_0 = 1.2 \times 10^{-5}$ is also included. The peak in Q_{T*} corresponds to an optimal roughness length that allows a maximum amount of heat to reach the ice surface to cause melting. Interestingly, it can be seen that the relationship between Q_{T*} and z_0 is non-monotonic. As a sidenote, we present in figure 4.1 (b) the total vertical heat flux (resolved +SGS) from the new LES experiments and from the experiment with $z_0 = 1.2 \times 10^{-5}$ m in chapter 3. We find that even for an ice–ocean interface with higher basal roughness lengths, no PSW heat (which is trapped below the mixed layer based located at $z = -40$ m) is entrained.

4.4 Discussion and Conclusion

The ocean-to-ice heat flux Q_{T*} increases to a peak value and then decreases over the range of z_0 we considered because the two terms on the right-hand side of the expression used for Φ_T,

$$\Phi_T = \frac{1}{\kappa} \log\left(\frac{z}{z_0}\right) + 1.57\left(\frac{u_* z_0}{\nu}\right)^{1/2}\left(\frac{\nu}{k_T}\right)^{2/3}, \tag{4.25}$$

are competing. The first term, representing the non-dimensional temperature change across logarithmic layer, decreases with increasing z_0 whereas the second term, representing the non-dimensional temperature change across the viscous

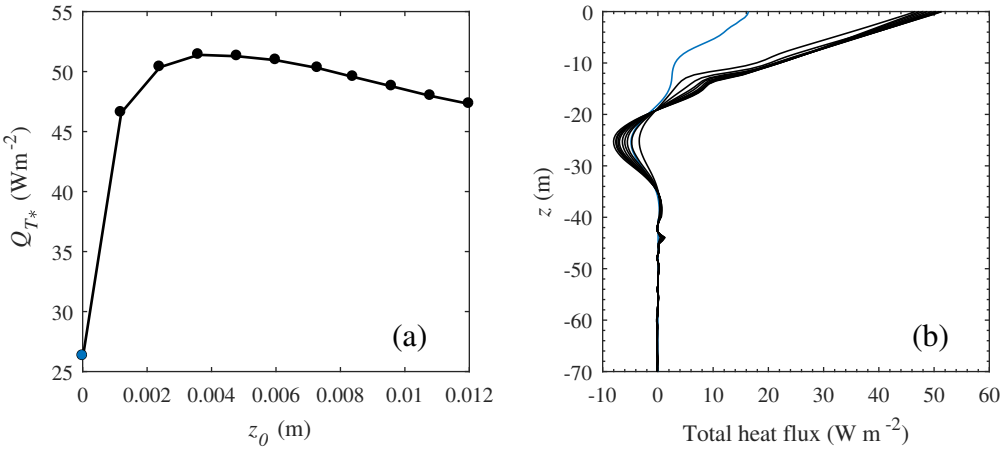

Figure 4.1: (a) Basal surface heat flux Q_{T*} and (b) total vertical heat flux (resolved +SGS) for varying z_0. Results corresponding to $1.2 \times 10^{-}3$ m $\leq z_0 \leq 1.2 \times 10^{-2}$ m are shown in black and results corresponding to $z_0 = 1.2 \times 10^{-5}$ m from chapter 3 are shown in blue.

sublayer, increases with increasing z_0.

While the above argument represents an analytical explanation for the non-monotonic relationship between Q_{T*} and z_0, a physical interpretation is that, as roughness increases above a certain length, turbulent eddies stay further away from the ice–ocean interface, hence delivering less heat to the ice (McPhee *et al.*, 1987*a*). This interpretation is supported by Yaglom & Kader (1974), who remarked that roughness affects heat transfer in two opposite ways. On the one hand, wall roughness causes additional fluctuations in the flow, which enhances heat transfer, but on the other hand, roughness also decelerates the flow at the wall, which leads to a decrease in heat transfer. Comparison of experimental data for flows in pipes of varying roughness indicates that the rate of change of the Nusselt number Nu with Re is larger in rougher pipes than in smoother pipes at low Re. However, as Re increases, the Nu–Re rate of change in rougher

pipes becomes similar to, or sometimes smaller than, the *Nu–Re* rate of change in smoother pipes. Through direct numerical simulations of Rayleigh-Benard convection, Zhang *et al.* (2018) also demonstrated that roughness can cause heat transfer suppression, as Shishkina & Wagner (2011) had earlier noted. Hot/cold fluid can be trapped in the spaces between the roughness elements, setting up a thick thermal boundary layer separating the bulk flow from the boundary.

In light of our LES results for ice basal surface heat flux with varying roughness lengths, we review the parameterizations for the ocean–ice heat flux used in different climate models. These are listed in table 4.1. The symbol θ_{ML} denotes the temperature of the ocean mixed layer, k_{melt}= 240 W m^{-2} K^{-1}, and $c_h = 0.006$. The CICE and LIM parameterizations are from the work of McPhee (1992).

It can be seen that the GFDL CM 2.1 model does not take into account the basal surface roughness. In the LIM and CICE models, a drag coefficient is used in the computation of the friction velocity u_*. The drag coefficient is a constant in LIM while in CICE, it varies non-linearly with z_0. Given the different approaches to treating, or lack of treatment of, surface roughness among climate models, it can be concluded that a clear relationship between sea ice basal roughness and ice–ocean heat flux is required.

In this chapter we reviewed the derivation of a heat transfer law developed by Yaglom & Kader (1974) and modified by McPhee *et al.* (1987*a*). LES experiments based on this heat transfer law showed that the heat flux to the ice basal surface increases to a maximum and then decreases with increasing roughness, indicating that there is an optimal roughness length for melting. This is a non-intuitive trend because it is generally perceived that wall roughness only

Climate model	Parameterization for Q_{T*}	Reference
GFDL CM 2.1	$k_{\mathrm{melt}}(\theta_{\mathrm{ML}} - \theta_b)$	Delworth *et al.* (2006)
LIM	$\rho_0 c_\ell c_h u_*(\theta_{\mathrm{ML}} - \theta_b)$	Vancoppenolle *et al.* (2012)
CICE	$\rho_0 c_\ell c_h u_*(\theta_{\mathrm{ML}} - \theta_b)$	Hunke *et al.* (2015)

Table 4.1: Parameterization of ice–ocean heat flux q_{T*} in different climate models

enhances heat transfer. Roughness, however, may play a complicated role. It is thus important for future work to address the heat flux–surface roughness relationship more deeply in order to improve our understanding of ice–ocean interaction and to make our capabilities for predicting sea ice evolution more robust.

Chapter 5

Future work

Two future studies are proposed based on the work presented in this thesis. The first is a laboratory experiment on ice ablation due to both heat and salt exchange with a turbulent flow and the second is a LES-based numerical investigation of heat entrainment from the ocean to sea ice in a marginal ice zone.

5.1 Turbulent heat and salt exchange between water and ice at an evolving ice–water interface

In the experimental study presented in chapter 2, the effect of salinity on the motion of the ice–water interface was ignored. In the oceanographic situation, the ablation and freezing rates are governed both by the conservation of heat and the conservation of salt at the ice–ocean interface. The freezing point T_f is determined by the salt concentration at the interface. Wells & Worster (2011) showed analytically that when the heat flux from the fluid to the interface is large, melting occurs, but when the far-field fluid tempearture is below T_f, the salt flux to the interface causes ice to dissolve. Ice dissolution by turbulent flow

has been studied experimentally by Kerr & McConnochie (2015).

This proposed future experiment will investigate melting versus dissolution in response to a turbulent flow of a salt solution over an ice–water interface. The apparatus will be similar to the one in the experiment shown in chapter 2, with a set of conductor probes added to measure salinity. Figure 5.1 illustrates the set-up. The ice will melt, dissolve, or grow depending on the initial temperature and salt concentration, the rotation speed of the lid, and on the relative thicknesses, δ_S and δ_T, of the evolving solutal and thermal boundary layers respectively. The regimes corresponding to melting and disssolution in turbulent flow will thus be identified. The ratio of δ_S to δ_T is estimated to be $(\alpha_S/\alpha_T)^{1/2}$, where α_S is the salt diffusivity and α_T is the thermal diffusivity of the solution. This estimation will be verified in this experiment. The proposed study is also an extension of the experiments of Neufeld & Wettlaufer (2008) on the effect of an external flow on mushy layer growth.

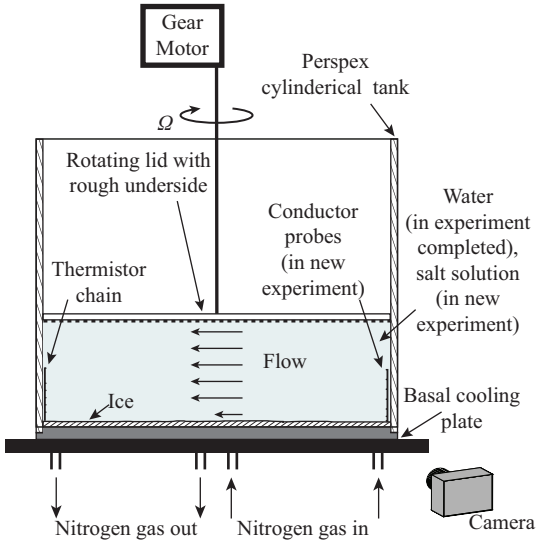

Figure 5.1: Laboratory apparatus including conductor probes

5.2 LES of heat entrainment from the ocean to sea ice in a marginal ice zone

The retreat of Arctic sea ice in the summer causes the formation of a marginal ice zone (MIZ), a region partially ice-covered with the rest being open water. The MIZ is characterized by large spatial gradients in albedo, sea surface temperature, salinity, and wind drag (McPhee *et al.*, 1987*b*). Between 1968 and 2008, the MIZ in the Canada Basin has increased in areal extent, growing by 3.6% per decade (Tivy *et al.*, 2011). Ocean-to-ice heat fluxes as large as 100–200 W m^{-2} and ice bottom melt rates as large as 3–6 cm per day have been measured in that region (Gallaher *et al.*, 2016). In order to improve our sea ice prediction capability, it is important to understand more deeply the absorption and distribution of ocean heat in the MIZ. In this proposed future study, large eddy simulation (LES) will be used to investigate the vertical entrainment of heat from the ocean mixed layer to the ocean surface in the MIZ in the Canada Basin as ice drifts over the surface.

Previous studies focusing on the MIZ have been primarily observational. Gascard *et al.* (1988) reported that the MIZ in Fram Strait is characterized by ice concentration of 10% to 40% and that the ice floes in the MIZ are less than 1 km in diameter. McPhee *et al.* (1987*b*) presented a comprehensive set of measurements of properties at the upper surface of an ice flow and in the turbulent boundary layer under sea ice from a research vessel that drifted from inside the ice edge into the MIZ in the Greenland Sea. Higher melting rates were observed in the MIZ as a consequence of divergence of the ice pack. Wind mixing, the advection of warm water, and buoyancy effects from previous melt-

ing are reported to be three major factors that interplay to set the melting rate. More recently Gallaher *et al.* (2016) studied the ice-ocean boundary layer in the Canada Basin using a set of autonomous measuring instruments over the course of the 2014 summer season. They noted that in the Canada Basin MIZ, the formation of large open water areas is primarily caused by solar radiation input into the ocean, estimating that 86% of solar radiation goes to latent heat losses while the remaining 14% goes to mixed layer heat storage. The studies mentioned above provide important field observations to guide modeling efforts of processes in the MIZ. One modeling study relevant to the MIZ is the work of Skyllingstad & Denbo (2001) in which LES is used to investigate turbulent fluxes under a lead in stationary and moving sea ice in the wintertime. A 150 m-wide lead in an otherwise ice-covered domain was considered, and the LES results demonstrated that salt plumes downstream of the lead increase in length with ice speed. The heat flux near the ice basal surface was also shown to be stronger in the case of moving ice than in stationary ice.

In this proposed project, the efforts of using LES to model the interaction of the PSW and NSTM layers with the basal surface of sea ice in a domain that is fully ice-covered (chapter 3) will be extended to a domain that is only partially ice-covered. The objectives are to understand how turbulent heat entrainment from the ocean mixed layer to sea ice changes with (1) the size of the ice floes, (2) the fraction of the ocean surface covered by ice, (3) the ice drift speed, (4) the size of the NSTM in the mixed layer, and (5) the solar radiative input to the ocean.

As in Skyllingstad & Denbo (2001), the model domain will be held constant and the surface ice field will be moved at a prescribed velocity. The water ve-

locity will be initialized to background noise. In order to have fully-developed turbulence in the boundary layer, the simulations will be spun-up for several hours with a top surface representing full, uniform ice coverage. Open water areas will then be introduced in the top surface. This is representative of simulating the upper ocean under a uniform ice pack at first, with the upper ocean encountering the MIZ eventually.

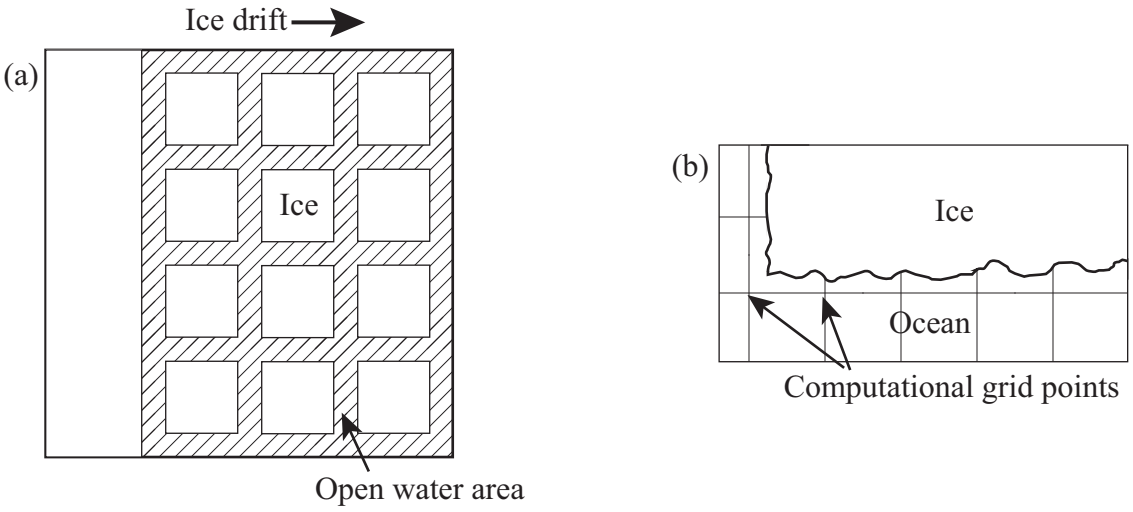

Figure 5.2: (a) Top view of domain showing ice floes partially covering the ocean surface. (b) Cross-section of a control volume at the ice–ocean interface.

The top boundary of the domain will be implemented as shown in figure 5.2a. The top boundary conditions are non-homogeneous, being different at the ice–ocean interface and under the ocean surface. At the ice–ocean interface, the stress resulting from the motion of the ice, the heat flux, and the salt flux will be calculated using Monin-Obukhov similarity theory. In the open water region, a constant stress due to the wind will drive the flow, a heat flux representative of solar radiation penetrating the ocean will be prescribed, and zero salt flux will be imposed. The use of non-homogeneous boundary conditions has not

been tried before in the O LES code *LESGO* and will require significant efforts in development and testing. Initial test-cases will be compared and validated against the simulations of Skyllingstad & Denbo (2001). The effect of surface waves will not be considered in this study. In the Canada Basin, the role of surface waves in causing the ice cover to break up and open water areas to form is minor compared to the effect of radiative input of heat (Gallaher *et al.*, 2016). The rate at which the ice–ocean interface moves due to melting is much lower than the friction velocity driving the turbulence in the mixed layer. The motion of the ice–ocean interface can thus be ignored over the integration periods considered, which makes it justifiable to not have the LES model coupled with an ice model.

An important new method to be introduced in the LES code for this study is the sharp interface immersed boundary method outlined in Mittal *et al.* (2008). Figure 5.2b shows a cross-section of a control volume at the ice–ocean boundary. It can be seen that the bottom surface of the ice can be below the first grid point in the simulations. The flow is thus essentially interacting with a complex solid body. In order to calculate the force that body exerts on the flow, the sharp interface immersed boundary method will be used. This method is based on the calculation of variables on ghost cells inside the body such that the boundary conditions are satisfied precisely on the immersed boundary. The implementation of this method will be a significant component of this project. Extensive testing and validation exercises will be conducted by comparing results against cases from the literature before the procedure is applied to the problem being studied here.

Observations of processes at the ice–ocean interface in a MIZ are difficult

to obtain because of the harsh environmental conditions. The use of a high-resolution LES model, as proposed in this project, can thus contribute significantly to advance our understanding of the MIZ. The results can help quantify the amount of heat entrained from the mixed layer under drifting sea ice that goes to melting compared to the amount that goes to the atmosphere. This will bring insight into whether the tendency is for the ice volume in a certain domain to be minimized or for the heat to simply escape to the atmosphere. Since open water areas are becoming more prominent in the Canada Basin, more solar radiation is penetrating the ocean surface. The effect of heat input through solar radiation on the melting rate can also be quantified in this study. While Gallaher *et al.* (2016) noted that 86% of incoming solar radiation goes to melting, these simulations can show how this percentage changes with different conditions. With increased ice melting, it is expected that the water at the ice–ocean interface becomes increasingly stratified. Simulations will be conducted in this study to show how quickly mixing due to stress at the ice–water interface and at the open ocean surface can break down the stratification to allow more heat delivery to the ice basal surface. Another subject that can be investigated is whether the vertical surface of an ice floe melts faster than the bottom surface. Given that the set-up will be representative of the Canada Basin, the results from this study can show whether heat from the PSW can be brought up to the basal ice surface in a MIZ. The PSW represents a significant reservoir of heat under the mixed layer in the Arctic, and this study can address whether it is responsible for the formation and expansion of the MIZ.

Several scaling laws can be derived from the results. In particular, the dependence of the turbulent heat flux to the basal ice surface on (1) the size

of the ice floes, (2) the open water fraction of the sea surface, (3) the ice drift speed, (4) the size of the NSTM, and (5) the solar radiative input to the ocean can be quantified. These scaling laws can be implemented in regional models of the Arctic Ocean for more accurate prediction of the evolution of sea ice.

Sea ice in the Arctic is projected to further decline in the next decade. The MIZ itself is growing in area and hence becoming increasingly prominent every summer. The significance of this project lies in its potential to reveal many of the small scale interactions and feedbacks at the ice–ocean interface in a MIZ. Understanding these processes will allow us to develop a deeper and more comprehensive picture of how the Arctic is losing its ice.

Appendix A

A.1 Implementation of the scalar transport equation in *LESGO*

The convection-diffusion equation for a tracer C in LES is:

$$\frac{\partial \widetilde{C}}{\partial t} = -\widetilde{u}_i \frac{\partial \widetilde{C}}{\partial x_i} + \frac{\partial}{\partial x_i}\left(K_C \frac{\partial \widetilde{C}}{\partial x_i} \right).$$

K_C is the diffusivity of the tracer, i is an index which represents the directions x, y, and z by taking the values 1, 2, and 3 respectively, u_i is the velocity vector, t is time, and the tilde, $(\widetilde{\cdot})$, denotes filtering at the LES grid scale. The first term on the right hand side is responsible for advection of the tracer while the second term is responsible for tracer diffusion. The discretization of the equation in *LESGO* is described below. k is an index denoting the grid point in the vertical direction and N_z is the total number of vertical grid points.

A.1.1 Advection term

At $k = 1$

$$\left[\widetilde{u}_i \frac{\partial \widetilde{C}}{\partial x_i} \right]_{k=1} = \left[\widetilde{u} \frac{\partial \widetilde{C}}{\partial x} \right]_{k=1} + \left[\widetilde{v} \frac{\partial \widetilde{C}}{\partial y} \right]_{k=1} + \frac{1}{2} \left[\widetilde{w} \frac{\partial \widetilde{C}}{\partial z} \right]_{k=2}$$

For $k = 2$ to $(N_z - 1)$

$$\left[\widetilde{u}_i \frac{\partial \widetilde{C}}{\partial x_i}\right]_k = \left[\widetilde{u}\frac{\partial \widetilde{C}}{\partial x}\right]_k + \left[\widetilde{v}\frac{\partial \widetilde{C}}{\partial y}\right]_k + \frac{1}{2}\left(\left[\widetilde{w}\frac{\partial \widetilde{C}}{\partial z}\right]_k + \left[\widetilde{w}\frac{\partial \widetilde{C}}{\partial z}\right]_{k+1}\right)$$

At $k = N_z$

$$\left[\widetilde{u}_i \frac{\partial \widetilde{C}}{\partial x_i}\right]_{k=N_z} = \left[\widetilde{u}\frac{\partial \widetilde{C}}{\partial x}\right]_{k=N_z} + \left[\widetilde{v}\frac{\partial \widetilde{C}}{\partial y}\right]_{k=N_z}$$

A.1.2 Diffusion term

At $k = 1$

$$\begin{aligned}\left[\frac{\partial}{\partial x_i}\left(K_C \frac{\partial \widetilde{C}}{\partial x_i}\right)\right]_{k=1} &= \frac{\partial}{\partial x}\left(\frac{1}{\chi}\left[\nu_t \frac{\partial \widetilde{C}}{\partial x}\right]_{k=1}\right) \\ &+ \frac{\partial}{\partial y}\left(\frac{1}{\chi}\left[\nu_t \frac{\partial \widetilde{C}}{\partial y}\right]_{k=1}\right) \\ &+ \frac{\partial}{\partial z}\left(\left[\frac{C_b - \widetilde{C}|_{k=1}}{\Phi}\right] u_*\right)\end{aligned}$$

In the above expression, ν_t is the eddy viscosity, $\chi = \nu_t / K_C$, and C_b is the value of the tracer C at the boundary. In addition,

$$u_* = \frac{\sqrt{\widehat{\widetilde{u}}^2|_{k=1} + \widehat{\widetilde{v}}^2|_{k=1}}}{(1/\kappa)\log(z_1/z_0)} \quad \text{and}$$

$$\Phi = \frac{1}{\kappa}\log\left(\frac{z_1}{z_0}\right) + 1.57\left(\frac{u_* z_0}{\nu}\right)^{1/2}\left(\frac{\nu}{k_C}\right)^{2/3},$$

where $\kappa = 0.4$ is the von Karman constant, z_0 is the roughness length, z_1 is the vertical distance of the first grid point from the boundary, k_C is the molecular diffusivity of tracer C, and ν is the molecular viscosity. The hat, $\widehat{(..)}$, denotes test-filtering at twice the grid scale.

For $k = 2$ to $N_z - 1$

$$\left[\frac{\partial}{\partial x_i}\left(K_C \frac{\partial \widetilde{C}}{\partial x_i}\right)\right]_k = \frac{\partial}{\partial x}\left(\frac{1}{\chi}\left[\nu_t|_k + \nu_t|_{k+1}\right]\frac{\partial \widetilde{C}}{\partial x}\bigg|_k\right) + \frac{\partial}{\partial y}\left(\frac{1}{\chi}\left[\nu_t|_k + \nu_t|_{k+1}\right]\frac{\partial \widetilde{C}}{\partial y}\bigg|_k\right) + \frac{\partial}{\partial z}\left(\frac{1}{\chi}\left[\nu_t \frac{\partial \widetilde{C}}{\partial z}\right]_k\right)$$

A.1.3 Time integration

The second-order Adams-Bashforth method is used to integrate the scalar transport equation from timestep n to timestep $(n+1)$. Let

$$\text{RHS} = -\widetilde{u}_i \frac{\partial \widetilde{C}}{\partial x_i} + \frac{\partial}{\partial x_i}\left(K_C \frac{\partial \widetilde{C}}{\partial x_i}\right).$$

Then

$$\widetilde{C}_{n+1} = \widetilde{C}_n + \mathrm{d}t[1.5(\text{RHS}_n) - 0.5(\text{RHS}_{n+1})].$$

A.2 LES model testing and validation

We perform the simulation of McWilliams *et al.* (1997) for shear turbulence in the planetary boundary layer (PBL) of the ocean to test and validate our LES code, in particular its solution for scalars. This simulation includes the effect of temperature but not salinity. While our study of the flow under Arctic sea ice involves both temperature and salinity, it is sufficient to test the code with a case that involves only temperature, because the same advection-diffusion equation is used to solve for the evolution of salinity in our simulations.

We solve (3.1), (3.2), and (3.3) in a three-dimensional rectangular domain with the top corresponding to the ocean surface; ρ in (3.1) is here evaluated using a linear equation of state, $\rho = \rho_0(1-\alpha\theta)$, where $\alpha = 2\times10^{-4}$ °C^{-1} is the thermal expansion coefficient of seawater. A shear stress $\tau = 0.037$ N m^{-2}, equivalent to $u_* = 6.1\times10^{-3}$ m s^{-1} is applied at the top of the domain in the x-direction and a heat flux $q_{T*} = -5$ W m^{-2} leaves the top surface. Although these momentum and heat flux boundary conditions are constants and hence simpler than in our application, they serve our objective of validating our coupled momentum and scalar solver. The effect of the shear stress on the turbulence and the mean flow is much stronger than the effect of surface cooling.

The domain length is $L_x = L_y = 150$ m and $L_z = 90$ m. The domain consists of a mixed layer of depth z_m and a layer stably stratified by temperature underneath. The simulation is set up such that z_m is initially 33 m, with the temperature θ_0 homogeneous from the surface to z_m and decreasing with depth by $\partial\theta_0/\partial z = 0.01$ K m^{-1} below z_m. The computational grid size is $N_x = N_y = 50$ and $N_z = 150$. The simulation is run until it reaches a quasi-equilibrium

state and we take statistics over a length of time during this quasi-equilibrium state. Yang *et al.* (2015) performed a similar LES validation exercise, although they considered the additional effect of Stokes drift giving rise to Langmuir turbulence and reported only statistics related to the velocity field.

Figure A.1 shows the comparison of the horizontally- and time-averaged velocity components $\langle\overline{u}\rangle$ and $\langle\overline{v}\rangle$, total vertical heat flux, and temperature variance $\langle\overline{\theta'^2}\rangle$ from our simulation against those of McWilliams *et al.* (1997). $\overline{\theta'^2}$ is evaluated as $\overline{\theta'^2} = \overline{\theta\theta} - \bar{\theta}\bar{\theta}$. The two sets of profiles of velocity components match each other very closely. The heat flux and temperature profiles agree reasonably well also. We attribute the difference between them to the eddy viscosity model in our simulation being different from that of McWilliams *et al.* (1997). Nieuwstadt *et al.* (1993) showed that different eddy viscosity parameterizations give horizontally-averaged heat flux and temperature variance profiles that are slightly different from each other in their LES of the atmospheric boundary layer.

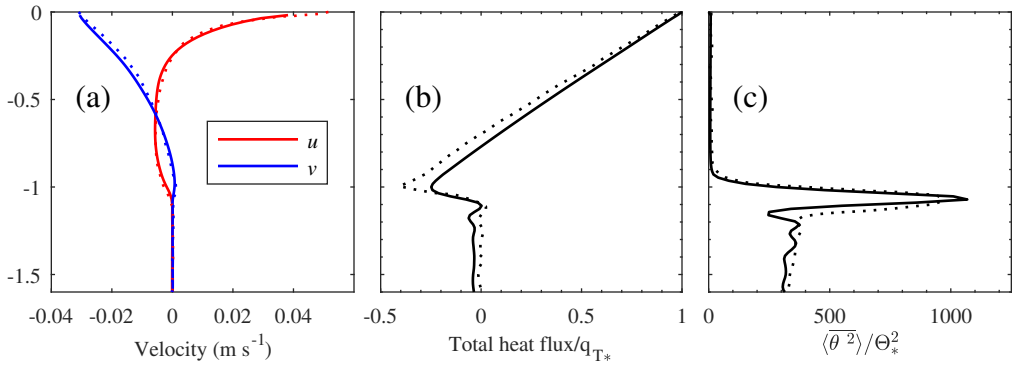

Figure A.1: (a) Velocity components $\langle\overline{u}\rangle$ and $\langle\overline{v}\rangle$, (b) total vertical heat flux $(\langle\overline{w'\theta'}\rangle + \langle\overline{K_T\partial\theta/\partial z}\rangle)$ normalized by q_{T*}, and (c) temperature variance $\langle\overline{\theta'^2}\rangle$ normalized by Θ_*^2, where $\Theta_* = q_{T*}/u_*$. Solid lines: our simulation, dotted lines: McWilliams *et al.* (1997).

A.3 Variable quantities in chapter 3

The list of variable quantities in chapter 3 and the symbols used to denote them is given in table A.1.

Table A.1: Variables used in chapter 3

Quantity	Symbol	Units
Fit coefficients in scaling law	a, b_1, b_2	
Heat transfer coefficient	c_H	
Dimensional constant in heat flux parameterization	C	$\mathrm{m}^{-0.50}\mathrm{s}^{0.50}\mathrm{K}^{-0.62}$
Smagorinsky coefficient	C_s	
Heat content of mixed layer	H_{ml}	J m^{-2}
Indices denoting direction	i, j	
Molecular salt diffusivity	k_S	$\mathrm{m}^2\ \mathrm{s}^{-1}$
Molecular thermal diffusivity	k_T	$\mathrm{m}^2\ \mathrm{s}^{-1}$
Sub-grid scale salt eddy diffusivity	K_S	$\mathrm{m}^2\ \mathrm{s}^{-1}$
Sub-grid scale thermal eddy diffusivity	K_T	$\mathrm{m}^2\ \mathrm{s}^{-1}$
Length of domain	L_x, L_y, L_z	m
Number of computational grid points	N_x, N_y, N_z	
Kinematic pressure	p	$\mathrm{m}^2\ \mathrm{s}^{-2}$
Turbulent subgrid-scale Prandtl number	$\mathrm{Pr}_{\mathrm{SGS}}$	
Heat flux through ice	q_{ice}	K m s^{-1}
Sub-grid scale salt flux	$q_{S,i}$	g kg^{-1} m s^{-1}
Salt flux at ice–ocean interface (at $z = 0$)	q_{S*}	g kg^{-1} m s^{-1}
Sub-grid scale heat flux	$q_{T,i}$	K m s^{-1}
Heat flux at ice–ocean interface (at $z = 0$)	q_{T*}	K m s^{-1}
Heat flux at ice–ocean interface (at $z = 0$)	Q_{T*}	W m^{-2}
Initial salinity	S_0	g kg^{-1}
Salinity of ocean water at ice–ocean interface (at z=0)	S_b	g kg^{-1}
Strain rate	$\mathcal{S}_{i,j}$	s^{-1}
Turbulent subgrid-scale Schmidt number	$\mathrm{Sc}_{\mathrm{SGS}}$	
Time	t	s
Velocity along x and y directions respectively	u, v	m s^{-1}
Friction velocity	u_*	m s^{-1}

Velocity vector	u_i	m s^{-1}
Relative velocity	$u_{r,i}$	m s^{-1}
Velocity of ocean water at ice–ocean interface (at $z = 0$)	U_b	m s^{-1}
Vertical velocity of ice–ocean interface	W_b	m s^{-1}
Displacement vector components	x, y, z	m
Displacement (distance and direction) vector	x_i	m
Vertical distance of first grid point from ice–ocean interface	z_1	m
Mixed layer depth	z_m	m
Ekman layer depth	δ	m
Grid cut-off filter size in LES	Δ	m
Grid size	Δ_x, Δ_y, Δ_z	m
Potential temperature	θ	^{o}C
Initial temperature	θ_0	^{o}C
Freezing temperature at ice–ocean interface (at z=0)	θ_b	^{o}C
Salinity- and pressure-dependent freezing point at a depth z	θ_f	^{o} C
Friction temperature	Θ_*	^{o}C
Molecular viscosity	ν	m^2 s^{-1}
Eddy viscosity	ν_t	m^2 s^{-1}
Potential density	ρ	kg m^{-3}
Sub-grid scale shear stress	$\tau_{i,j}$	m^2 s^{-2}
Parameters in Monin-Obukhov similarity theory	Φ_T, Φ_S	

A.4 Supporting information for chapter 3

As supporting information, we provide figures showing salinity and vertical salt flux profiles that accompany some of the temperature and vertical heat flux profiles, respectively, discussed in chapter 3. The salinity profiles are from ITPs and the vertical salt flux profiles are outputs from the LES experiments.

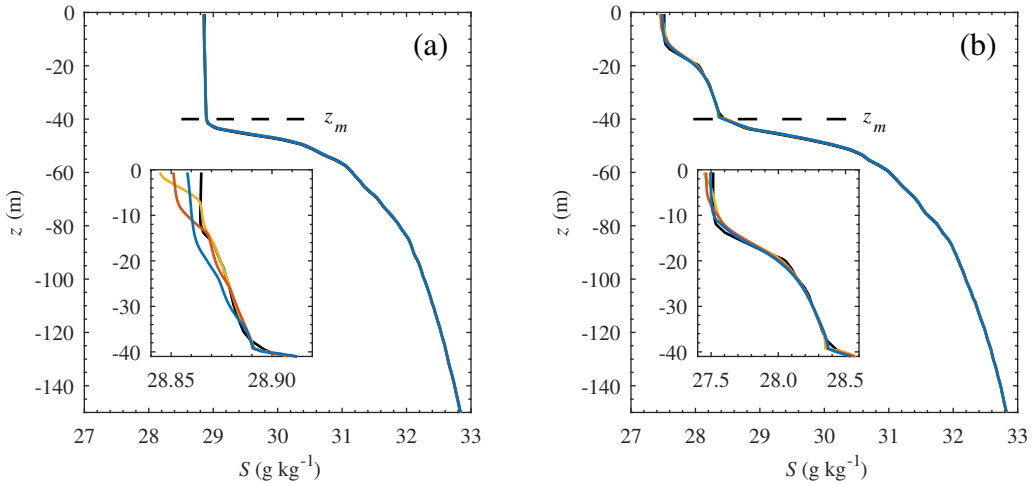

Figure A.2: Initial salinity S_0 (solid black line) and final salinity $\langle\overline{S}\rangle$ profiles from simulations with $U_b = 0.03$ m s^{-1} (yellow line), 0.15 m s^{-1} (red line), and 0.30 m s^{-1} (blue line) for (a) 'PSW only' case and (b) 'PSW+NSTM' case. The mixed layer depth z_m is indicated by a horizontal dashed line.

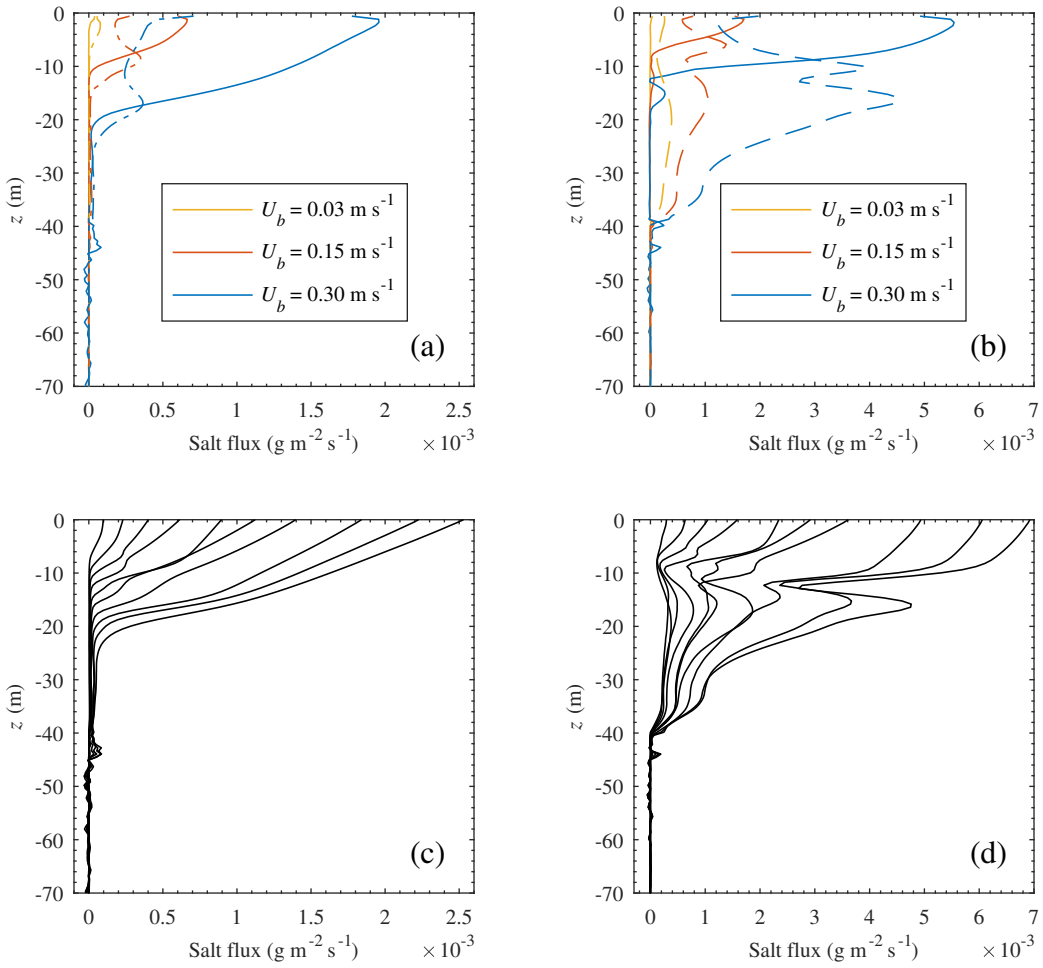

Figure A.3: Resolved salt flux $\rho_0\langle\overline{w'S'}\rangle$ (solid lines) and SGS salt flux $\rho_0\langle\overline{K_S\partial S/\partial z}\rangle$ (dash-dotted lines) for the (a) 'PSW only' case and (b) 'PSW+NSTM' case. Total vertical salt flux (resolved+SGS) for the (c) 'PSW only' case and (d) 'PSW+NSTM' case. In (c) and (d), the profiles from left to right correspond to U_b increasing monotonically from 0.03 m s^{-1} to 0.30 m s^{-1}. This figure is the counterpart of figure 6.

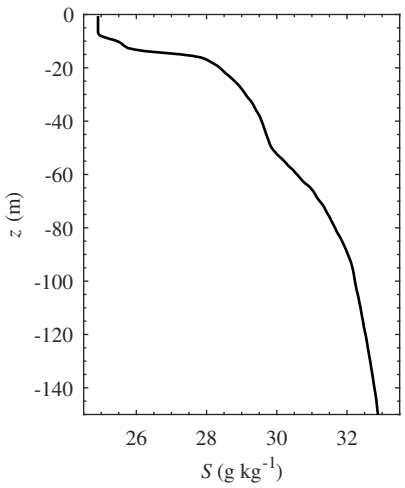

Figure A.4: Initial salinity profile from ITP 41 for case study. This figure is the counterpart of figure 10(a).

Bibliography

Albertson, J. D. & Parlange, M. B. 1999 Surface length scales and shear stress: Implications for land-atmosphere interaction over complex terrain. *Water Resour. Res.* **35** (7), 2121–2132.

AMAP 2012 Arctic Climate Issues 2011: Changes in Arctic snow, water, ice, and permafrost. SWIPA 2011 Overview Report.

Andersson, H. I & Lygren, M. 2006 LES of open rotor–stator flow. *Int. J. Heat Fluid Flow* **27** (4), 551–557.

Antonopoulos-Domis, M. 1981 Large-eddy simulation of a passive scalar in isotropic turbulence. *J. Fluid Mech.* **104**, 55–79.

Boger, D. V. & Westwater, J. W. 1967 Effect of buoyancy on the melting and freezing process. *J. Heat Transfer* **89** (1), 81–89.

Bou-Zeid, E., Meneveau, C. & Parlange, M. 2005 A scale-dependent Lagrangian dynamic model for large eddy simulation of complex turbulent flows. *Phys. Fluids* **17** (2), 025105.

Brisbourne, A. M., Smith, A. M., King, E. C., Nicholls, K. W., Holland, P. R. & Makinson, K. 2014 Seabed topography beneath Larsen C Ice Shelf from seismic soundings. *Cryosphere* **8**, 1–13.

Broecker, W. S., Peacock, S. L., Walker, S., Weiss, R., Fahrbach, E., Schröder, M., Mikolajewicz, U., Heinze, C., Key, R., Peng, T.-H. & Rubin, S. 1998 How much deep water is formed in the Southern Ocean? *J. Geophys. Res.* **103** (C8), 15833–15843.

Bronen, R. 2013 Climate-induced displacement of Alaska native communities. Alaskan Immigration Justice Project. Washington, D.C.: Brookings Institution.

Calaf, M., Parlange, M. B. & Meneveau, C. 2011 Large eddy simulation study of scalar transport in fully developed wind-turbine array boundary layers. *Phys. Fluids* **23** (12), 126603.

Canuto, C., Hussaini, M. Y., Quarteroni, A. & Zang, T. A. 1988 *Spectral Methods in Fluid Dynamics*. New York: Springer-Verlag.

Chamberlain, A. C. 1968 Transport of gases to and from surfaces with bluff and wave-like roughness elements. *Quart. J. Roy. Met. Soc.* **94** (401), 318–332.

Cheah, S. C., Iacovides, H., Jackson, D. C., Ji, H. & Launder, B. E. 1994 Experimental investigation of enclosed rotor-stator disk flows. *Exp. Therm. Fluid Sci.* **9** (4), 445–455.

Coachman, L. K. & Barnes, C. A. 1961 The contribution of Bering Sea water to the Arctic Ocean. *Arctic* **14** (3), 147–161.

Cole, S. T., Timmermans, M-L., Toole, J. M., Krishfield, R. A. & Thwaites, F. T. 2014 Ekman veering, internal waves, and turbulence observed under Arctic sea ice. *J. Phys. Oceanogr.* **44** (5), 1306–1328.

Cole, S. T., Toole, J. M., Lele, R., Timmermans, M-L., Gallaher, S. G., Stanton, T. P., Shaw, W. J., Hwang, B., Maksym, T., Wilkinson, J. P. & others 2017 Ice and ocean velocity in the Arctic marginal ice zone: Ice roughness and momentum transfer. *Elem Sci Anth* **5**.

Comiso, J. C. 2003 Large-scale characteristics and variability of the global sea ice cover. In *Sea ice: An introduction to its Physics, Chemistry, Biology and Geology* (ed. D. N. Thomas & G. S. Dieckmann), chap. 4, pp. 112–142. Oxford, UK: Blackwell Science.

Dallaston, M. C., Hewitt, I. J. & Wells, A. J. 2015 Channelization of plumes beneath ice shelves. *J. Fluid Mech.* **785**, 109–134.

Dansereau, V., Heimbach, P. & Losch, M. 2014 Simulation of subice shelf melt rates in a general circulation model: Velocity-dependent transfer and the role of friction. *J. Geophys. Res. Oceans* **119**, 1765–1790.

Delworth, T. L., Broccoli, A. J., Rosati, A., Stouffer, R. J., Balaji, V., Beesley, J. A., Cooke, W. F., Dixon, K. W., Dunne, J., Dunne, K. A. & others 2006 GFDL's CM2 global coupled climate models. Part I: Formulation and simulation characteristics. *J. Climate* **19** (5), 643–674.

Depoorter, M. A., Bamber, J. L., Griggs, J. A., Lenaerts, J. T. M., Ligtenberg, S. R. M., van den Broeke, M. R. & Moholdt, G.

2013 Calving fluxes and basal melt rates of Antarctic ice shelves. *Nature* **502** (7469), 89.

Dieckmann, G. S. & Hellmer, H. H. 2003 The importance of sea ice: An overview. In *Sea ice: An introduction to its Physics, Chemistry, Biology and Geology* (ed. D. N. Thomas & G. S. Dieckmann), chap. 1, pp. 1–21. Oxford, UK: Blackwell Science.

Drewry, D. J., Jordan, S. R. & Jankowski, E. 1982 Measured properties of the Antarctic ice sheet: surface configuration, ice thickness, volume and bedrock characteristics. *Ann. Glaciol.* **3**, 83–91.

Drewry, D. J. & Morris, E. M. 1992 The response of large ice sheets to climatic change. *Phil. Trans. R. Soc. Lond. B* **338** (1285), 235–242.

Feldmann, J. & Levermann, A. 2015 Collapse of the West Antarctic Ice Sheet after local destabilization of the Amundsen Basin. *Proc. Natl. Acad. Sci. USA* p. 201512482.

Francis, J. A., Chan, W., Leathers, D. J., Miller, J. R. & Veron, D. E. 2009 Winter Northern Hemisphere weather patterns remember summer Arctic sea-ice extent. *Geophys. Res. Lett.* **36** (L07503).

Gallaher, S. G., Stanton, T. P., Shaw, W. J., Cole, S. T., Toole, J. M., Wilkinson, J. P., Maksym, T. & Hwang, B. 2016 Evolution of a Canada Basin ice-ocean boundary layer and mixed layer across a developing thermodynamically forced marginal ice zone. *J. Geophys. Res. Oceans* **121** (8), 6223–6250.

Galperin, B., Sukoriansky, S. & Anderson, P. S. 2007 On the critical Richardson number in stably stratified turbulence. *Atmos. Sci. Lett.* **8** (3), 65–69.

Gascard, J-C., Kergomard, C., Jeannin, P-F. & Fily, M. 1988 Diagnostic study of the Fram Strait Marginal Ice Zone during summer from 1983 and 1984 Marginal Ice Zone Experiment lagrangian observations. *J. Geophys. Res.* **93** (C4), 3613–3641.

Germano, M., Piomelli, U., Moin, P. & Cabot, W. H. 1991 A dynamic subgrid-scale eddy viscosity model. *Phys. Fluids A* **3** (7), 1760–1765.

Gilpin, R.R., Hirata, T. & Cheng, K. C. 1980 Wave formation and heat transfer at an ice-water interface in the presence of a turbulent flow. *J. Fluid Mech.* **99**, 619–640.

Haynes, W. M. 2015 *CRC Handbook of Chemistry and Physics: A Ready-Reference Book of Chemical and Physical Data*. CRC.

Hellmer, H. H. & Olbers, D. J. 1989 A two-dimensional model for the thermohaline circulation under an ice shelf. *Antarc. Sci.* **1** (4), 325–336.

Holland, D. M. & Jenkins, A. 1999 Modeling thermodynamic ice-ocean interactions at the base of an ice shelf. *J. Phys. Oceanogr.* **29** (8), 1787–1800.

Holland, M. M. & Bitz, C. M. 2003 Polar amplification of climate change in coupled models. *Clim. Dyn.* **21**, 221–232.

Holland, P. R. & Feltham, D. L. 2006 The effects of rotation and ice shelf topography on frazil-laden ice shelf water plumes. *J. Phys. Oceanogr.* **36** (12), 2312–2327.

Hooke, R. L. 2005 *Principles of Glacier Mechanics*. Cambridge University Press.

Hosni, M. H., Coleman, H. W. & Taylor, R. P. 1991 Measurements and calculations of rough-wall heat transfer in the turbulent boundary layer. *Int. J. Heat Mass Transfer* **34** (4-5), 1067–1082.

Hunke, E. C., Lipscomb, W. H., Turner, A. K., Jeffery, N. & Elliott, S. 2015 CICE: the Los Alamos sea ice model documentation and software user's manual version 5.1. *Tech. Rep.* LA-CC-06-012. T-3 Fluid Dynamics Group, Los Alamos National Laboratory, Los Alamos, N.M.

Huppert, H. E. & Worster, M. G. 1985 Dynamic solidification of a binary melt. *Nature* **314**, 703–707.

Ikeda, M. 1986 A mixed layer beneath melting sea ice in the marginal ice zone using a one-dimensional turbulent closure model. *J. Geophys. Res.* **91** (C4), 5054–5060.

IOC, SCOR & IAPSO 2010 *The international thermodynamic equation of seawater — 2010: Calculation and use of thermodynamic properties.*. Intergovernmental Oceanographic Commission, Manuals and Guides No. 56, UNESCO (English).

Itoh, M., Yamada, Y., Imao, S. & Gonda, M. 1992 Experiments on turbulent flow due to an enclosed rotating disk. *Exp. Therm. Fluid Sci.* **5** (3), 359–368.

Jackson, J. M., Carmack, E. C., McLaughlin, F. A., Allen, S. E. & Ingram, R. G. 2010 Identification, characterization, and change of the near-surface temperature maximum in the Canada Basin, 1993–2008. *J. Geophys. Res.* **115**, C0521.

Jacobs, S. S., Helmer, H. H., Doake, C. S. M., Jenkins, A. & Frolich, R. M. 1992 Melting of ice shelves and the mass balance of antarctica. *J. Glaciol.* **38** (130), 375–387.

Jacobs, S. S., Jenkins, A., Giulivi, C. F. & Dutrieux, P. 2011 Stronger ocean circulation and increased melting under Pine Island Glacier ice shelf. *Nat. Geosci.* **4**, 519–523.

Jenkins, A. 1991 A one-dimensional model of ice shelf-ocean interaction. *J. Geophys. Res. Oceans* **96** (C11), 20671–20677.

Jenkins, A. 2011 Convection-Driven Melting near the Grounding Lines of Ice Shelves and Tidewater Glaciers. *J. Phys. Oceanogr.* **41** (12), 2279–2294.

Jenkins, A., Dutrieux, P., Jacobs, S. S., McPhail, S. D., Perrett, J. R., Webb, A. T. & White, D. 2010*a* Observations beneath Pine Island Glacier in West Antarctica and implications for its retreat. *Nat. Geosci.* **3**, 468–472.

Jenkins, A., Nicholls, K. W. & Corr, H. F. J. 2010*b* Observation and parameterization of ablation at the base of Ronne Ice Shelf, Antarctica. *J. Phys. Oceanogr.* **40** (10), 2298–2312.

Johannessen, O. M., Shalina, E. V. & Miles, M. W. 1999 Satellite evidence for an Arctic sea ice cover in transformation. *Science* **286** (5446), 1937–1939.

Josberger, E. G. 1983 Sea ice melting in the marginal ice zone. *J. Geophys. Res.* **88** (C5), 2841–2844.

Kader, B. A. & Yaglom, A. M. 1972 Heat and mass transfer laws for fully turbulent wall flows. *Int. J. Heat Mass Transfer* **15**, 2329–2351.

Kantha, L. H. & Clayson, C. A. 2000 *Numerical Models of Oceans and Oceanic Processes*, *Int. Geophys. Ser.*, vol. 66. San Diego, Calif.: Academic Press.

Kerr, R. C. & McConnochie, C. D. 2015 Dissolution of a vertical solid surface by turbulent compositional convection. *J. Fluid Mech.* **765**, 211–228.

Kim, G. E., Gnanadesikan, A. & Pradal, M-A. 2016 Increased surface ocean heating by colored detrital matter (CDM) linked to greater northern hemisphere ice formation in the GFDL CM2Mc ESM. *J. Climate* **29** (24), 9063–9076.

Kirchmeier-Young, M. C., Zwiers, F. W. & Gillett, N. P. 2017 Attribution of extreme events in Arctic sea ice extent. *J. Climate* **30** (2), 553–571.

Krishfield, R., Toole, J., Proshutinsky, A. & Timmermans, M-L. 2008 Automated Ice-Tethered Profilers for seawater observations under pack ice in all seasons. *J. Atmos. Oceanic Technol.* **25** (11), 2091–2105.

Kumar, V., Kleissl, J., Meneveau, C. & Parlange, M. B. 2006 Large-eddy simulation of a diurnal cycle of the atmospheric boundary layer: Atmospheric stability and scaling issues. *Water Resour. Res.* **42** (6), W06D09.

Kwok, R. & Rothrock, D. A. 2009 Decline in Arctic sea ice thickness from submarine and ICESat records: 1958–2008. *Geophys. Res. Lett.* **36** (15), L15501.

Lilly, D. K. 1967 The representation of small scale turbulence in numerical simulation experiments. In *IBM Scientific Computing Symposium on Environmental Sciences* (ed. H. H. Goldstine), pp. 195–210. Yorktown Heights, New York.

Little, C. M., Gnanadesikan, A. & Hallberg, R. 2008 Large-scale oceanographic constraints on the distribution of melting and freezing under ice shelves. *J. Phys. Oceanogr.* **38** (10), 2242–2255.

Liu, J., Curry, J. A., Wang, H., Song, M. & Horton, R. M. 2012 Impact of declining Arctic sea ice on winter snowfall. *Proc. Natl. Acad. Sci. USA* **109** (11), 4074–4079.

Marinov, I., Gnanadesikan, A., Sarmiento, J. L., Toggweiler, J. R., Follows, M. & Mignone, B. K. 2008 Impact of oceanic circulation on biological carbon storage in the ocean and atmospheric pCO2. *Glob. Biogeochem. Cycles* **22**.

Martin, T., Tsamados, M., Schroeder, D. & Feltham, D. L. 2016 The impact of variable sea ice roughness on changes in arctic ocean surface stress: A model study. *J. Geophys. Res. Oceans* **121** (3), 1931–1952.

Martínez Tossas, L. 2017 Large eddy simulations and theoretical analysis of wind turbine aerodynamics using an actuator line model. PhD thesis, The Johns Hopkins University, Baltimore, MD.

Mason, P. J. 1989 Large-eddy simulation of the convective atmospheric boundary layer. *J. Atmos. Sci.* **46** (11), 1492–1516.

McConnochie, C. D. & Kerr, R. C. 2017 Enhanced ablation of a vertical ice wall due to an external freshwater plume. *J. Fluid Mech.* **810**, 429âĂŞ447.

McPhee, M. 2008 *Air-Ice-Ocean Interaction: Turbulent Ocean Boundary Layer Exchange Processes*. Springer.

McPhee, M. G. 1992 Turbulent heat flux in the upper ocean under sea ice. *J. Geophys. Res.* **97** (C4), 5365–5379.

McPhee, M. G., Kottmeier, C. & Morison, J. H. 1999 Ocean heat flux in the Central Weddell Sea during winter. *J. Phys. Oceanogr.* **29** (6), 1166–1179.

McPhee, M. G., Maykut, G. A. & Morison, J. H. 1987*a* Dynamics and thermodynamics of the ice/upper ocean system in the marginal ice zone of the greenland sea. *J. Geophys. Res. Oceans* **92** (C7), 7017–7031.

McPhee, M. G., Maykut, G. A. & Morison, J. H. 1987*b* Dynamics and thermodynamics of the ice/upper ocean system in the Marginal Ice Zone of the Greenland Sea. *J. Geophys. Res. Oceans* **92** (C7), 7017–7031.

McPhee, M. G., Stanton, T. P., Morison, J. H. & Martinson, D. G. 1998 Freshening of the upper ocean in the Arctic: Is perennial sea ice disappearing? *Geophys. Res. Lett.* **25** (10), 1729–1732.

McWilliams, J. C., Sullivan, P. P. & Moeng, C-H. 1997 Langmuir turbulence in the ocean. *J. Fluid Mech.* **334**, 1–30.

Meier, W. N. 2017 Losing Arctic sea ice: observations of the recent decline and the long-term context. In *Sea Ice*, 3rd edn. (ed. David N. Thomas), chap. 11, pp. 290–303. Chichester, UK: John Wiley & Sons.

Mellor, G. L., McPhee, M. G. & Steele, M. 1986 Ice-seawater turbulent boundary layer interaction with melting or freezing. *J. Phys. Oceanogr.* **16** (11), 1829–1846.

Meneveau, C. & Katz, J. 2000 Scale-invariance and turbulence models for large-eddy simulation. *Annu. Rev. Fluid Mech.* **32**, 1–32.

Meneveau, C., Lund, T. S. & Cabot, W. H. 1996 A Lagrangian dynamic subgrid-scale model of turbulence. *J. Fluid Mech.* **319**, 353–385.

Mittal, R., Dong, H., Bozkurttas, M., Najjar, F. M., Vargas, A. & von Loebbecke, A. 2008 A versatile sharp interface immersed boundary method for incompressible flows with complex boundaries. *J. Comput. Phys.* **227** (10), 4825–4852.

Moeng, C-H. & Sullivan, Peter P. P. 2015 Large-eddy simulation. In *Encyclopedia of Atmospheric Sciences*, 2nd edn. (ed. G.R. North (editor-in chief), J. Pyle & F. Zhang), , vol. 4, pp. 232–240. Academic Press.

Mueller, R. D., Padman, L., Dinniman, M. S., Erofeeva, S. Y., Fricker, H. A. & King, M. A. 2012 Impact of tide-topography interactions on basal melting of Larsen C Ice Shelf, Antarctica. *J. Geophys. Res. Oceans* **117** (C5).

Neufeld, J. A. & Wettlaufer, J. S. 2008 An experimental study of shear-enhanced convection in a mushy layer. *J. Fluid Mech.* **612**, 363–385.

Nieuwstadt, F. T. M., Mason, P. J., Moeng, C-H. & Schumann, U. 1993 Large-eddy simulation of the convective boundary layer: A comparison of four computer codes. In *Turbulent Shear Flows 8: Selected Papers from the Eighth International Symposium on Turbulent Shear Flows* (ed. Franz Durst, Rainer Friedrich, Brian E. Launder, Frank W. Schmidt, Ulrich Schumann & James H. Whitelaw), pp. 343–367. Berlin: Springer-Verlag.

Notz, D. & Stroeve, J. 2016 Observed Arctic sea-ice loss directly follows anthropogenic CO_2 emission. *Science* **354** (6313), 747–750.

Orszag, S. A. & Pao, Y-H. 1975 Numerical computation of turbulent shear flows. In *Advances in Geophysics: Turbulent Diffusion in Environmental Pollution, Proceedings of a Symposium held at Charlottesville, Virginia* (ed. F. N. Frenkiel & R. E. Munn), *A*, vol. 18, pp. 225–236. Elsevier.

Owen, P. R. & Thomson, W. R. 1963 Heat transfer across rough surfaces. *J. Fluid Mech* **15** (3), 321–334.

Paolo, F. S., Fricker, H. A. & Padman, L. 2015 Volume loss from Antarctic ice shelves is accelerating. *Science* **348** (6232), 327–331.

Perovich, D. K., Light, B., Eicken, H., Jones, K. F., Runciman, K. & Nghiem, S. V. 2007 Increasing solar heating of the Arctic Ocean and adjacent seas, 1979–2005: Attribution and role in the ice-albedo feedback. *Geophys. Res. Lett.* **34** (19).

Piomelli, U. 1999 Large-eddy simulation: achievements and challenges. *Prog. Aerosp. Sci.* **35** (4), 335–362.

Pope, S. B. 2000 *Turbulent Flows*. Cambridge University Press.

Porté-Agel, F. 2004 A scale-dependent dynamic model for scalar transport in large-eddy simulations of the atmospheric boundary layer. *Boundary-Layer Meteorol.* **112**, 81–105.

Post, E., Bhatt, U. S., Bitz, C. M., Brodie, J. F., Fulton, T. L., Hebblewhite, M., Kerby, J., Kutz, S. J., Stirling, I. & Walker, D. A. 2013 Ecological consequences of sea-ice decline. *Science* **341** (6145), 519–524.

Povitsky, A. & Morris, P. J. 2000 A higher-order compact method in space and time based on parallel implementation of the Thomas algorithm. *J. Comput. Phys.* **161**, 182–203.

Pritchard, H. D., Ligtenberg, S. R. M., Fricker, H. A., Vaughan, D. G., Van den Broeke, M. R. & Padman, L. 2012 Antarctic ice-sheet loss driven by basal melting of ice shelves. *Nature* **484**, 502–505.

Ramudu, E., Gelderloos, R., Yang, D., Meneveau, C. & Gnanadesikan, A. 2017 Replication data for: Large eddy simulation of heat entrainment under arctic sea ice.

Ramudu, E., Gelderloos, R., Yang, D., Meneveau, C. & Gnanadesikan, A. 2018 Large eddy simulation of heat entrainment under arctic sea ice. *J. Geophys. Res. Oceans* **123**, 287–304.

Ramudu, E., Hirsh, B. H., Olson, P. & Gnanadesikan, A. 2016 Turbulent heat exchange between water and ice at an evolving ice–water interface. *J. Fluid Mech.* **798**, 572–597.

Rignot, E., Jacobs, S., Mouginot, J. & Scheuchl, B. 2013 Ice-Shelf melting around Antarctica. *Science* **341** (6143), 266–270.

Scheduikat, M. & Olbers, D. J. 1990 A one-dimensional mixed layer model beneath the Ross Ice Shelf with tidally induced vertical mixing. *Antarc. Sci.* **2** (1), 29–42.

Schmidtko, S., Heywood, K. J., Thompson, A. F. & Aoki, S. 2014 Multidecadal warming of Antarctic waters. *Science* **346**, 1227–1231.

Serreze, M. C., Barrett, A. P. & Cassano, J. J. 2011 Circulation and surface controls on the lower tropospheric air temperature field of the Arctic. *J. Geophys. Res.* **116** (D07104).

Serreze, M. C., Barrett, A. P., Stroeve, J. C., Kindig, D. N. & Holland, M. M. 2009 The emergence of surface-based Arctic amplification. *Cryosphere* **3**, 11.

Serreze, M. C., Holland, M. M. & Stroeve, J. 2007 Perspectives on the Arctic's shrinking sea-ice cover. *Science* **315** (5818), 1533–1536.

Shafi, H. S., Antonia, R. A. & Krogstad, P-Å 1997 Heat flux measurements in a turbulent boundary layer on a rough wall. *Int. J. Heat Mass Transfer* **40** (12), 2989–2993.

Sharqawy, M. H., Lienhard, J. H. & Zubair, S. M. 2010 Thermophysical properties of seawater: A review of existing correlations and data. *Desalination and Water Treatment* **16** (1–3), 354–380.

Shaw, W. J., Stanton, T. P., McPhee, M. G. & Kikuchi, T. 2008 Estimates of surface roughness length in heterogeneous under-ice boundary layers. *J. Geophys. Res. Oceans* **113** (C8).

Shaw, W. J., Stanton, T. P., McPhee, M. G., Morison, J. H. & Martinson, D. G. 2009 Role of the upper ocean in the energy budget of arctic sea ice during SHEBA. *J. Geophys. Res.* **114**, C06012.

Shen, Y, Tong, P. & Xia, K-Q 1996 Turbulent convection over rough surfaces. *Phys. Rev. Lett.* **76** (6), 908.

Shimada, K., Kamoshida, T., Itoh, M., Nishino, S., Carmack, E., McLaughlin, F., Zimmermann, S. & Proshutinsky, A. 2006 Pacific Ocean inflow: Influence on catastrophic reduction of sea ice cover in the Arctic Ocean. *Geophys. Res. Lett.* **33**, L08065.

Shishkina, O. & Wagner, C. 2011 Modelling the influence of wall roughness on heat transfer in thermal convection. *J. Fluid Mech.* **686**, 568–582.

Simmonds, I. & Rudeva, I. 2012 The great Arctic cyclone of August 2012. *Geophys. Res. Lett.* **39**, L23709.

Skyllingstad, E. D. & Denbo, D. W. 2001 Turbulence beneath sea ice and leads: A coupled sea ice/large-eddy simulation study. *J. Geophys. Res.* **106** (C2), 2477–2497.

Skyllingstad, E. D., Paulson, C. A., Pegau, W. S., McPhee, M. G. & Stanton, T. 2003 Effects of keels on ice bottom turbulence exchange. *J. Geophys. Res.* **108** (C12).

Skyllingstad, E. D., Smyth, W. D., Moum, J. N. & Wijesekera, H. 1999 Upper-ocean turbulence during a westerly wind burst: A comparison of large-eddy simulation results and microstructure measurements. *J. Phys. Oceanogr.* **29**, 5–28.

Smagorinsky, J. 1963 General circulation experiments with the primitive equations. I. The basic experiment. *Mon. Weather Rev.* **91** (3), 99–164.

Stanton, T. P., Shaw, W. J., Truffer, M., Corr, H. F. J., Peters, L. E., Riverman, K. L., Bindschadler, R., Holland, D. M. & Anandakrishnan, S. 2013 Channelized ice melting in the ocean boundary layer beneath Pine Island Glacier, Antarctica. *Science* **341**, 1236–1239.

Steele, M., Morison, J., Ermold, W., Rigor, I., Ortmeyer, M. & Shimada, K. 2004 Circulation of summer Pacific halocline water in the Arctic Ocean. *J. Geophys. Res.* **109**, C02027.

Steele, M., Zhang, J. & Ermold, W. 2010 Mechanisms of summertime upper Arctic Ocean warming and the effect on sea ice melt. *J. Geophys. Res.* **115**, C11004.

Steig, E. J., Ding, Q., Battisti, D. S. & Jenkins, A. 2012 Tropical forcing of Circumpolar Deep Water inflow and outlet glacier thinning in the Amundsen Sea Embayment, West Antarctica. *Ann. Glaciol.* **53** (60), 19–28.

Stern, A. A., Holland, D. M., Holland, P. R., Jenkins, A. & Sommeria, J. 2014 The effect of geometry on ice shelf ocean cavity ventilation: a laboratory experiment. *Exp. Fluids* **55** (5), 1–19.

Stroeve, J., Holland, M. M., Meier, W., Scambos, T. & Serreze, M. 2007 Arctic sea ice decline: Faster than forecast. *Geophys. Res. Lett.* **34** (9).

Thielicke, W. & Stamhuis, E. J. 2014 PIVlab–towards user-friendly, affordable and accurate digital particle image velocimetry in matlab. *J. Open Res. Software* **2** (1), e30.

Timmermans, M-L., Proshutinsky, A., Golubeva, E., Jackson, J. M., Krishfield, R., McCall, M., Platov, G., Toole, J., Williams, W., Kikuchi, T. & Nishino, S. 2014 Mechanisms of Pacific Summer Water variability in the Arctic's Central Canada Basin. *J. Geophys. Res. Oceans* **119** (11), 7523–7548.

Tivy, A., Howell, S. E. L., Alt, B., McCourt, S., Chagnon, R., Crocker, G., Carrieres, T. & Yackel, J. J. 2011 Trends and variability in summer sea ice cover in the Canadian arctic based on the Canadian Ice

Service Digital Archive, 1960–2008 and 1968–2008. *J. Geophys. Res. Oceans* **116** (C3).

Toole, J. M., Timmermans, M-L., Perovich, D., Krishfield, R. A., Proshutinsky, A. & Richter-Menge, J. A. 2010 Influences of the ocean surface mixed layer and thermohaline stratification on Arctic Sea ice in the central Canada Basin. *J. Geophys. Res.* **115**, C10018.

Townsend, A. A. 1964 Natural convection in water over an ice surface. *Quart. J. Roy. Meteor. Soc.* **90** (385), 248–259.

Tyler, S. W., Holland, D. M., Zagorodnov, V., Stern, A. A., Sladek, C., Kobs, S., White, S., Suárez, F. & Bryenton, J. 2013 Using distributed temperature sensors to monitor an Antarctic ice shelf and sub-ice-shelf cavity. *Journal of Glaciology* **59** (215), 583–591.

UNESCO 1981 Tenth report of the Joint Panel on Oceanographic Tables and Standards. Unesco Tech. Pap. in Mar. Sci. 36.

Vancoppenolle, M., Bouillon, S., Fichefet, T., Goosse, H., Lecomte, O., Morales Maqueda, M. A. & Madec, G. 2012 *LIM: The Louvain-la-Neuve sea ice model*. Notes du Pole de modélisation, Institut Pierre-Simon Laplace (IPSL), Paris,France.

Vihma, T. 2014 Effects of Arctic sea ice decline on weather and climate: A review. *Surv. Geophys.* **35**, 1175–1214.

Wadhams, P. 1988 The underside of arctic sea ice imaged by sidescan sonar. *Nature* **333** (6169), 161.

Wadhams, P., Wilkinson, J. P. & McPhail, S. D. 2006 A new view of the underside of arctic sea ice. *Geophys. Res, Lett,* **33** (L04501).

Wagner, W. & Pruss, A. 2002 The IAPWS formulation 1995 for the thermodynamic properties of ordinary water substance for general and scientific use. *J. Phys. Chem. Ref. Data* **31** (2), 387–535.

Wells, A. J. & Worster, M. G. 2011 Melting and dissolving of a vertical solid surface with laminar compositional convection. *J. Fluid Mech.* **687**, 118–140.

Wettlaufer, J. S., Worster, M. G. & Huppert, H. E. 1997 Natural convection during solidification of an alloy from above with application to the evolution of sea ice. *J. Fluid Mech.* **344**, 291–316.

White, F. M. 1974 *Viscous Fluid Flow*. McGraw-Hill.

Woodgate, R. A., Aagaard, K. & Weingartner, T. J. 2006 Interannual changes in the Bering Strait fluxes of volume, heat and freshwater between 1991 and 2004. *Geophys. Res. Lett.* **33**, L15609.

Woodgate, R. A., Weingartner, T. & Lindsay, R. 2010 The 2007 Bering Strait oceanic heat flux and anomalous Arctic sea-ice retreat. *Geophys. Res. Lett.* **37**, L01602.

Yaglom, A. M. & Kader, B. A. 1974 Heat and mass transfer between a rough wall and turbulent fluid flow at high Reynolds and Peclet numbers. *J. Fluid Mech.* **62**, 601–623.

Yang, D., Chamecki, M. & Meneveau, C. 2014 Inhibition of oil plume dilution in Langmuir ocean circulation. *Geophys. Res. Lett.* **41**, 1632–1638.

Yang, D., Chen, B., Chamecki, M. & Meneveau, C. 2015 Oil plumes and dispersion in langmuir, upper-ocean turbulence: Large-eddy simulations and K-profile parameterization. *J. Geophys. Res. Oceans* **120** (7), 4729–4759.

Yang, S. & Christensen, J. H. 2012 Arctic sea ice reduction and European cold winters in CMIP5 climate change experiments. *Geophys. Res. Lett.* **39** (L20707).

Zhang, J., Lindsay, R., Schweiger, A. & Steele, M. 2013 The impact of an intense summer cyclone on 2012 arctic sea ice retreat. *Geophys. Res. Lett.* **40** (4), 720–726.

Zhang, Y-Z., Sun, C., Bao, Y. & Zhou, Q. 2018 How surface roughness reduces heat transport for small roughness heights in turbulent Rayleigh–Bénard convection. *J. Fluid Mech.* **836**.

Vita

Eshwan Ramudu was born in Mauritius on March 6, 1987. He graduated from Harvard University in 2010 with a Bachelor's of Science degree in Engineering Sciences. At Harvard, Eshwan was a Teaching Fellow for an advanced Calculus course, *Applied Math 21a*, and conducted undergraduate research in the School of Engineering and Applied Sciences. He was as an engineer at an ocean wave energy start-up in Boston, MA from 2010 to 2012. Eshwan has been pursuing a Ph.D. in the Department of Earth and Planetary Sciences at Johns Hopkins University since 2012. In 2014, he was awarded an M.S.E. degree in Mechanical Engineering from Johns Hopkins through the Center for Environmental & Applied Fluid Mechanics Dual Degree Program. During his Ph.D., Eshwan has been a Teaching Assistant for several courses offered by the Department of Earth and Planetary Sciences, namely *Introduction to Sustainability*, *Introduction to Global Environmental Change*, *Ocean and Atmospheres*, and *Guided Tour: The Planets*.